Research supported by the National Science Foundation under grants ATM-0071371, ATM - 9618684 and NASA Grant NCC5-288.

THE KINEMATICS AND THERMODYNAMICS OF A MIDLATITUDE, CONTINENTAL MESOSCALE CONVECTIVE SYSTEM AND ITS MESOSCALE VORTEX

by

Jason C. Knievel

Richard H. Johnson, P.I.

Colorado State University

DEPARTMENT OF ATMOSPHERIC SCIENCE

PAPER NO. 730

The Kinematics and Thermodynamics of a Midlatitude, Continental Mesoscale Convective System and Its Mesoscale Vortex

Jason C. Knievel

Department of Atmospheric Science
Colorado State University
Fort Collins, CO 80523-1371

2002

Atmospheric Science Paper No. 730

ABSTRACT

The Kinematics and Thermodynamics of a Midlatitude, Continental Mesoscale Convective System and Its Mesoscale Vortex

The author examines a mesoscale convective system (MCS) and the mesoscale convective vortex (MCV) it generated. The MCS, which comprised a leading convective line and trailing stratiform region, traversed Kansas and Oklahoma on 1 August 1996, passing through the NOAA Wind Profiler Network, as well as four sites from which soundings were being taken every three hours during a field project. The unusually rich data set permitted study of the MCS and MCV over nine hours on scales between those of operational rawinsondes and Doppler radars.

The author used a spatial bandpass filter to divide observed wind into synoptic and mesoscale components. The environment-relative, mesoscale wind contained an up- and downdraft and divergent outflows in the lower and upper troposphere. The mesoscale wind was asymmetric about the MCS, consistent with studies of gravity waves generated by heating typical of that in many MCSs.

According to a scale-discriminating vorticity budget, both the synoptic and mesoscale winds contributed to the prominent resolved sources of vorticity in the MCV: tilting and convergence. Unresolved sources were also large. The author speculates that an abrupt change in the main source of vorticity in an MCV may appear as an abrupt change in its altitude of maximum vorticity.

Distributions of temperature and humidity in the MCS were consistent with its mesoscale circulations. In the terminus of the mesoscale downdraft, advection of drier, potentially warmer air exceeded humidifying and cooling from rain, so profiles of temperature and dewpoint exhibit onion and double-onion patterns. The mesoscale updraft was approximately saturated with a moist adiabatic lapse rate. Mesoscale drafts and convective drafts vertically mixed the troposphere, partially homogenizing equivalent potential temperature.

The MCV contained a column of high potential vorticity in the middle troposphere, with a cold core below the freezing level and a warm core above—a pattern characteristic of profiles of heating by stratiform regions. The cold core was 2 km too shallow to be in pure gradient balance with wind in the MCV. Ongoing forcing during the observed lifetime of the MCV may have prevented it from achieving balance, even if that was its tendency.

Jason C. Knievel
Department of Atmospheric Science
Colorado State University
Fort Collins, Colorado 80523-1371

ACKNOWLEDGEMENTS

The National Science Foundation and the National Aeronautics and Space Administration supported this research with grants ATM 9618684, ATM 0071371, and NCC5-288 SUPP 0002.

Profiler data and code to read them are from S. B. Trier and C.-F. Shih of the National Center for Atmospheric Research (NCAR); satellite images are from the Cooperative Institute for Research in the Atmosphere, thanks to K. Dean and N. McClurg; the skew-T/ln-p program is from G. Thompson of NCAR; code for calculating divergence and vorticity with line integrals is from P. C. Ciesielski of Colorado State University (CSU); WSI's NOWrad radar data are from the Global Hydrology Resource Center; Oklahoma Mesonet data are from the Oklahoma Climatological Survey; GCIP data are from the Joint Office for Scientific Support of the University Corporation for Atmospheric Research and the National Oceanic and Atmospheric Administration (NOAA); level II radar data are from NCAR; code for calculating azimuthal averages around the MCV is from J. P. Kossin of the Space Science and Engineering Center; and code for retrieving thermodynamic fields within balanced vortices is from D. S. Nolan of the University of Miami.

Discussions with the following people improved my research and writing: J. P. Kossin; D. S. Nolan; S. B. Trier; C. A. Davis of NCAR; C. A. Doswell, III of the National Severe Storms Laboratory; P. T. Haertel of NOAA's Aeronomy Laboratory; S. A. Hausman of the United States Air Force; W. A. Petersen of the Earth Systems Science Center; C. R. Pettet of NCAR; H. Richter of Australia's Bureau of Meteorology Research Center; and W. R. Cotton, M. T. Montgomery, and J. A. Ramirez of CSU.

Finally, most invaluable to me were M. D. Parker of the University of Nebraska; and P. E. Ciesielski, R. K. Taft, and my graduate advisor, R. H. Johnson, of CSU.

DEDICATION

To the Davies, Grubenhoff, Lewis, and McCarty families,

and especially to Jennifer

CONTENTS

FIGURES

TABLES

Chapter 1

INTRODUCTION

Mesoscale convective systems (MCSs) with extensive trailing stratiform regions modify their local environments with strong, persistent mesoscale circulations rooted in deep layers of diabatic heating and cooling. In this dissertation I present an examination of the kinematics and thermodynamics of an MCS that traversed Kansas and Oklahoma on 1 August 1996, devoting special attention to the mesoscale convective vortex (MCV) the MCS generated. Because the MCS comprised a leading convective line and a trailing stratiform region, my results and commentary apply to that mode of system, although there are others (Houze et al. 1990; Parker and Johnson 2000).

1.1 Background

Compared to a single cumulonimbus, MCSs are immense. Their lines of intense cumulonimbi are one hundred to many hundreds of kilometers long, and their cloud shields cover tens to hundreds of thousands of square kilometers. MCSs are also long-lived. Although the individual cumulonimbi within an MCS can each exist for less than one hour, the lifetime of an entire system is of order ten hours. Some MCSs even last for days.

Because of their size and longevity, MCSs heavily modify the troposphere around themselves. Modifications include gravity waves, buoyancy rolls, mesoscale updrafts and downdrafts, convergent inflows and divergent outflows, and, in some systems, MCVs. These circulations often extend well beyond the clouds and precipitation of a system (Menard and Fritsch 1989; Mapes 1993; Pandya and Durran 1996), so what appears to be *the environment* in radar and satellite images, may, dynamically and thermodynamically, still be *the MCS*.

Convectively-generated gravity waves and buoyancy rolls are the agents that transmit MCSs' circulations farthest (Nicholls et al. 1991; Mapes 1993). How far they are transmitted depends on the Rossby radius of deformation:

$$\lambda_R = \frac{NH}{(\zeta + f)^{1/2} (2VR^{-1} + f)^{1/2}}, \tag{1.1}$$

wherein N is the Brunt-Väisällä frequency, H is the scale height of the disturbance, ζ is the vertical component of relative vorticity, f is the Coriolis parameter, and V is the wind's rotational component, of which R is the radius of curvature (Shapiro and Willoughby 1982; Frank 1983). In an environment of 100% relative humidity, rising air is heated by condensation as well as cooled by expansion, so N should be replaced by N_m, as explained by Durran and Klemp (1982).

How the atmosphere responds to heating by phase changes in water within a stratiform region depends partly on the horizontal size of the heated area compared with λ_R. When sources of diabatic heating are larger than λ_R, more energy is retained in balanced, vortical flow near an MCS than is transmitted to the far field by gravity waves and buoyancy rolls (Schubert et al. 1980; Mapes 1993). An MCS can shrink its local Rossby radius by saturating the stratiform region, which means a potentially lower-valued N_m replaces N, and by generating a vortical circulation, which increases $2VR^{-1}$ (Schubert and Hack 1982; Chen and Frank 1993). Therefore an MCS first triggers mostly propagative responses in the atmosphere, then as the system grows and matures it converts increasingly more energy into advective responses.

Gravity waves and buoyancy rolls are among the atmosphere's initial propagative responses to concentrated heating and cooling. Advective responses include mesoscale updrafts and downdrafts and part of convergent inflows and divergent outflows; buoyancy rolls contribute to inflows and outflows as well.

The advective part of a mesoscale updraft originates in a convective line. Ascent in a mesoscale updraft comes primarily from heating by deposition in dissipating, buoyant convective cores that move rearward from a convective line (Biggerstaff and Houze 1991). Rearward motion in a mesoscale updraft comes partly from high pressure in the warm updrafts of a convective line, and partly from a line's vertical flux of rearward momentum (Gallus and Johnson 1992).

The advective part of a mesoscale downdraft originates in a stratiform region. A minimum in pressure forms in the middle troposphere at the front of a stratiform region when pressure hydrostatically decreases below the tops of tilted convective updrafts (LeMone 1983). A second minimum in pressure often forms behind the first when diabatic heating in slanted updrafts surmounts diabatic cooling from precipitation (Brown 1979; Johnson and Gallus 1988). Both lows accelerate air from rear to front in a stratiform region.

Divergent outflow in the lower troposphere occurs when an evaporatively- and sublimatively-cooled mesoscale downdraft decelerates upon reaching the ground or a stable layer above the ground. Divergent outflow in the upper troposphere is due to a cold region of high pressure (Maddox et al. 1981; Cotton et al. 1989).

MCVs are less common circulations. They are generally centered in the lower or middle troposphere with tangential wind speeds of orders 1 and 10 m s^{-1}, diameters of order 100 km, and lifetimes of orders 1 and 10 h. In the context of potential vorticity, one source for MCVs is the atmosphere's balanced response to diabatic heating within a stratiform region (Hertenstein and Schubert 1991). Diabatic heating energizes gravity waves that convey some energy to the far field and retain some energy in a local vortical circulation. The partitioning of energy to the far and near fields is based on the size of the system compared with the Rossby radius given by (1.1).

MCVs organize some MCSs on the mesoscale (Menard and Fritsch 1989; Brandes 1990; Raymond and Jiang 1990) and can serve as the primary dynamical link between serial MCSs (Raymond and Jiang 1990; Fritsch et al. 1994; Trier et al. 2000b). There is even growing evidence that MCVs over warm ocean water can be precursors of tropical cyclones (e.g., Bosart and Sanders 1981; Miller and Fritsch 1991; Harr et al. 1996).

Exactly why MCVs are less common than other mesoscale circulations in MCSs is not well understood, but vertical shear is a known factor. Climatologies by Bartels and Maddox (1991) and Trier et al. (2000b) and numerical simulations by Davis and Weisman (1994) and others demonstrated that MCVs are more likely to form in weak to moderate, rather than strong, vertical shear. Once an MCS generates its own circulations, vertical shear in its stratiform region is much differ-

ent from that in the environment. Local vorticity may also be much different from vorticity in the environment because MCSs often form in negative synoptic relative vorticity (Cotton et al. 1989).

If friction is ignored, vertical vorticity within an MCV must originate from some combination of a) horizontal advection of absolute vorticity, b) vertical advection of relative vorticity, c) convergence of absolute vorticity, d) tilting of horizontal vorticity by horizontally-varying vertical wind, and e) horizontal baroclinity. This is apparent upon examination of the equation for the local change in relative vertical vorticity of an inviscid fluid on an f plane:

$$\begin{aligned}\frac{\partial \zeta}{\partial t} = & \underbrace{-\left(\boldsymbol{v} \cdot \boldsymbol{\nabla}\left(\zeta + f\right)\right)}_{a} \underbrace{-\left(w\frac{\partial \zeta}{\partial z}\right)}_{b} \\ & \underbrace{-\left(\left(\zeta + f\right)\boldsymbol{\nabla} \cdot \boldsymbol{v}\right)}_{c} \underbrace{+\left(\xi\frac{\partial w}{\partial x} + \eta\frac{\partial w}{\partial y}\right)}_{d} \\ & \underbrace{+\left(\mathbf{J_{xy}}\left(p, \alpha\right)\right)}_{e},\end{aligned} \tag{1.2}$$

wherein $\boldsymbol{\zeta}(\xi, \eta, \zeta)$ is relative vorticity, $\boldsymbol{v}(u, v)$ is horizontal wind, w is vertical wind, f is the Coriolis parameter, and $\mathbf{J_{xy}}\left(p, \alpha\right)$ is the two-dimensional Jacobian of pressure, p, and specific volume, α. Letters assigned to the terms correspond to the enumeration earlier in the paragraph. Baroclinity is weak near MCVs and may be ignored (Skamarock et al. 1994). In a Lagrangian sense, advections only redistribute vorticity, they do not create it, so analyses of vertical vorticity in MCVs tend to emphasize horizontal divergence and tilting, terms (c) and (d) in (1.2). Contributions from both sources are frequently large (e.g., Brandes 1990; Chong and Bousquet 1999). (Henceforth, *vorticity* means *relative vertical vorticity*, and *divergence*, *convergence*, and *shear* mean *horizontal divergence*, *horizontal convergence*, and *vertical shear* unless otherwise stated.)

Convergence in the middle troposphere within the stratiform region of an MCS can concentrate existing planetary and synoptic vorticity (Bartels and Maddox 1991; Johnson and Bartels 1992; Skamarock et al. 1994). Some of this convergence is in response to diabatic heating and cooling in the stratiform region of an MCS (Hertenstein and Schubert 1991), and is equated with vertical divergence from a mesoscale updraft above a mesoscale downdraft.

Tilted circulations are sources and sinks of vorticity as well. Horizontally varying vertical motion in an MCS's mesoscale updraft or downdraft can tilt vorticity equated with sheared wind (Davis and Weisman 1994). Both wind in an MCS and wind in the system's environment are sheared, but initial studies of tilted vorticity in MCVs emphasized only environmental shear (e.g., Biggerstaff and Houze 1991) or did not differentiate between the two shears (e.g., Brandes 1990). Not until more recently have a few studies demonstrated that vertical shear in MCSs is an important source of vorticity within MCVs (e.g., Davis and Weisman 1994; Chong and Bousquet 1999; Bousquet and Chong 2000).

1.2 Objectives and motivations

To varying extents, all empirical studies of MCVs and the MCSs that generate them are handicapped by limited data. Outside of elaborate and infrequent field projects the handicap can be severe. Because MCSs and MCVs are long-lived and mobile, normally an empiricist must compromise between coarse data that encompass a large fraction of the lifetimes of a system and vortex (e.g., Bosart and Sanders 1981; Fritsch et al. 1994; Bartels et al. 1997) or fine data that encompass only a small fraction of their lifetimes (e.g., Keenan and Rutledge 1993; Scott and Rutledge 1995; Chong and Bousquet 1999). Thermodynamical data are especially scant.

In a departure from this norm, the MCS and MCV of 1 August 1996 presented an opportunity for detailed mesoscale analysis over nine hours when they traversed Kansas and Oklahoma. The system and vortex were observed in unusual detail by the densest part of the National Oceanic and Atmospheric Administration (NOAA) Wind Profiler Network (NPN), by four sites above which thermodynamical soundings were taken every three hours as part of an ongoing field project in the southern Great Plains, and by the Oklahoma Mesonet. (Although a union of observations from these platforms is unprecedented in the study of an MCV, the data still fall short of fully describing the life cycles of the MCS and MCV of 1 August 1996.)

In applying to these data a few new variations on proven analysis techniques, my objective was to address four questions rarely, or not at all, addressed in published empirical research:

- What form do the primary mesoscale circulations within an MCS take when viewed in an environment-relative frame of reference?

MCSs are commonly depicted in a storm-relative frame of reference, whereby the translational motion of an MCS is subtracted from the observed wind. This reveals many phenomena, such as hydrometeor transports and thermal advections, but it can mask some mesoscale structure within MCSs. I adopted an environment-relative frame of reference, whereby the synoptic component was removed from the observed wind. Few MCSs, and no MCVs, have been examined from this perspective. Results in the environment-relative frame of reference are especially valuable for comparison with perturbation flows in numerically simulated MCSs and MCVs.

- What are the sources of vorticity in MCVs on the scale of the MCS and on the scale of the larger environment?

Most empirical vorticity budgets for MCVs fall into two categories. In the first category are studies of vorticity on the scale of an MCS and MCV; these are usually based on Doppler radars and/or research sounding networks (e.g., Biggerstaff and Houze 1991; Johnson and Bartels 1992; Chong and Bousquet 1999). In the second category are larger-scale budgets based on the nation's operational sounding network (e.g., Bartels and Maddox 1991). No single empirical vorticity budget for an MCV has included an investigation of circulations within an MCS and those within the MCS's larger environment. I present the first budget for vorticity in an MCV that comprises terms for sources and sinks of vorticity within an MCS, its environment, and combinations of the two. The budget has the added advantage of encompassing nine hours of the MCV's lifetime.

- To what extent are the wind and mass of observed MCVs in gradient balance?

The fact that some MCVs persist for days suggests that a subset of vortices comprise fields of wind and mass that are nearly balanced, and many researchers have successfully simulated MCVs and similar vortices in numerical models founded on various assumptions of balance (e.g., Hack and Schubert 1986; Raymond and Jiang 1990; Davis and Weisman 1994). Explicitly evaluating balance

within observed MCVs is more difficult, and no one has done it yet, perhaps because soundings through cores of MCVs are extremely rare. Fortuitously, one sounding through the MCS of 1 August 1996 was nearly through the center of the MCV. That sounding and the relatively detailed observations of wind by the NPN permit an explicit assessment of gradient balance.

- How closely does the structure of potential vorticity in observed MCVs resemble that predicted by theory and numerical simulations?

According to theory and numerical simulations, the positive vertical gradient of diabatic heating in the middle troposphere within stratiform regions generates high potential vorticity in the lower troposphere and low potential vorticity in the upper troposphere (e.g., Hoskins et al. 1985; Haynes and McIntyre 1987; Raymond and Jiang 1990). It is difficult to observe this distribution of potential vorticity on the scale of an MCV. Fritsch et al. (1994), in a rare study of its kind, resorted to creating a composite MCV with operational soundings taken over three days. For the MCS of 1 August 1996, data from a field project in the southern Great Plains enabled me to diagnose potential vorticity from a composite MCV created with soundings over only six hours.

Answers to these specific questions are related to fascinating, deeper issues about MCSs and MCVs that are not easily tackled. Among the few that I briefly touch on at the end of the dissertation in chapter 6 are: 1) the most appropriate way to describe and measure an MCV's kinematical environment; 2) the amount of realism one must include in the environment of a simulated MCV in order for the results of the simulation to be realistic; 3) whether the life cycles of MCVs can be divided into regimes, each characterized by a single primary net source of vorticity; and 4) the narrow range of shear that is strong enough to be an important source of tilted horizontal vorticity but is not so strong that it rips apart MCVs.

Chapter 2

DATA AND METHODS

Observations are from the National Weather Service (NWS), remote sensors operated by NOAA, 1996's Enhanced Seasonal Observing Period (ESOP-96) of the Global Energy and Water Cycle Experiment's (GEWEX's) Continental-Scale International Project (GCIP), and the Oklahoma Climatological Survey's Oklahoma Mesonet (Brock et al. 1995; Shafer et al. 2000).

2.1 Satellite

Satellite data are from channels one (visible, 0.55–0.75 μm), three (water vapor, 6.50–7.00 μm), and four (infrared, 10.20–11.20 μm) from Geostationary Operational Environmental Satellites (GOESs) 8 and 9.

2.2 Radar

Radar data are instantaneous composite reflectivity with temporal and spatial intervals of 15 min and 2 km $\times$ 2 km. Each pixel for a specific point at a specific time is the highest reflectivity detected in a column by any radar. A 24-h animation of composite reflectivity provided the best overall, qualitative sense of the MCS's evolution, and was the means by which I first detected the MCV within the MCS's stratiform region. For more detailed analyses of the system and vortex I used the Weather Surveillance Radar-1988 Doppler (WSR-88D) Algorithm Testing and Display Program (WATADS 10.0) to examine level II data from WSR-88Ds at Oklahoma City (KTLX) and Vance Air Force Base, OK (KVNX).

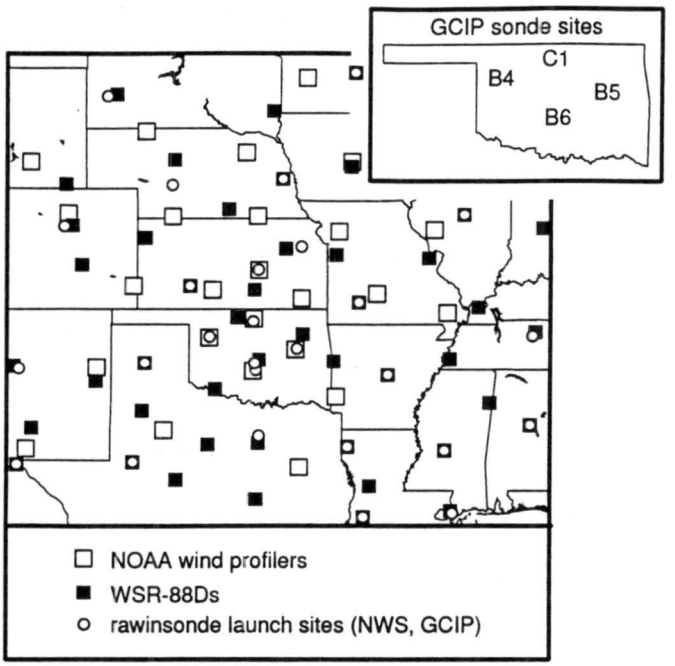

Figure 2.1: Sites of observations above the ground. NOAA wind profilers are marked by large open squares, WSR-88Ds by small solid squares, and radiosonde launch sites of the NWS and GCIP ESOP-96 by small open circles.

2.3 Surface

I inferred synoptic and mesoscale fronts near the ground primarily from my own manual analyses of temperature from observations in METAR, the international format for reporting surface weather, and from the Oklahoma Mesonet. When such analyses were insufficient, I referred to manually analyzed streamlines, radar reflectivity from WSR-88Ds, and satellite data from GOES 8 and GOES 9. Some choices of mesoscale fronts were educated guesses, and I did not pursue detailed explanations of the fronts' origins.

2.4 Soundings

Tropospheric soundings are from the NPN (Weber et al. 1993; Barth et al. 1994), radiosondes launched semi-daily by the NWS, and radiosondes launched every three hours from four sites in Oklahoma during ESOP-96 of GCIP (fig. 2.1).

I analyzed hourly data from the NPN taken from 0.5 to 16.25 km above ground level (AGL), excluding data that failed NOAA's checks for temporal and spatial continuity (Weber et al. 1993) and their check for contamination by migrating birds (Barth, personal communication, 1998). I inspected all soundings for gross errors, removed them, and linearly interpolated in the voids.

From 0900 to 1800 UTC on 1 August, the *period of detailed analysis*, 12% of soundings were missing at the NPN sites closest to the MCS, 13% at the seven most densely spaced sites (fig. 2.1). Only at 1800 UTC was I able to substitute a GCIP sounding for a missing NPN sounding.

For thermodynamical soundings, convective available potential temperature (CAPE) and convective inhibition (CIN) were calculated for a thoroughly mixed boundary layer 10 hPa deep for morning soundings and 100 hPa deep for afternoon soundings.

2.5 Objective analyses and bandpass filtering

To produce gridded fields of *total wind*, $\boldsymbol{u}(u, v, w)$, I used a two-pass Barnes analysis (Barnes 1973; Koch et al. 1983) on data from the NPN. Grid points were 75 km apart, the cut-off radius was 750 km, and the response function was chosen to capture 90% of the signal of phenomena with wavelengths of 300 km, which is twice the average distance between profilers in the densest part of the NPN (*total* curve in fig. 2.2). Less than 10% of the signal of phenomena with wavelengths shorter than 85 km was captured, so virtually no coherent convective signal exists in the analyzed data.

To partially isolate the mesoscale kinematics of the MCS from the synoptic kinematics, I employed a second Barnes analysis, which, together with the first, acted as a spatial bandpass filter (Maddox 1980). The *synoptic background wind*, $\widetilde{\boldsymbol{u}}(\widetilde{u}, \widetilde{v}, \widetilde{w})$, was approximated with data filtered to include 90% and 0.09% of the signals of phenomena with wavelengths of 1600 km and 300 km, respectively (*synoptic* curve in fig. 2.2). This is the same filtration Maddox (1980) used for synoptic features. The *mesoscale perturbation in wind*, $\widehat{\boldsymbol{u}}(\widehat{u}, \widehat{v}, \widehat{w})$, was approximated by subtracting the synoptic background wind from the total wind (*mesoscale* curve in fig. 2.2). In summary: $\boldsymbol{u}(u, v, w) = \widetilde{\boldsymbol{u}}(\widetilde{u}, \widetilde{v}, \widetilde{w}) + \widehat{\boldsymbol{u}}(\widehat{u}, \widehat{v}, \widehat{w})$. Sometimes I refer to the components simply as the *syn-*

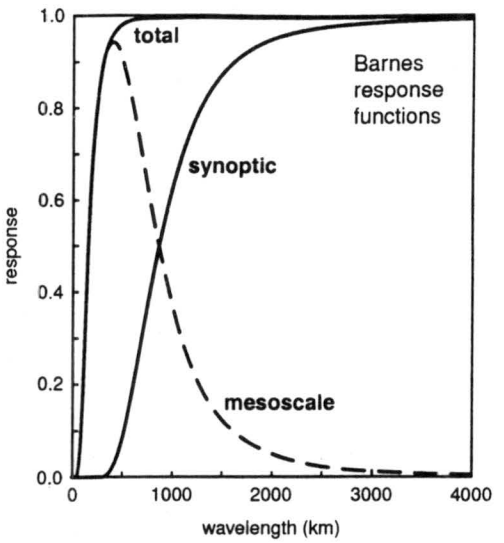

Figure 2.2: Response functions for the Barnes analyses.

optic wind and the *mesoscale wind.* Figure 2.3 shows examples of them and demonstrates that the technique capably resolved the MCV of 1 August as it moved southeastward across Oklahoma.

The right column of panels in figure 2.3 may give the impression of discontinuities in the mesoscale wind, discontinuities that would produce unrealistic derivatives. That impression seems to be an artifact of the eyes' interpretation of vectors, though, because vorticity (fig. 2.4) and divergence (not shown) of the mesoscale wind are acceptably smooth.

The bandpass filter did not completely isolate the mesoscale and synoptic winds from each other, especially at scales near where the two response curves cross (fig. 2.2). If one considers mesoscale phenomena to have characteristic lengths of 2–2000 km (Orlanski 1975), then what I call the *synoptic background wind* certainly contains some mesoscale signal. However, the wavelengths of the MCS and MCV of 1 August 1996 were near the peak of the mesoscale response function, ~400 km, where the synoptic part of the filter was quite insensitive.

2.6 Divergence and vorticity

I calculated divergence and vorticity two ways. Results in this dissertation are from centered finite differences of objectively analyzed fields of u and v components of wind. This method can

produce derivatives corrupted by noise (Schaefer and Doswell III 1979), so I tested it against line integrals of tangential and normal components of wind calculated around the perimeter of triangles whose vertices were the profilers (Ceselski and Sapp 1975). The two methods produced comfortingly similar results.

2.7 Vertical velocity

Vertical velocity is from the kinematical method with a linear correction to density-weighted divergence (O'Brien 1970), for which I set $w = 0$ at 750 m above the tropopause and $w = 0$ at 500 m AGL. The upper condition is based on work by Johnson et al. (1990), who showed that vertical velocity above the stratiform region of the MCS of 10–11 June 1985 was close to zero one kilometer above the tropopause. The lower condition was a pragmatic choice; surface data at the NPN sites were unavailable, and Brandes (1990) and others showed that magnitudes of mesoscale vertical motions near 500 m AGL in the presence of MCSs are only $0–5\times10^{-2}$ m s^{-1}.

2.8 Vorticity budget

As mentioned in chapter 1, for a budget of wind above the boundary layer and any cold pool it is reasonable to dismiss baroclinity, represented by the Jacobian in (1.2). For the remaining four terms in (1.2), I calculated a budget for both the synoptic background wind and the mesoscale perturbation in wind. The local derivative on the left side of (1.2) is for a $2°\times2°$ area repositioned every hour so it was centered on the middle-tropospheric part of the MCV. Mesoscale wind in the middle troposphere was virtually the same as a *system-relative* wind (i.e., wind in a frame of reference that moved with the MCV) because the translational motion of the MCV was due primarily to advection by the background synoptic wind in the middle troposphere. This is often the case (e.g., Zhang and Fritsch 1988; Johnson and Bartels 1992; Trier et al. 2000b). Over the detectable lifetime of the MCV, zonal and meridional components of the synoptic background wind at the three-dimensional center of the MCV were 7.7 and -8.1 m s^{-1}, respectively. The corresponding components of the MCV's average translational velocity were 7.4 and -8.1 m s^{-1}. Therefore, once

the synoptic wind was removed from the total wind, the frame of reference moved in the middle troposphere with the MCV, and the circulation of the mesoscale perturbation in wind within the MCV was approximately closed (fig. 2.3b).

I calculated on a grid the vorticity budget for the mesoscale perturbation in wind, for the synoptic background wind, and for the sum of the two, the total wind. This sum is not truly a total wind in that it does not contain fully-sampled contributions from sub-grid phenomena such as eddies from cumulonimbi. First, the NPN is insufficiently dense to record unaliased observations of such phenomena. Second, filtering by the Barnes routine excluded nearly all sources and sinks of vorticity with wavelengths smaller than 85 km. Yet phenomena this small undoubtedly contributed to temporal changes in vorticity (Weisman and Davis 1998), and those contributions probably translated to larger scales to which the Barnes routine was sensitive (Esbensen 1993). Fortunately, eddy fluxes of momentum in MCSs are generally less in stratiform regions than in convective lines (Gallus and Johnson 1992), and my vorticity budget is limited to the former.

Because of such unresolved sources and sinks of vorticity, the budget has a residual, which necessarily also includes observational errors. When written in terms of a resolved synoptic component, designated by $\widetilde{(\ )}$; a resolved mesoscale component, designated by $\widehat{(\ )}$; and a residual, Z; (1.2) becomes

$$\begin{aligned}
\frac{\partial \zeta}{\partial t} = \frac{\partial(\widetilde{\zeta} + \widehat{\zeta})}{\partial t} = \\
&- (\widetilde{\mathbf{v}} + \widehat{\mathbf{v}}) \cdot \boldsymbol{\nabla}(\widetilde{\zeta} + f + \widehat{\zeta}) \\
&- (\widetilde{w} + \widehat{w}) \frac{\partial(\widetilde{\zeta} + \widehat{\zeta})}{\partial z} \\
&- (\widetilde{\zeta} + f + \widehat{\zeta}) \boldsymbol{\nabla} \cdot (\widetilde{\mathbf{v}} + \widehat{\mathbf{v}}) \\
&+ (\widetilde{\xi} + \widehat{\xi}) \frac{\partial(\widetilde{w} + \widehat{w})}{\partial x} + (\widetilde{\eta} + \widehat{\eta}) \frac{\partial(\widetilde{w} + \widehat{w})}{\partial y} \\
&+ \mathbf{J}_{\mathbf{xy}}(\widetilde{p} + \widehat{p}, \widetilde{\alpha} + \widehat{\alpha}) \\
&+ Z.
\end{aligned} \tag{2.1}$$

I vertically smoothed terms in the budget with a five-point, center-weighted running mean. The appendix provides examples of the formulae I used to apply (2.1) to data on a grid.

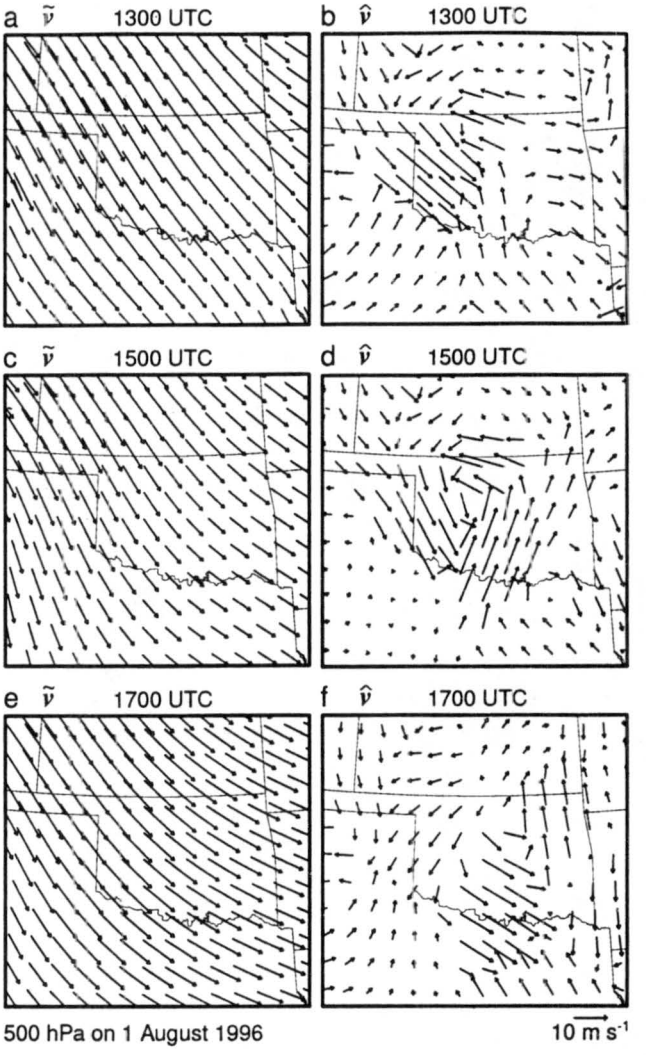

Figure 2.3: Synoptic and mesoscale winds at 500 hPa on 1 August 1996. The rows from top to bottom are for 1300, 1500, and 1700 UTC; the columns from left to right are the synoptic background wind and the mesoscale perturbation in wind.

Often the resolved terms on the right side of a budget in the form of (2.1) together nearly cancel the residual, leaving the local tendency as a small difference in this near cancellation (e.g., Reed and Johnson 1974). Therefore, the magnitude and even the sign of the local tendency, $\partial\zeta/\partial t$, is very sensitive to errors in the horizontal derivatives that compose the resolved terms. This sensitivity is especially troublesome if one uses the local tendency to predict vorticity. I did not do this because

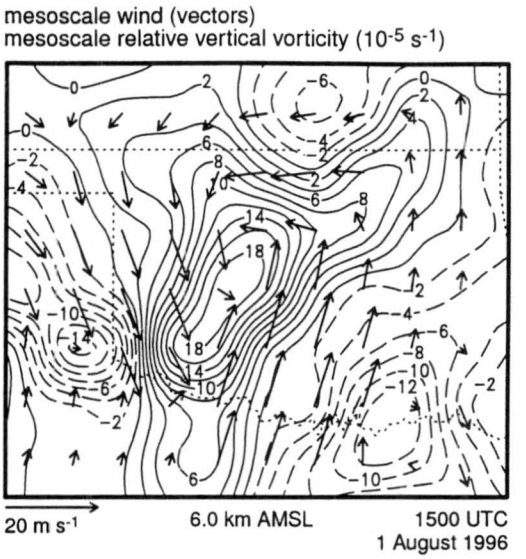

Figure 2.4: Mesoscale wind (m s^{-1}) and vorticity (10^{-5}s^{-1}) at 6.0 km AMSL at 1500 UTC on 1 August 1996.

observations of vorticity were available every hour for my analysis. Even so, it is valuable to assess how the local tendency differs when calculated with a budget based on a mathematically simpler form of the vorticity equation than that on which I based (2.1).

One such equation, used in vorticity budgets by Davis and Weisman (1994) and Weisman and Davis (1998), among others, may be written most simply as

$$\frac{\partial \zeta}{\partial t} = \nabla \cdot \boldsymbol{K}, \tag{2.2}$$

in which friction and baroclinity are ignored and

$$\boldsymbol{K} = w\left(\boldsymbol{k} \times \frac{\partial \boldsymbol{v}}{\partial z}\right) - \boldsymbol{v}(\zeta + f), \tag{2.3}$$

wherein $\boldsymbol{k}$ is the vertical unit vector, and all the other symbols have meanings as in (2.1). When (2.2) and (2.3) are combined, the explicit terms are

$$\frac{\partial \zeta}{\partial t} = -\frac{\partial}{\partial x}\left[w\frac{\partial v}{\partial z} + u(\zeta + f)\right] - \frac{\partial}{\partial y}\left[w\frac{\partial u}{\partial z} + v(\zeta + f)\right]. \tag{2.4}$$

I checked the results of (2.1), which I call the *conventional form* of the vorticity budget, with (2.2), which is sometimes called the *flux form*, but which I call the *divergence form* of the vorticity budget. Results of the check appear later in the dissertation.

2.9 Rossby radius of deformation

Calculations of the Rossby radius of deformation, λ_R, were hampered by scant thermodynamical data. The only GCIP radiosonde from which data were not lost during penetration of the stratiform region near the core of the MCV was launched at 1800 UTC from Morris, OK (B5). From that sounding (shown later in figure 5.5) I calculated N in (1.1) over a depth of 3 km to be 1.05×10^{-2} s^{-1}, which I used in calculations for other times and locations. The resultant value of 31.5 m s^{-1} for NH is very close to the fixed 30.0 m s^{-1} used by Cotton et al. (1989) in their evaluation of changes in λ_R over the lifetime of a composite mesoscale convective complex (MCC), a specific type of large MCS. Although the calculation of λ_R was for a part of the stratiform region, the lower troposphere was subsaturated there, so I used N instead of the N_m mentioned in section 1.1.

2.10 Schematic cross sections

Although the NPN provided a much more resolved data set than would have been available from operationally launched radiosondes alone, missing data still made impossible detailed analyses at every individual hour, especially late in the lives of the MCS and MCV. I mitigated this problem in two ways. First, I examined vertical velocity, divergence, and vorticity in the form of temporal and spatial averages over 3 h and a $2°\times2°$ area centered on the MCV. Second, I scrutinized vertical and horizontal cross sections of wind only for times at which the most data were available, and present herein to the reader cross sections that are schematic (derived, for example, from analyses of perturbation wind such as shown in fig. 2.3b, d, and f). This allows me to depict features that appear in various data sets, sometimes at various times, in a way I believe best represents the overall kinematics of the MCS and MCV.

2.11 Spatial and temporal extent of the MCV

Determining an MCV's location, lifetime, and size is not straightforward. As yet there is no universally accepted approach, possibly because no single approach tried so far works well with every data set. I diagnosed the center of the MCV to be at the center of the observable cyclonic motion in composite radar reflectivity. For the purposes of this research, I considered the MCV to have formed when a cyclonic circulation first appeared and to have dissipated when that cyclonic circulation disappeared. Proximate radar echoes were present before, during, and after the MCV's lifetime, so it is quite unlikely that the MCV existed long before or after I could detect it with radar, but with other MCVs this is often not the case. Methods of locating the MCV based on kinematical and thermodynamical data proved too sensitive to the coarseness of observations, producing closed streamlines and maxima in vorticity that unrealistically jumped hundreds of kilometers from some times to the next. Methods based on infrared satellite data were impossible due to cirri above the swirl of clouds in the middle troposphere.

Because of the coarseness of the kinematical data, I could do no more than estimate the size of the MCV at certain times when the vortex seemed best observed. The radius of maximum wind was approximately 0.75–1.50° latitude (83–167 km). The rotating cloud shield extended beyond the radius of maximum wind—which is common (e.g. Fritsch et al. 1994)—to a radius of approximately 2.0° latitude (222 km). Some have estimated the perimeter of MCVs with contours of vorticity (e.g., Brandes and Ziegler 1993). The weakness in this method is that horizontal shear near MCSs often contributes large vorticity, which can elongate contours or displace even quasi-circular contours well away from the center of an MCV's rotation.

2.12 Tilt of the MCV

The distance between even the most closely-spaced NPN sites made it impossible to measure reliably to what extent the MCV was tilted away from vertical. If one could safely assume steady-state tilt, hourly profiles of wind from even a single site might be useful, but such an assumption is unreliable because the tilt of some MCVs can change hourly (Trier and Davis 2002).

2.13 Gradient balance in the MCV

In order to assess the extent to which the MCV of 1 August 1996 was in gradient balance, I retrieved a balanced temperature profile from observed wind in the MCV, then compared that retrieved, balanced profile to an observed profile in the MCV's core.

The procedure demanded a number of approximations and compromises. The only complete sounding near the core of the MCV was above Purcell, OK (B6) at 1800 UTC. However, no GCIP sounding site was unaffected by the MCS at that time, so a more realistic far-field boundary condition for the retrieval was an average of soundings above Dodge City, KS (DDC), Little Rock, AR (LIT), and Shreveport, LA (SHV) taken at 0000 UTC, six hours later. As an additional complication, wind observations from the NPN at 1800 UTC were unrepresentative, as I explain in chapter 4, so I chose to retrieve the balanced temperature profile from observations of wind at 1500 UTC.

The retrieval involved three steps. First, I approximated the observed MCV with an axisymmetric, non-divergent vortex constructed from the azimuthal average of observed tangential winds. Second, I used the far-field sounding and wind field at each altitude to calculate the pressure field inward from the perimeter to the core. Third, I forced the temperature field into hydrostatic balance, based on the pressure field. The second and third steps were repeated until the gradient imbalance in the axisymmetric vortex was extremely small.

2.14 Composite MCV and potential vorticity

In order to calculate from the few available thermodynamical soundings a meaningful, three-dimensional distribution of potential vorticity, I constructed a composite MCV from GCIP soundings taken at 1500 through 2100 UTC. Each sounding was positioned relative to the MCV's middle-tropospheric center at the time the respective sondes were launched, then the data were objectively analyzed with a Cressman (1959) scheme. I calculated potential vorticity, P, according to the approximate form in Cartesian coordinates:

$$P \approx \alpha (\zeta + f) \frac{\partial \theta}{\partial z}, \tag{2.5}$$

wherein θ is potential temperature and the other symbols have the same meanings as in (1.2). This approximation to the full equation,

$$P = \alpha (\zeta + f) \cdot \nabla \theta, \tag{2.6}$$

is valid when horizontal gradients of potential temperature are much smaller than the vertical gradient, which was the case on the mesoscale and the synoptic scale near the MCV, above boundaries near the ground. Among the papers that explain potential vorticity and its usefulness are those by Hoskins et al. (1985) and Haynes and McIntyre (1987).

Chapter 3

ENVIRONMENT AND LIFE CYCLES OF THE MCS AND MCV

The MCS formed at 0430 UTC on 1 August 1996 and had completely dissipated by 0315 UTC on 2 August. The MCS's environment was not different in any important way from the environments of other observed MCSs that generated MCVs (e.g., Bartels and Maddox 1991; Trier et al. 2000b).

3.1 Above the ground

The MCS originated in weakly to moderately sheared northwesterly wind upstream of conditionally unstable air. The northwesterlies were a result of a ridge centered over the Colorado Plateau and a trough centered over the Great Lakes (fig. 3.1). Within the northwesterlies was a short-wave trough in the lower and middle troposphere. Vorticity advection at 500 hPa was weak to non-existent (not shown). Four GCIP soundings at 0900 to 1200 UTC ahead of the MCS display a shallow nocturnal inversion surmounted by layers of weak conditional instability from the lower to the upper troposphere (fig. 3.2 is an example). CAPE ranged from 321 to 1483 J kg^{-1}, and CIN from 91 to 305 J kg^{-1}. Because the last sounding ahead of the MCS was at 1200 UTC, these ranges of CAPE and CIN almost certainly do not represent the environment that the mature, decaying, and dissipating MCS encountered later in the day. The sounding at 0000 UTC on 2 August above Shreveport, LA, approximately 200 km southeast of where the MCS dissipated, registered CAPE of 2513 J kg^{-1} and CIN of 6 J kg^{-1}. I believe these values better represent the environment of the MCS during the afternoon of 1 August. The average altitude of the tropopause near the MCS was 15.73 km AMSL (116 hPa) and the average altitude of 0°C was 4.48 km (596 hPa). A weak to

moderate southerly low-level jet (Whiteman et al. 1997) appeared between 100 and 500 m AGL in the vicinity of the MCS after nightfall (not shown). At the jet's altitude, gradients in temperature and moisture were small, so advections were weak.

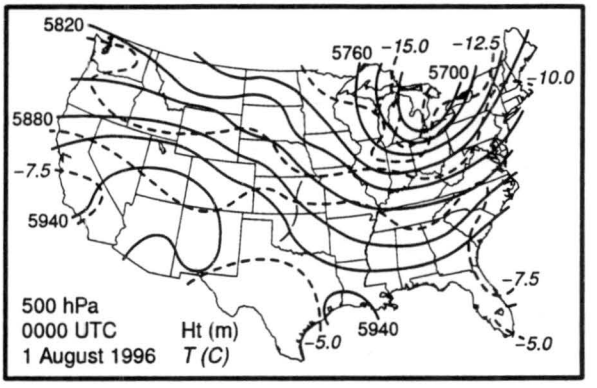

Figure 3.1: Height (m AMSL) and temperature (°C) at 500 hPa at 0000 UTC on 1 August 1996. The thin line with long dashes marks the axis of a short-wave trough.

These tropospheric conditions are similar to those in environments of other MCSs that generated MCVs. Bartels and Maddox (1991) showed that 29% of MCVs in the population they studied formed in northwesterly wind between a ridge and trough at 500 hPa, and weak vorticity advection and low-level jets were common. Bartels and Maddox (1991) and Trier et al. (2000b) noted high CAPE ahead of many of the MCVs in their studies. The latter found that CAPE averaged 1895 J kg^{-1} among MCVs that fostered a secondary MCS. The MCV of 1 August 1996 did foster secondary cumulonimbi, but not in the form of an MCS.

3.2 Near the ground

A synoptic stationary front extended southward through the western High Plains, then southeastward across the Great Plains (fig. 3.3). At 0000 UTC on 1 August, three mesoscale fronts disrupted and modified the synoptic front in Wyoming, Colorado, and Kansas. These fronts appeared to be the leading edges of outflow from unorganized clusters of cumulonimbi, but data were inconclusive. (Fronts were determined from observations more dense than those shown in figure 3.3.)

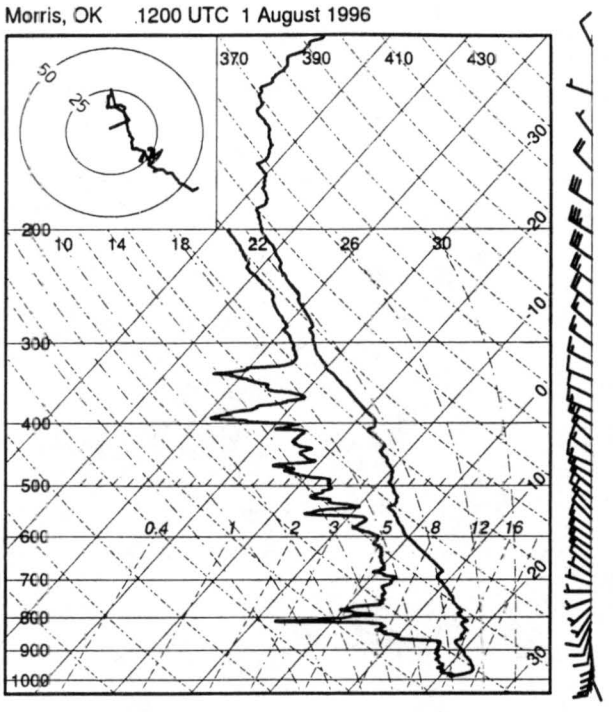

Figure 3.2: Sounding above Morris, OK (B5) at 1200 UTC on 1 August 1996. Half and full wind barbs respectively represent 2.5 and 5.0 m s^{-1}. CAPE was 436 J kg^{-1} and CIN was 198 J kg^{-1}. This sounding is representative of those taken ahead of the MCS early on 1 August.

Trier et al. (2000b) found that over half the MCVs in the central United States during spring and summer 1998 were generated by MCSs that formed near synoptic surface fronts. Most of these MCSs originated on the cold side of east-west, quasi-stationary fronts like the one in figure 3.3. After it formed, the MCS of 1 August 1996 soon moved south of the synoptic front. Although the MCS's outflow effectively kept the system on the cool side of the mesoscale front, deep towers in the convective line were fed by warm environmental air from the south.

3.3 The MCS and MCV

The MCS studied herein was the largest, but not the only, organized system of cumulonimbi in the central United States on 1 August 1996; a smaller vortical system formed in South Dakota and crossed Nebraska (states, but not the smaller system, are shown in figure 3.3). At various

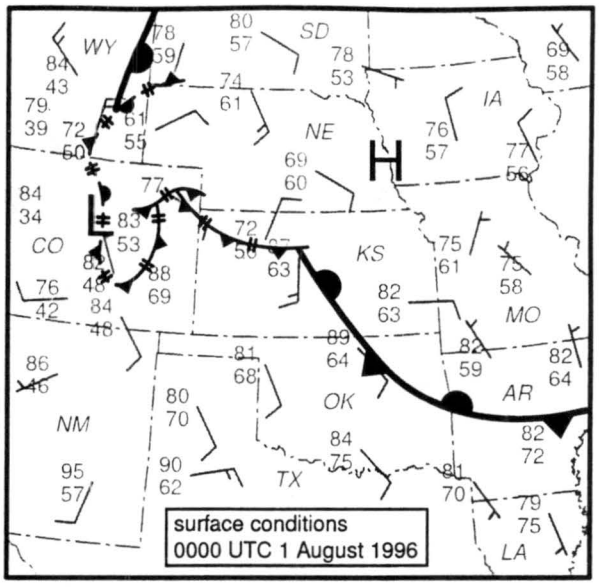

Figure 3.3: Synoptic and mesoscale fronts at 0000 UTC on 1 August 1996. Station models display temperature, dewpoint (both °F), and wind, for which full and half barbs respectively represent 2.5 and 5.0 m s^{-1}. An absent vector indicates a missing observation, not necessarily calm conditions. Regions of locally high and low pressure are respectively marked by Hs and Ls.

stages, the larger MCS (and, henceforth, the only one to which I will refer) exhibited many classic characteristics of MCSs that generate MCVs (table 3.1 and fig. 3.4). Early symmetry gave way to asymmetry as the MCS matured, which exemplifies recent conclusions by Skamarock et al. (1994), Loehrer and Johnson (1995), and others that *symmetric* and *asymmetric* are adjectives that should be applied to *stages* in some MCSs, not to MCSs as a whole.

3.3.1 Formation

The MCS formed with the merger of three clusters of cumulonimbi between 0345 and 0415 UTC on 1 August. The first cluster, *A* in fig. 3.4a, emerged from a large mass of cumulonimbi in the Panhandle of Nebraska. The second cluster, *B*, appeared to form along the short mesoscale front in the northeastern corner of Colorado (fig. 3.3). The third cluster, *C*, formed along the mesoscale front in northwestern Kansas. Between 0430 and 0530 UTC the three clusters became indistinguishable; they were the incipient MCS.

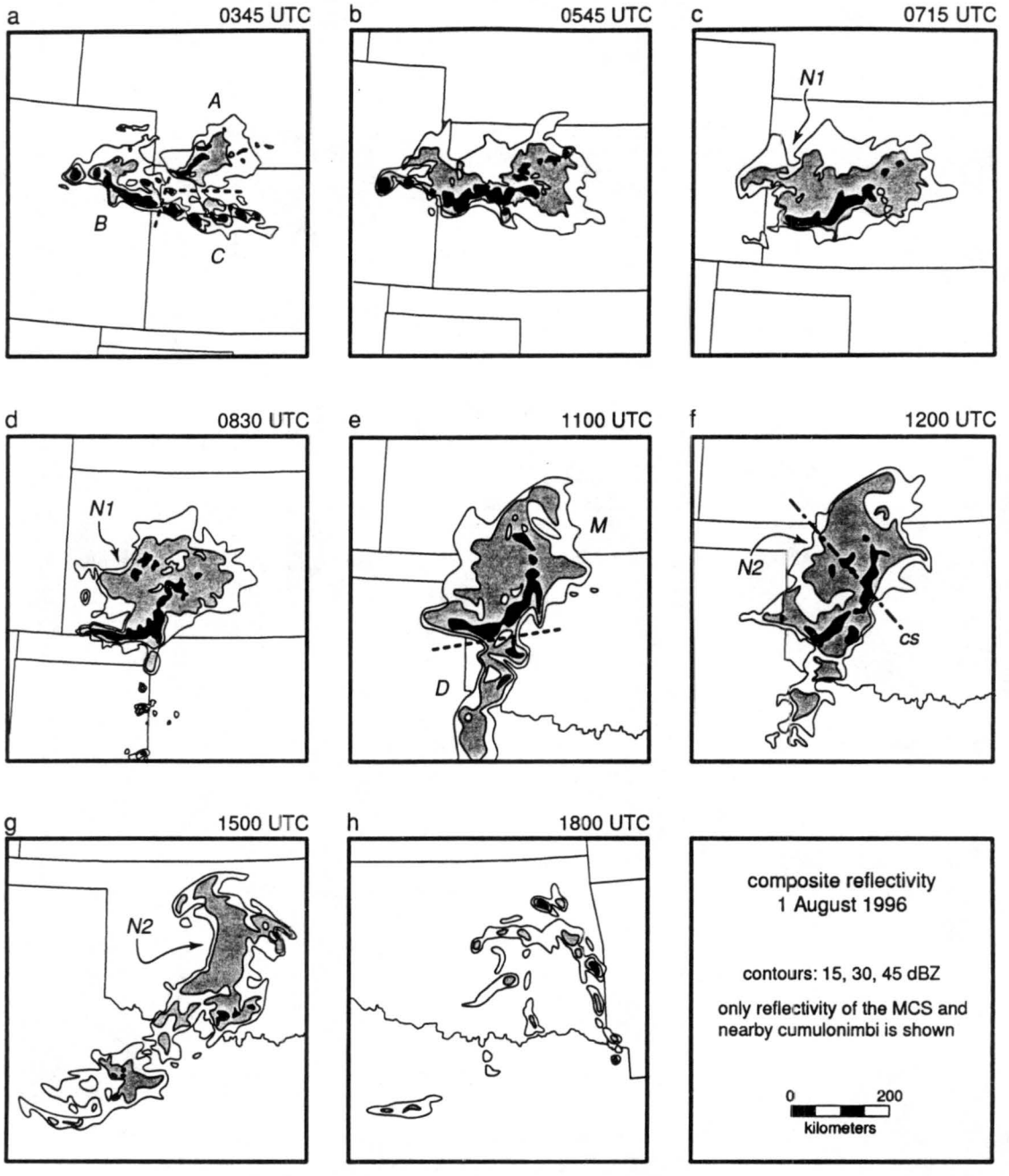

Figure 3.4: Composite reflectivity at eight times on 1 August 1996. Times are a) 0345, b) 0545, c) 0715, d) 0830, e) 1100, f) 1200, g) 1500, and h) 1800 UTC. Contours are at 15, 30, and 45 dBZ. Only reflectivity due to the MCS and nearby cumulonimbi is shown. Three clusters that merged to form the incipient MCS are separated by dashed lines and marked with *A*, *B*, and *C*. A band of cumulonimbi that was overtaken by the MCS, *M*, is marked by *D*. Notches are marked by *N1* and *N2*. The location of the cross section in fig. 4.4 is marked by *cs*.

3.3.2 Development

The MCS spent 1 h 15 min approximately symmetric about its vector of motion, beginning at 0545 UTC when a convective line roughly 275 km long produced contiguous reflectivity of 45 dBZ (fig. 3.4b). The MCS's symmetry was approximate in that reflectivity from cumulonimbi was highest at the center of the convective line, as in the schema of a symmetric system by Houze et al. (1990), but reflectivity in the stratiform region was highest on the MCS's left, as in their schema of an asymmetric system. (*Right* and *left* are from the perspective of the advancing MCS; its left side was generally to the northeast and its right side was generally to the southwest.) Late in the symmetric stage there were signs of the MCV in Doppler wind from KVNX, which is consistent with the possibility that heating in the stratiform region of the MCS generated the vortex.

Following the symmetric stage, the convective line remained vigorous and the MCS became highly asymmetric. Its transition to asymmetry began at 0715 UTC when a notch developed at the back edge of the stratiform region (*N1* in fig. 3.4c and d) and the convective line started to bow into the shape of an *S* (fig. 3.4c and d). Notch *N1* initially appeared to be the lingering signature of a gap where clusters *A* and *B* merged to form the incipient MCS (cf. fig. 3.4a and c). However, the notch persisted (fig. 3.4d). Smull and Houze (1987) found a similar coincidence between notching of a stratiform region and bowing of a convective line within the MCS of 22 May 1976. They hypothesized that strong inflow from behind the MCS in the middle troposphere dried the stratiform region, descended, and overtook the convective line, accelerating it forward. This same sequence of events most likely explains the asymmetric deformation of the MCS of 1 August 1996, although sparse coverage of the NPN prevented me from determining this conclusively.

During the hour after the initial bowing at 0715 UTC, the stratiform region became dramatically enhanced; reflectivity in active, embedded cumulonimbi exceeded 50 dBZ. As rainfall rate increased and the stratiform region expanded, a small cluster of heavily precipitating clouds overtook the existing stratiform region from behind and merged with it (not shown). It was at the time of the deformation of the convective line into the *S* and of this merger that the MCS became most asymmetric (fig. 3.4d).

3.3.3 *Maturity*

From 0900 to 1130 the MCS changed little, apart from some fracturing of the northern part of the convective line (the northern, concave, of the two curves that composed the *S* shape), which left only a single, convex arc of cumulonimbi at the leading edge of the MCS. In an approach similar to that of Hilgendorf and Johnson (1998), I designated this period as the mature stage because of the MCS's minimal change and because the system comprised the main reflectivity features that characterize asymmetric MCSs of this kind: a bowed convective line followed by stratiform precipitation—some of which includes enhanced radar returns—on the system's left side.

3.3.4 *Decline*

At 1100 UTC the right half of the MCS overtook in western Oklahoma a broad, seemingly unorganized north-south band of cumulonimbi (fig. 3.4e). The unorganized band effectively became the right side of the MCS's convective line. At 1145 UTC reflectivity within the convective line started to decrease from over 50 dBZ along most of its right half to only 40 dBZ in isolated patches by 1345 UTC (not shown).

Between 1145 and 1530 UTC a second notch formed at the back of the MCS (*N2* in fig. 3.4f and g). As notch *N2* advanced deeply and cyclonically into the left part of the stratiform region, reflectivity on the MCS's far left took on the shape of a hammer head (fig. 3.4g), and the stratiform region broke into spiral bands of clouds that continued to rain with reflectivity between 15 and 35 dBZ. This second notch, like the first, was almost certainly symptomatic of dry air intruding at the back of the MCS. Notches and spiral bands within stratiform regions that contain MCVs are common (e.g., Fritsch et al. 1994), but they do not accompany every MCV (e.g., Chong and Bousquet 1999), nor are they infallible signs of MCVs (e.g., Fortune et al. 1992).

At no time did any of our data expose an anticyclonic vortex on the right side the MCS of 1 August 1996, although vorticity there was often strongly negative from horizontal shear. Anticyclonic vortices are sometimes paired with cyclonic vortices in MCSs (e.g., Scott and Rutledge 1995), although the former tend to be smaller, weaker, and more short lived.

Table 3.1: Stages of the MCS of 1 August 1996 diagnosed from composite reflectivity.

Stage	Time (UTC)	Characteristics
prelude	0215–0330	scattered cumulonimbi form prior to the MCS
formation	0345–0415	three clusters of cumulonimbi merge
	0430–0530	indistinguishable clusters become the incipient MCS
development	0545–0700	MCS is quasi-symmetric with a linear convective line of reflectivity $\geq$45 dBZ
	0715–0845	MCS becomes asymmetric when the first of two notches develops at the back edge of the stratiform region and the convective line bows into the shape of an S.
maturity	0900–1130	northern part of the S-shaped convective line becomes fractured, otherwise the MCS changes little
decline	1145–1530	MCS weakens as a second notch develops at the back edge of the stratiform region; the convective line breaks apart; the northern side of the stratiform region takes on the appearance of a hammer head
dissipation	1545–0315	remnants of the MCS take the form of spiral bands that slowly dissipate, spotty new cumulonimbi grow among old cumulonimbi

3.3.5 Dissipation

In the lengthy final stage of the MCS, from 1545 UTC on 1 August through 0315 UTC on 2 August, the spiral bands slowly dissipated, and scattered new cumulonimbi grew in the remnants of the bands (fig. 3.4h). Clusters of cumulonimbi that I traced to these dissipating bands persisted through 2 August in Arkansas, Louisiana, and Mississippi, but no sustained mesoscale vortical patterns were visible in the clusters. Interestingly, there was a report of an F0 tornado beneath one fresh cumulonimbus within the dissipating spiral bands. The thin tornado lasted from 2105 to 2115 UTC and damaged trees in a rural area. How some MCVs foster new cumulonimbi in the wake of dissipating MCSs is an important and fascinating topic, although it is beyond the scope of this dissertation. The small body of published research on the subject includes papers by Raymond and Jiang (1990), Fritsch et al. (1994), and Trier et al. (2000a).

Chapter 4

KINEMATICS

4.1 Wind

Only the densest part of the NPN provided data that were sufficiently resolved to diagnose the mesoscale kinematical imprint of the MCS on its environment. This forced me to restrict my analyses to between 0900 and 1800 UTC, which encompassed the MCS's asymmetric period from shortly before maturity through dissipation (table 3.1). I refer to this nine-hour interval as the *period of detailed analysis.*

4.1.1 Synoptic background wind

The synoptic background wind over Kansas and Oklahoma veered from southeasterly near the ground to westerly between 800 and 700 hPa and west-northwesterly or northwesterly above that (fig. 3.2). It was northwesterly in the middle troposphere where the MCV formed (fig. 2.3a).

AT 1200 UTC, absolute vorticity at 500 hPa was between 6 and 10×10^{-5} m s^{-1} (fig. 4.1a), most of which was planetary vorticity. The zonal components of the gradients in absolute vorticity in figure 4.1a were due to a short-wave trough (fig. 3.1). Absolute vorticity in the synoptic wind was similar to absolute vorticity in the 12-h forecast by the Nested Grid Model (NGM) initialized at 0000 UTC on 1 August (cf. fig. 4.1a and b). Evidently, synoptic vorticity over Kansas and Oklahoma was largely due to phenomena predicted by the forecast model. The MCS did not exist at 0000 UTC, so it was not represented in the NGM's initialization, nor was the MCS predicted by the NGM, although the model did forecast widespread rain. Similarity between the forecast field that

did not include the MCS and what I have calculated to be synoptic background wind substantiates my method of discriminating between scales.

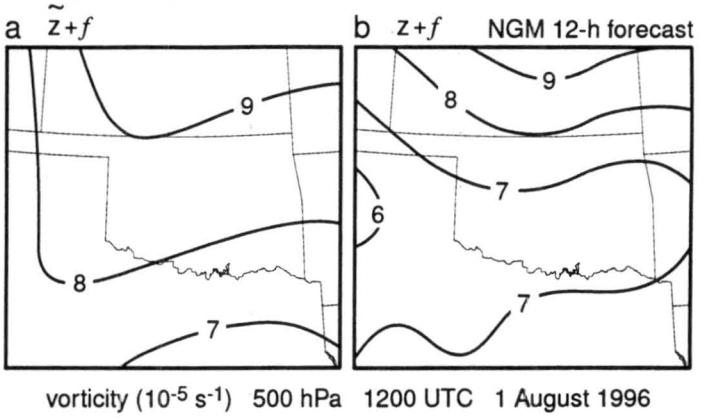

Figure 4.1: Absolute vorticity at 500 hPa at 1200 UTC on 1 August 1996. The panels show a) vorticity of the synoptic background wind and b) the NGM's 12-h forecast of vorticity from the model run initialized at 0000 UTC on 1 August 1996.

4.1.2 Mesoscale perturbation in wind

Observations from the NPN at 1200 UTC exemplify the mesoscale wind during the MCS's maturity (fig. 4.2), and observations from three hours later exemplify the mesoscale wind during the MCV's maturity (fig. 4.3). However, because no instrument platform was able to completely observe all of the important mesoscale structure of the system and vortex at every hour, I have chosen to summarize data from multiple hours and multiple platforms in the form of schemata (figs. 4.4 and 4.5).

During the MCS's maturity, the mesoscale perturbation in wind included a mesoscale updraft and downdraft, divergent outflow in the lower troposphere, divergent outflow in the upper troposphere, and an MCV centered in the middle troposphere (figs. 4.4 and 4.5). Apart from the MCV, these are the four primary mesoscale circulations portrayed in other depictions of wind within MCSs (e.g., Zipser 1977; Smull and Houze 1987; Johnson et al. 1990). Because these circulations appear in the mesoscale perturbation in wind, I conclude they were internal and fundamental to the MCS of

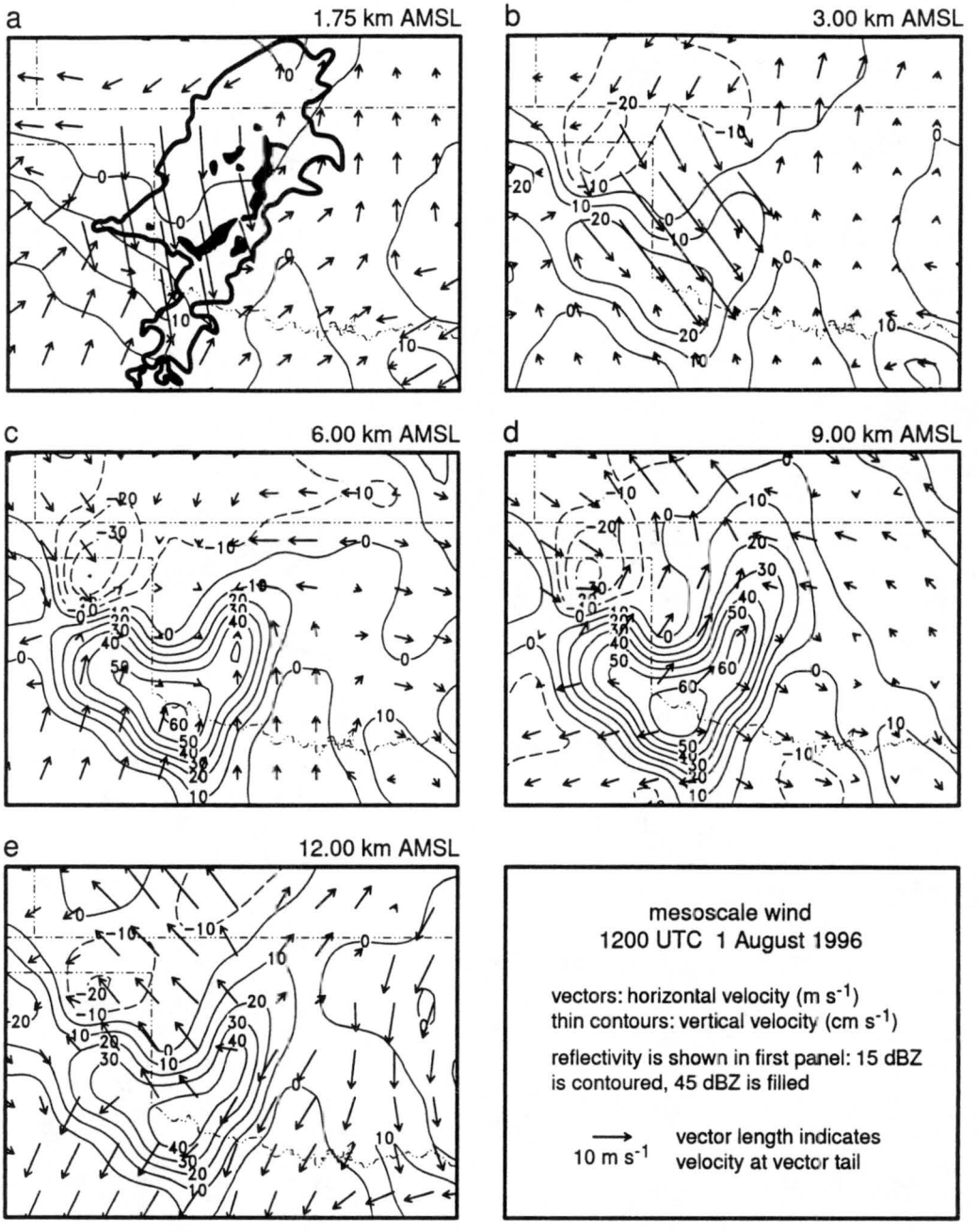

Figure 4.2: Three components of the mesoscale wind at 1200 UTC on 1 August 1996. The altitudes are a) 1.75 km, b) 3.00 km, c) 6.00 km, d) 9.00 km, and e) 12.00 km AMSL. Vectors represent horizontal velocity, and vertical velocity is contoured in thin lines every 10 cm s^{-1}. In the first panel, reflectivity of 15 dBZ is contoured in the thick line and >45 dBZ is filled.

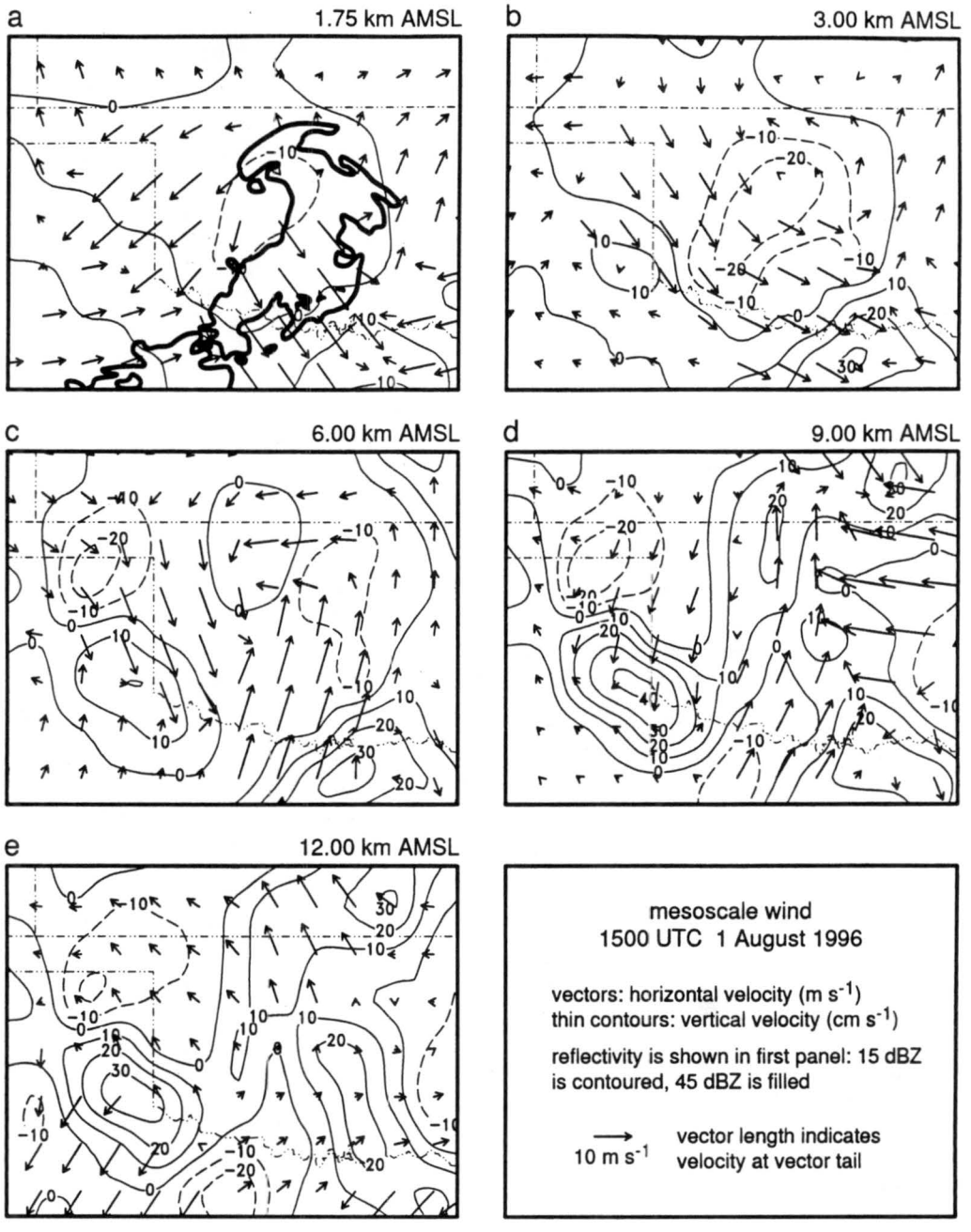

Figure 4.3: Three components of the mesoscale wind at 1500 UTC on 1 August 1996. The altitudes are a) 1.75 km, b) 3.00 km, c) 6.00 km, d) 9.00 km, and e) 12.00 km AMSL. Vectors represent horizontal velocity, and vertical velocity is contoured in thin lines every 10 cm s^{-1}. In the first panel, reflectivity of 15 dBZ is contoured in the thick line and >45 dBZ is filled.

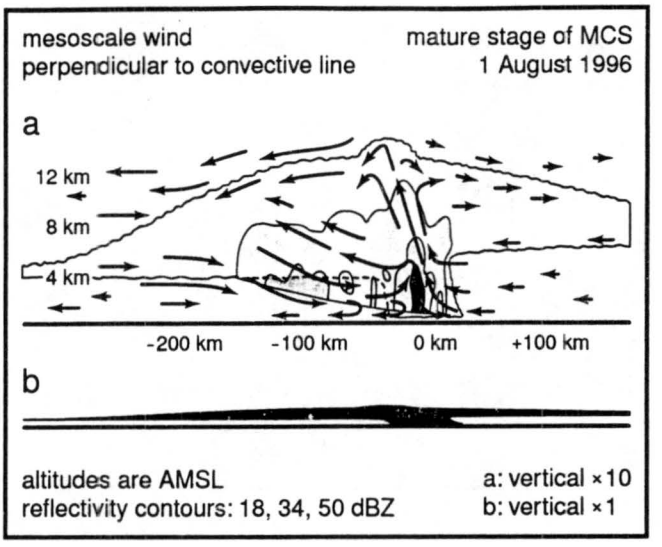

Figure 4.4: Schematic cross sections of the mature MCS on 1 August 1996. Depicted are reflectivity and the cross-line component of the mesoscale perturbation in wind. Arrows are a hybrid of vectors and streamlines, so their lengths roughly indicate relative wind speed of consistently observed flows along various locations in the MCS as determined from the NPN at 1200 UTC and from cross sections of WSR-88D Doppler velocity from Oklahoma City, OK at 1233 to 1320 UTC. Contours, from outer to inner, are cloud edge and reflectivity of 18, 35, and 50 dBZ. Reflectivity is at 1233 UTC along the cross section shown in figure 3.4f. The bottom edge of the reflectivity cross section is due to the lower limit of the lowest radar scan. Cloud top is from a GOES 8 IR image at 1215 UTC along the same cross section; cloud bottom is estimated from GCIP soundings at 1200 UTC and from other studies of MCSs. Height is exaggerated by a factor of ten in the top schema; the bottom schema is an unexaggerated silhouette.

1 August 1996; they were not merely *apparent* circulations that resulted from a ground-based frame of reference or from the superposition of the MCS's flow, the environmental flow, and the translational motion of the MCS relative to the environmental flow. Others have concluded the same about different MCSs (e.g., Smull and Houze 1987).

A mesoscale rear inflow jet entered the MCS at the back edge of the stratiform region, primarily below 8 km above mean sea level (AMSL) (fig. 4.4a, which is a synthesis of data from multiple sources, as explained in the caption), in the middle part of the MCS, away from its left and right ends (fig. 4.5). This inflow jet was the rear part of the mesoscale downdraft. Air in the downdraft flowed through the lower part of the anvil and beneath the anvil's base, then descended

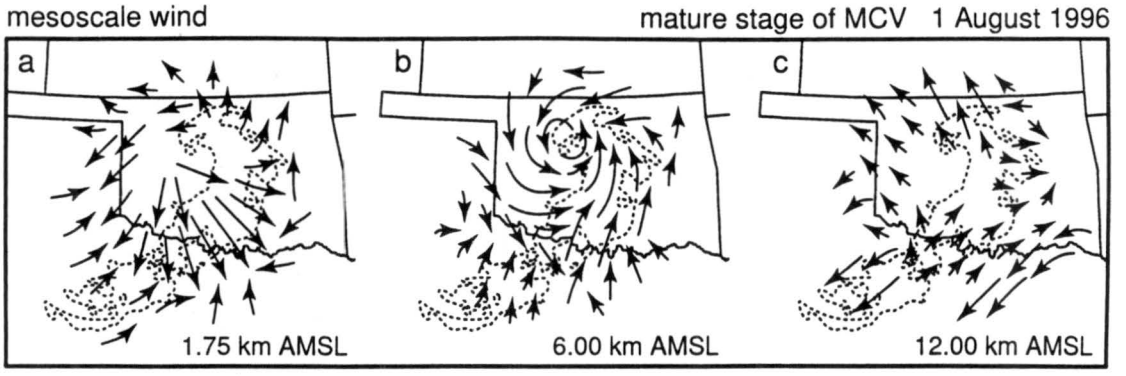

Figure 4.5: Schemata of the mesoscale perturbation in wind during the MCV's maturity on 1 August 1996. Horizontal wind is at altitudes of a) 1.75 km, b) 6.00 km, and c) 12.00 km AMSL. Arrows are a hybrid of vectors and streamlines, so their lengths roughly indicate relative wind speed. The contour of 15 dBZ reflectivity within the MCS is dashed.

beneath a mesoscale updraft (fig. 4.4a). Descent in the mesoscale downdraft was strongest between 2 and 6 km AMSL. (In figure 4.4, ground level is approximately 0.3 km AMSL.) The rear inflow jet is apparently one reason that rain-free air advanced into the stratiform region, forming the second notch as the MCS decayed. There is evidence that in some places the mesoscale downdraft continued through the convective line and emerged in front of the leading cumulonimbi. For example, in the middle of the mature MCS at 1250 UTC, a rear-to-front (RTF) flow (both in a storm-relative and an environment-relative framework) in the lower troposphere extended farther eastward than the high reflectivity of the convective line (fig. 4.6).

More than one of the mechanisms listed in section 1.1 may explain the RTF flow in the mesoscale downdraft. Level II reflectivity and Doppler velocity from Oklahoma City depict convective updrafts tilted upshear (fig. 4.4a), which is necessary for the middle-tropospheric low of LeMone (1983) that is known to accelerate RTF flow in stratiform regions. A local minimum in geopotential height above the cold pool that was detected by the Oklahoma Mesonet (not shown) could also have been partly responsible for the mesoscale downdraft (Brown 1979; Gallus and Johnson 1992). In addition, a fraction of the mesoscale downdraft may have been return flow in a

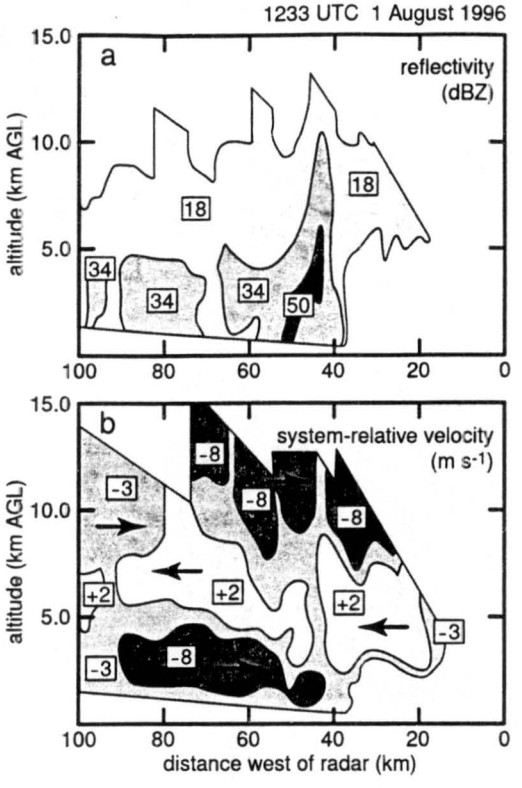

Figure 4.6: Cross section of level II data through the middle of the mature MCS at 1233 UTC on 1 August 1996. Panels show a) regions of reflectivity enclosed by contours of 18, 34, and 50 dBZ; and b) regions of system-relative radial wind enclosed by contours of 8 and 3 m s^{-1} toward the radar (westerlies), and 2 m s^{-1} away from the radar (easterlies). The section was taken along the 270° radian.

buoyancy roll (Mapes 1993). Finally , the horizontal flow in the mesoscale downdraft was part of the tangential northwesterly and westerly wind around the southwestern and southern parts of the MCV, which was located on the left side of the MCS (fig. 4.5b). In this way there was a symbiosis between the rear-inflow jet and the MCV. Each reinforced the circulation of the other, and the location of the jet on the right edge of the MCV ensured that the strong shears in the jet did not rip apart the vortex.

A mesoscale updraft lay above the mesoscale downdraft (fig. 4.4a). Level II Doppler velocity from Oklahoma City shows that in cross section the surfaces of highest wind speeds in both drafts

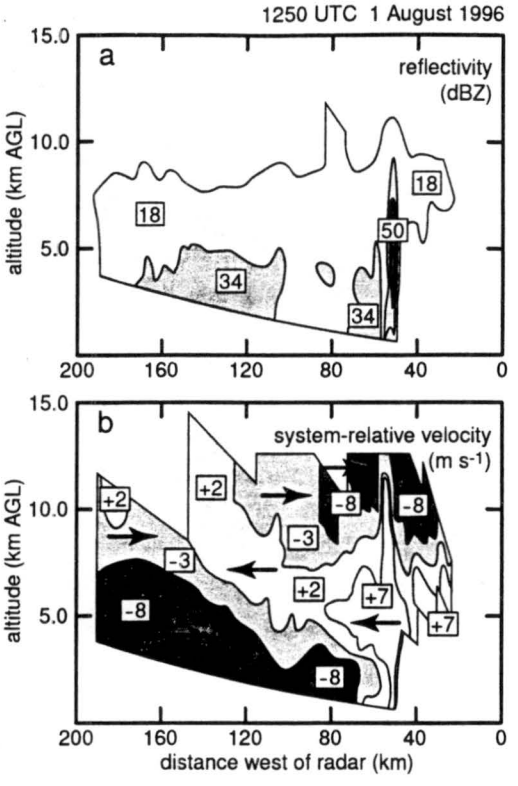

Figure 4.7: Cross section of level II data through the middle of the mature MCS at 1250 UTC on 1 August 1996. Panels show a) regions of reflectivity enclosed by contours of 18, 34, and 50 dBZ; and b) regions of system-relative radial wind enclosed by contours of 8 and 3 m s^{-1} toward the radar (west-northwesterlies), and 2 and 7 m s^{-1} away from the radar (east-southeasterlies). The section was taken along the 300° radian.

were concave, as seen from above, between the convective line and the enhanced reflectivity in the stratiform region. The mesoscale updraft originated at about 5 km AMSL along the back edge of updrafts in the convective line. Also apparent in Doppler velocity is a horizontally narrow zone of convective downdrafts along the back edge of the convective updrafts, near the origin of the mesoscale updraft. A similar zone of convective downdrafts appears in figures by Houze (1989) and Biggerstaff and Houze (1993), among others. The mesoscale updraft was at times distinct to an altitude of roughly 10 km AMSL farther than 150 km behind the convective line. Data from the NPN suggest that the Coriolis force turned the mesoscale updraft to the right as it ascended (fig. 4.5a and b),

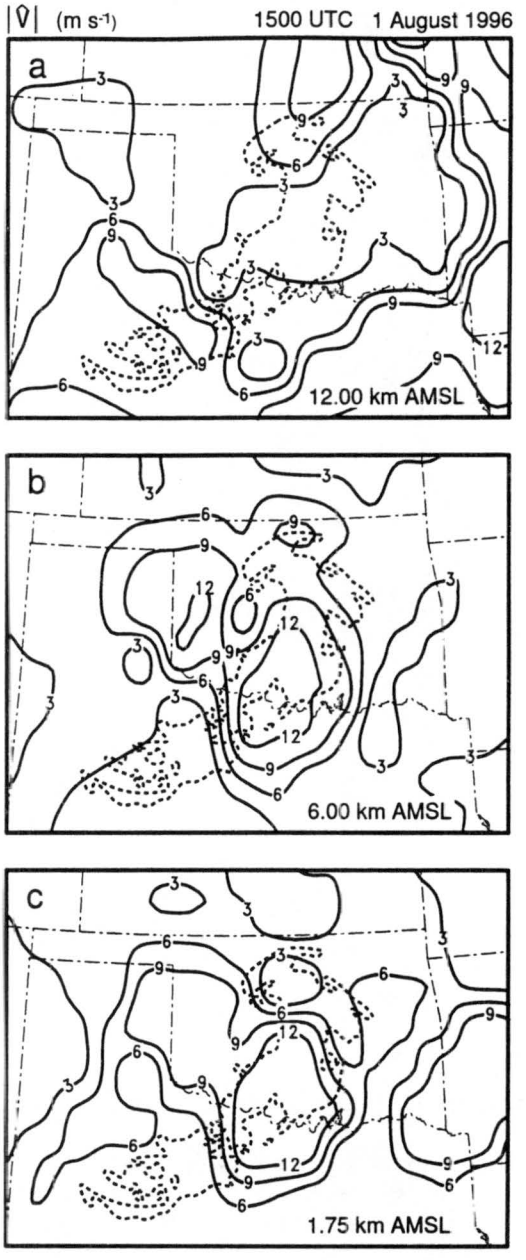

Figure 4.8: Speed of the mesoscale perturbation in wind at 1500 UTC on 1 August 1996. Contours are every 3 m s^{-1} at a) 12.00, b) 6.00, and c) 1.75 km AMSL. The contour of 15 dBZ reflectivity within the MCS is dashed.

in the manner described by Skamarock et al. (1994) and Scott and Rutledge (1995). Locally high wind speed in the divergent southeasterly flow on the north side of the MCS at 12 km AMSL—

where I later show upper-tropospheric divergence above the MCV was maximized—appeared to be part of the veering, ascending mesoscale updraft that was exiting the cloud and precipitation of the MCS (fig. 4.5c). These altitudes are above echoes returned to the WSR-88D at Oklahoma City, so I cannot confirm this speculation with more resolved data. Air in slanted updrafts of the convective line decelerated when beyond its level of buoyant equilibrium, which also contributed to divergent outflow in the upper troposphere (fig. 4.4a).

At 1.75 km AMSL—where I later show lower-tropospheric divergence in the MCV was maximized—diverging air beneath and behind the precipitation of the stratiform region converged with environmental air in a ring around the perimeter of the MCS's reflectivity (fig. 4.5a). Convergence in this ring was greatest near the southeastern and southern perimeter. Numerical simulations by Skamarock et al. (1994) demonstrated that such locally maximized convergence on the right side of a convective line characterizes MCSs that mature where the vertical component of planetary vorticity is large. Divergent northwesterly wind at 1.75 km AMSL behind the precipitation of the stratiform region was likely the terminus of the mesoscale downdraft (fig. 4.4a).

Air descended broadly and weakly along the top of front-to-rear (FTR) flow behind the convective line (fig. 4.4a). Johnson et al. (1990) noted broad descent at a similar altitude in the MCS of 10–11 June 1985. In that MCS, descent was in storm-relative flow within isentropic layers that sloped downward away from the convective line along the top of the stratiform anvil. That explanation is consistent with data from the MCS of 1 August 1996.

As the caption states, cloud top in figure 4.4 is based on infrared data from GOES 8. The slope of the cloud top is steeper than the slopes of clouds in schemata by Houze et al. (1989), Biggerstaff and Houze (1991), and others, so I scrutinized channels one and three from GOES 8 and checked soundings to the west of the MCS to determine whether thin, anvil cirri in the upper troposphere may have escaped detection in the infrared channel. I found no evidence that my depiction of cloud top is wrong but cannot completely rule out a misdiagnosis. One possible explanation for lack of high clouds well behind the MCS is that a region of dry air in the upper troposphere lay immediately to the west of the center of the MCS's cloud shield (not shown).

Most of the mesoscale perturbation in wind in the leading anvil was away from the convective line (fig. 4.4a). This perturbation was reinforced by synoptic northwesterlies, relative to the system, in the upper troposphere (fig. 4.7). Advection of hydrometeors by the relative total wind was no doubt responsible for the leading anvil. However, near the base of the cloud at about 6 km AMSL, both the perturbation in wind and the total wind were toward the convective line, not away from it. Collocation of leading anvil and rearward flow was explained by Smull and Houze (1985). They found that hydrometeors advected ahead of a convective line in RTF flow can fall out of that flow into FTR inflow, which advects the hydrometeors back toward the convective line.

The magnitude of the mesoscale perturbation in wind was asymmetric about the MCS at some altitudes. In the lower and middle troposphere, the mesoscale perturbation in wind covered a larger area behind the stratiform region than ahead of the convective line (fig. 4.8b and c). In particular, at 6.0 km AMSL a mesoscale perturbation in wind faster than 6 m s^{-1} extended farther than 300 km behind the back edge of the stratiform region's reflectivity (fig. 4.8b). This was mainly the mesoscale downdraft (figs. 4.4 and 4.5b). Evidently, the MCS generated its own rear inflow jet from accelerations in the middle troposphere; the jet was not due to strong northwesterly wind in the upper troposphere that was drawn downward by the MCS, although the system certainly did vertically transport some horizontal momentum. In the lower troposphere, the mesoscale perturbation in wind displayed a similar asymmetry. However, in the upper troposphere, the asymmetry was reversed in some cases (fig. 4.8a), or, at times for which figures are not shown, the flow was generally symmetric. According to Pandya and Durran (1996), Nachamkin and Cotton (2000), and others, such altitude-dependent asymmetries are symptoms of vertical shear's ability to tilt and horizontally arrange heating and cooling in an MCS. In particular, Pandya and Durran found that in their simulated squall line a deep, rearward-leaning heat source trailed by a heat sink focused low-frequency energy in the direction of that tilt. I cannot rule out the possibility that some of the perturbation in wind depicted in figure 4.8 was due to cumulonimbi unrelated to the MCS of 1 August 1996, but the effect was not great. The two largest masses of cumulonimbi that were closest to the MCS were in northeastern Kansas and Louisiana (not shown), quite far from the system.

4.1.3 Vertical wind shear

As the MCS matured, decayed, and began to dissipate, mesoscale and synoptic vertical wind shear in the lower and middle troposphere decreased overall at the center of the MCV (fig. 4.9). According to established terminology (e.g., Brandes 1990; Davis and Weisman 1994; Pandya et al. 2000), shear from 0.5 to 2.5 km AGL in the synoptic environment (dotted line in fig. 4.9) was moderate while the MCS was asymmetric from 0900 to 1500 UTC, then became weak as the MCS dissipated after 1600 UTC. Synoptic shear from 2.0 to 6.0 km AGL (dash-dotted line in fig. 4.9) can probably be described as moderate at all times.

The most consistent decrease in vertical shear at the MCV's center from 0900 to 1800 UTC was in the mesoscale perturbation in wind (dashed and solid lines in fig. 4.9) . The most precipitous drop was between 1100 and 1300 UTC when the convective line began to dissipate and the second notch was deforming the back edge of the stratiform precipitation (fig. 3.4f). During these two hours the MCV deepened substantially; the top of the column of positive vorticity rose from approximately 5.5 km AGL to higher than 9.0 km AGL (not shown). It is possible that the decrease in mesoscale shear was partly because wind became more vortical at increasingly higher altitudes. The direction of the wind would have become more vertically uniform, but only if the MCV was not greatly tilted, which it may have been. After 1700 UTC, the mesoscale shear began to increase in the lower and middle troposphere, perhaps as the vortical flow in the MCV began to lose coherence.

Overall reductions in the mesoscale and synoptic vertical shear during the period of detailed analysis were interrupted by brief increases, especially in the former. Some single-hour spikes in mesoscale shear, such as at 1100 UTC (dashed and solid lines in fig. 4.9), probably resulted from the NPN's inconsistent sampling of the MCS. However, inconsistent sampling does not explain the prolonged local maximum in lower-tropospheric synoptic shear from 1000 to 1400 UTC (dotted line in fig. 4.9). The short-wave trough, not the MCS, was responsible for this sustained increase. As it moved through the densest part of the NPN, the trough turned synoptic wind at 2.5 km AGL sharply from westerly to northwesterly (not shown). Then after the trough passed and the wind backed, synoptic shear in the lower troposphere decreased.

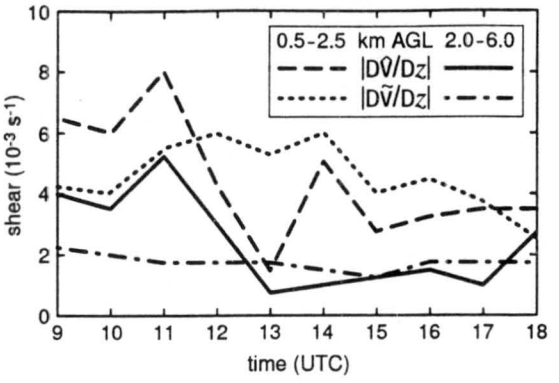

Figure 4.9: Vertical wind shear in the MCV from 0900 to 1800 UTC on 1 August 1996. Shears (10^{-3} s^{-1}) are at the MCV's center in the lower troposphere (0.5–2.5 km AGL) for the mesoscale perturbation in wind (dashed) and synoptic wind (dotted), and in the middle troposphere (2.0–6.0 km AGL) for the same components (solid and dash-dotted, respectively).

If the effects of the short-wave trough are discounted, synoptic shear in both the lower and middle troposphere decreased overall through the period of detailed analysis. This suggests that as the MCS aged it altered the kinematics of its environment in a way that increasingly favored an MCV; Davis and Weisman (1994) and Trier et al. (2000b) showed that MCVs are more likely in weakly sheared rather than strongly sheared environments.

The fact that over the entire period of detailed analysis shears in the mesoscale wind were generally as large as those in the synoptic wind may force researchers to rethink how we assess the kinematical environment of an MCV. An average of environmental soundings well away from an MCV or MCS probably does not accurately represent the shear immediately surrounding an MCS, because any system that generates an MCV creates its own shear. The shear an MCV experiences must be a combination of the environmental shear and that system-scale shear.

Possible interaction between shear and the MCV's tilt

As mentioned in section 2.12, the available data did not allow me to determine the tilt of the MCV. Even so, a comment on how tilted vortices interact with shear is appropriate.

The tilt to a vortex allows it to resist some destruction from shear. Vertical shear differentially advects the lower and upper layers of a vortex away from each other. At the same time, in a tilted vortex the mutual advection of each layer by the other causes the vortex's axis to process cyclonically about its mid-level center (Jones 1995). The procession slows with time until it stops when the vortex's tilt opposes the tilt due only to differential advection by vertical shear. In this way the shear's destructive effects are reduced. Any detailed study of the longevity and tilt of MCVs should include an analysis of these phenomena, but to do so will take a data set far more resolved than the one available to me.

4.2 Average kinematics over the MCV

Data from the NPN averaged over 3-h periods and over a $2° \times 2°$ area centered on the MCV in the middle troposphere reveal the persistent circulations that shaped the MCS (fig. 4.10). These persistent circulations were the mesoscale updraft and downdraft that met in a layer of convergence in the middle troposphere, divergent outflows in both the lower and upper troposphere, and the MCV. (References to *vertical velocity, divergence,* and *vorticity* in this section are to the temporal and spatial averages of those fields, unless otherwise stated.)

Profiles of vertical motion, divergence, and vorticity for the total wind centered on the MCV in the middle troposphere are generally similar to such profiles in other studies based on both observations and numerical simulations (e.g., Brandes 1990; Zhang 1992; Scott and Rutledge 1995). I address dissimilarities where appropriate.

One consistent result among studies of MCSs is that the magnitudes of kinematical terms calculated over stratiform regions depend on whether data are fine or coarse and on how those data are averaged. Fine data and minimal averaging produce high magnitudes. For example, some researchers have calculated middle-tropospheric maxima in vorticity within stratiform regions to be of order 1×10^{-6} s^{-1} (e.g., Cotton et al. 1989, with composite data), others have calculated maxima one hundred times larger (e.g., Chong and Bousquet 1999, with Doppler data). My calculations are much closer to the latter than to the former.

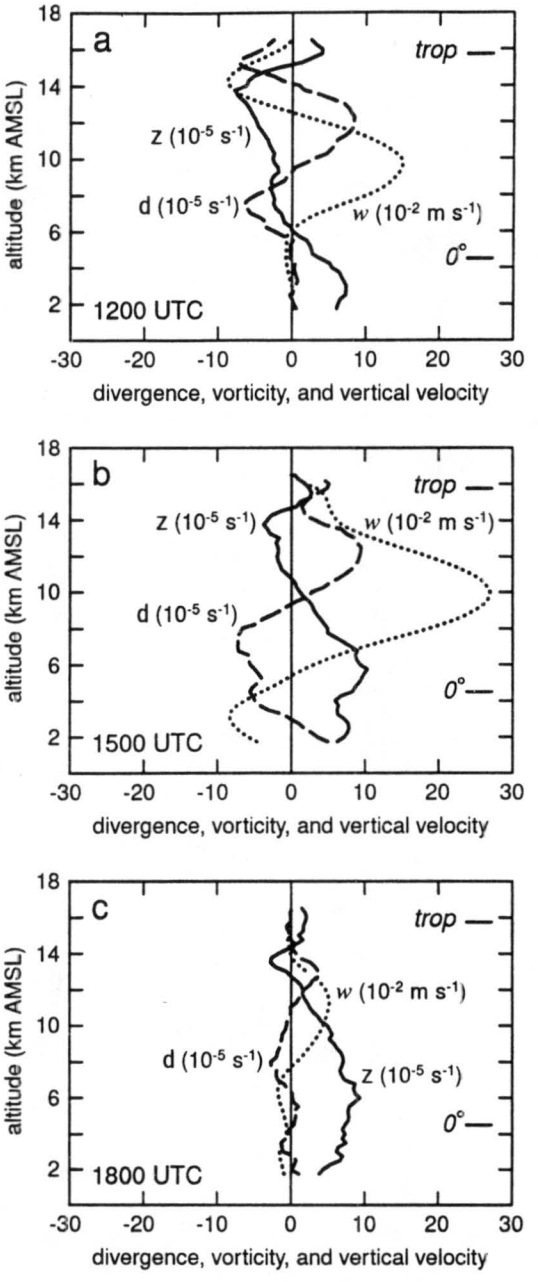

Figure 4.10: Kinematical averages in the MCV from 1200 to 1800 UTC on 1 August 1996. Relative vorticity (10^{-5} s^{-1}) of observed wind is solid, divergence (10^{-5} s^{-1}) is dashed, and vertical velocity (10^{-2} m s^{-1}) is dotted. Profiles are for a 2°×2° area centered on the MCV in the middle troposphere, averaged over 3 h ending at the time labeled. The levels of 0°C in the environment and of the tropopause are marked along the right side of each panel.

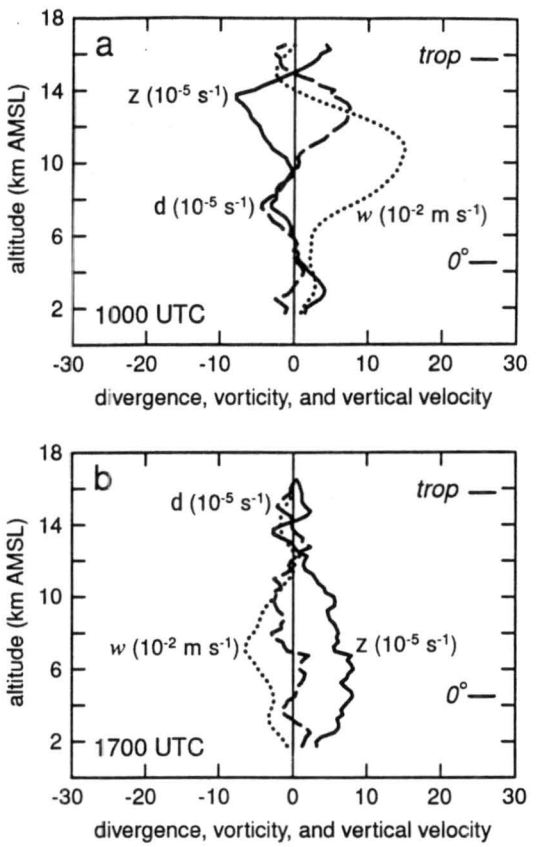

Figure 4.11: Kinematical averages in the MCV at 1000 and 1700 UTC on 1 August 1996. Relative vorticity (10^{-5} s^{-1}) of observed wind is solid, divergence (10^{-5} s^{-1}) is dashed, and vertical velocity (10^{-2} m s^{-1}) is dotted. Times are a) 1000 and b) 1700 UTC. Profiles are for a 2°×2° area centered on the MCV. Unlike in fig. 4.10, profiles are not for 3-h averages. The levels of 0°C in the environment and of the tropopause are marked along the right side of each panel.

4.2.1 Vertical velocity

The mesoscale updraft preceded the mesoscale downdraft (cf. dotted lines in fig. 4.10a and b). This is because in the archetypal MCS—and in the MCS of 1 August 1996—mechanisms that accelerate a mesoscale updraft appear before mechanisms that accelerate a mesoscale downdraft (sec. 1.1). A mesoscale updraft originates primarily from the convective line. A mesoscale downdraft originates from a combination of the convective line and the stratiform region, including the cold pool in the lower troposphere beneath the trailing anvil. An expansive stratiform region and cold

pool often do not appear until 4–8 h into the lifetime of an MCS (Smull and Houze 1985). Cotton et al. (1989) found that a mesoscale downdraft did not exist much before the mature stage of their composite MCS.

By the time vorticity in the MCV of 1 August 1996 reached its maximum at 1500 UTC, both mesoscale drafts were present and at their strongest (fig. 4.10b). The temporally and spatially-averaged maximum velocity of the mesoscale updraft was nearly 30 cm s^{-1}; the mesoscale downdraft reached an average velocity of nearly -10 cm s^{-1}. As mentioned in section 1.1, ascent in a mesoscale updraft is due to positively buoyant, dissipating cells from a convective line, and from heating by exothermic phase changes of water within the mesoscale updraft. Although the contour interval of 15 dBZ in figure 3.4 does not illustrate it, between 1200 and 1500 UTC the stratiform region contained large and persistent areas of enhanced reflectivity between 40 and 45 dBZ, a sign that hydrometeors were growing and heating the mesoscale updraft (Biggerstaff and Houze 1991), even though the MCS as a whole was dissipating. The mesoscale downdraft strengthened at 1500 UTC when erosion of the back edge of the stratiform region was a sign of the mechanisms that drive descent in such drafts: sublimative and evaporative cooling (Rutledge et al. 1988).

An additional indication that microphysics were important in forcing the two mesoscale drafts is that the average altitude that divided descent from ascent in the stratiform region (5.25 km AMSL) and the average altitude of 0°C in the environment (4.48 km AMSL) differed by only 0.77 km (fig. 4.10b). This difference is within the commonly observed range of 0 to 2 km (Houze 1993).

Unrepresentative data at 1800 UTC, perhaps from convective updrafts in a few fresh cumulonimbi, corrupted the average vertical velocity between 1500 and 1800 UTC, so changes in the mesoscale drafts are not accurately portrayed by figure 4.10c. In the figure, both drafts seem to have been present, although weak, which is not consistent with other studies in which mesoscale updrafts disappeared while mesoscale downdrafts deepened and persisted in late stages of MCSs that contained MCVs (e.g., Brandes 1990; Scott and Rutledge 1995). However, the areally averaged profile of vertical motion at 1700 UTC alone—not averaged over three hours—is qualitatively almost identical to profiles in the other studies mentioned, which gives it credence. At 1700 UTC

there was no mesoscale updraft, and the top of the mesoscale downdraft was at about 11 km AMSL (fig. 4.11b).

4.2.2 Divergence

Convergence was conspicuously small through the depth of the MCV (that is, below 6 km AMSL) between 0900 and 1200 UTC (dashed line in fig. 4.10a), which suggests that tilting may have played a prominent role in the initial formation of the MCV. Unfortunately, at the time the MCV first appeared it was well northwest of the part of the NPN sufficiently dense for detailed analysis, so I could not determine the source of initial vorticity (section 4.3 provides more details of this). In an MCV simulated by Zhang (1992), a vortex whose final strengthening was mainly from convergence—as was the case with the MCV of 1 August 1996—did, in fact, begin mainly as tilted horizontal vorticity.

Above the growing MCV lay convergence centered at 7.5 km and strong divergence centered at 12.0 km AMSL (fig. 4.10a). Divergence in the upper troposphere, which persisted at various strengths over the entire period of detailed analysis (fig. 4.10), is partially the signature of upper tropospheric high pressure that is a fundamental feature of MCSs in general, not just of those that generate MCVs (sec. 1.1).

At 1500 UTC (fig. 4.10b), the vertical distribution of divergence was very similar to that calculated by Cotton et al. (1989) for the average stratiform region of a composite MCS (their fig. 12). In the MCS of 1 August 1996, divergence first appeared in the lower troposphere, below about 3 km AMSL. It was equated with overturning and horizontal diffluence (provided the wind speed did not change much) in the mesoscale downdraft as it neared the ground, or perhaps as it neared the top of stable air in the cold pool. The middle troposphere above was convergent where the horizontally opposed mesoscale up- and downdrafts met. The profile of divergence in the upper troposphere centered at about 12 km AMSL was nearly identical to that from three hours earlier (cf. fig. 4.10a and b). Throughout the nine hours of analysis, divergence in this part of the upper troposphere varied with the mesoscale updraft, whereas divergence in the lower troposphere varied

with the mesoscale downdraft (fig. 4.10). The vertical distribution of divergence at 1500 UTC was also consistent with buoyancy rolls generated by a combination of convective and stratiform heating, which Mapes (1993) illustrated. Divergence in the lower and upper troposphere may have been the outgoing branches of the $l = 2$ roll in his figure 6, and convergence in the middle troposphere may have been the incoming branch.

Divergence, both positive and negative, weakened markedly throughout the troposphere during the final three hours of analysis (fig. 4.10c). Maximum divergence rose in altitude as the MCS dissipated, a trend also apparent in figures by Cotton et al. (1989) and Brandes (1990). Upper-tropospheric divergence persisted, although it was considerably weaker than three hours earlier. This weakening is substantially different from the dramatic increase in divergence within the decaying composite MCS of Cotton et al. (1989); the reason for the difference is unclear. Other studies specifically of MCSs that generated MCVs show trends in divergence more like I found (e.g. Brandes 1990; Chong and Bousquet 1999; Bousquet and Chong 2000). I reject the possibility that poor sampling by the NPN may have left undetected a spike in upper-tropospheric divergence, because there was no pronounced fall-off in detected vorticity within the MCV during the last three hours of analysis (cf. fig. 4.10b and c).

4.2.3 Vorticity

Over the period of detailed analysis, the MCV deepened and strengthened as the MCS matured and dissipated, until the vortex occupied almost the entire troposphere (solid lines in fig. 4.10). According to the Oklahoma Mesonet, the MCV appeared even to reach the ground; by 1900 UTC a broad vortical circulation was centered at the back edge of the southern spiral band of the decaying MCS (fig. 4.12).

Two features in figure 4.12 are signs that the MCV may not have been highly tilted. First, the center of circulation at the ground at 1900 UTC was very near the center of circulation in the middle troposphere (the gray circle in the figure). Second, no pronounced mesoscale low appeared near the MCV—the low in western Oklahoma was most likely a vestigial wake low of the kind described by

Johnson and Hamilton (1988). Highly tilted MCVs are more likely to generate mesoscale lows and highs at the ground because the warm air in the upper part of a tilted MCV's core is horizontally offset from the cold air in the lower part of core, which means that perturbations in mass equated with the two perturbations in temperature do not vertically cancel.

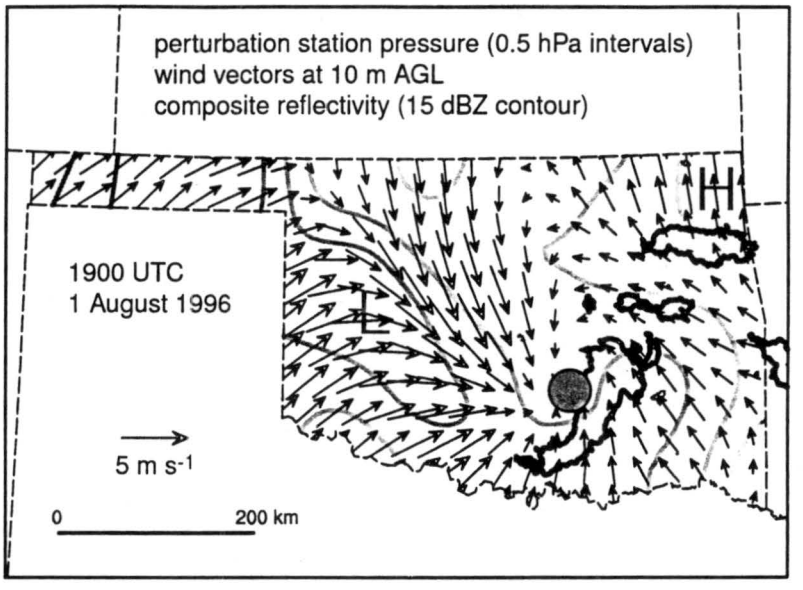

Figure 4.12: Radar reflectivity and surface conditions within the Oklahoma Mesonet at 1900 UTC on 1 August 1996. Surface pressure is contoured every 0.5 hPa in gray; values are deviations from a state-wide mean and darker grays indicate lower pressure. Vectors depict wind at 10 m AGL. The thick black contours outline reflectivity $\geq$ 15 dBZ. The gray circle marks the middle-tropospheric center of the MCV.

Not only did the top and, perhaps, the bottom of the MCV change altitude with time, so did the maximum in vorticity. Positive vorticity in the vortex originated at about 3 km AMSL (fig. 4.11a), the altitude of its average maximum from 0900 to 1200 UTC (fig. 4.10a). The top of the MCV and the level of maximum vorticity both ascended between 1200 and 1500 UTC as the vortex strengthened (fig. 4.10b). Then the height of maximum vorticity remained approximately fixed at 6 km AMSL for the remainder of the period of detailed analysis (fig. 4.10c). The long-lived simulated MCV of Zhang and Fritsch (1988) behaved similarly: the height of maximum vorticity varied little for the first two hours of the MCV's lifetime, rose abruptly as the MCV strengthened,

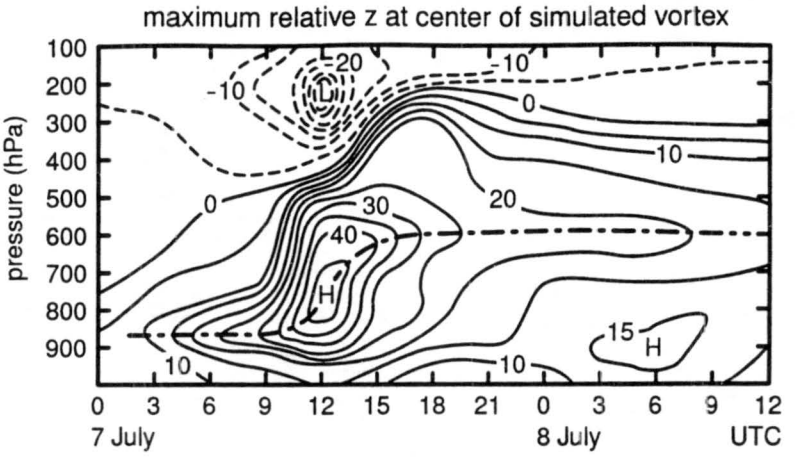

Figure 4.13: Temporal change in maximum relative vertical vorticity in the numerically simulated MCV of 6–7 July 1982. Contours are every $5\times10^{-5}s^{-1}$. Negative contours are dashed. [Adapted from a figure by Zhang and Fritsch (1988).]

then varied little after that (fig. 4.13). Rogers and Fritsch (2001) simulated an MCV whose vorticity maximum ascended with time, even while the base of the vortex descended to the ground. Conversely, Chen and Frank (1993) simulated an MCV whose vorticity maximum descended, not ascended with time. Few empirical studies recount temporal variations of vorticity within an MCV, but, among these few, Menard and Fritsch (1989) and Johnson and Bartels (1992) did find that maxima in vorticity ascended with time in two MCVs. [The MCV of 6–7 July 1982, which Menard and Fritsch studied, was the same MCV simulated by Zhang and Fritsch (1988)]. These and other studies (e.g., Zhang 1992; Davis and Weisman 1994) strongly suggest the intriguing possibility that some MCVs' life cycles can be divided into stages that are characterized by dominant sources of vorticity concentrated at distinctive altitudes. If so, a sudden ascent or descent of maximum vorticity within an MCV may signal a transition from one of these stages to another.

It is not surprising that the MCV of 1 August 1996 grew stronger even while the MCS decayed. Although the strength and areal extent of radar echoes in the convective line decreased beginning as early as 1145 UTC, the stratiform region remained vigorous until 1430 UTC (fig. 3.4), with large patches of reflectivity greater than 40 dBZ, and it is heating in the stratiform region, not

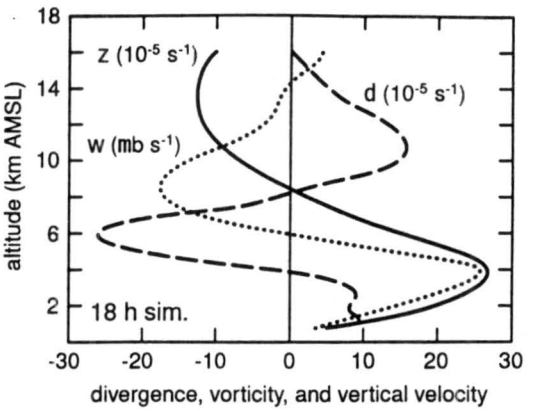

Figure 4.14: Kinematical averages in the numerically simulated MCV of 10–11 June 1985. Profiles are for the mature stage of the MCV and the decaying stage of the MCS. Relative vorticity (10^{-5} s^{-1}) is solid, divergence (10^{-5} s^{-1}) is dashed, and vertical velocity (μb s^{-1}) is dotted. Profiles are for a 100×100 km area centered on the MCV after an 18 h simulation. [Adapted from a figure by Zhang (1992).]

heating in the convective line, that generates MCVs (Hertenstein and Schubert 1991). When Zhang (1992) simulated the MCS of 10–11 June 1985, he, too, found that the MCV generated by that system grew stronger as the system decayed. Indeed, the kinematical profiles from the decaying stage of Zhang's system match quite closely the kinematical profiles for the same stage of the MCV of 1 August 1996 (cf. figs. 4.10b and 4.14). (Note that Zhang depicted vertical velocity in units of pressure, not altitude.)

The great depth of the MCV from 1500 to 1800 UTC has precedent. The simulated MCV of Chen and Frank (1993) had a top near 200 hPa, which would be 12.4 km AMSL in our case. Observed MCVs of Brandes (1990) and Bousquet and Chong (2000) had tops near 11 km AMSL.

The shallow, weakly negative vorticity above the MCV of 1 August 1996 is the signature of planetary vorticity's effects on divergent outflow from high pressure in the upper troposphere. Others have also noted such a feature (e.g., Brandes 1990; Johnson and Bartels 1992; Bousquet and Chong 2000).

4.3 Vorticity budget

According to (2.1), convergence, tilting, and unresolved effects contributed the most to net changes in the MCV as it matured, and prominent sources and sinks of vorticity existed in both the synoptic and mesoscale components of the wind.

4.3.1 Total wind

In the total wind there were only two positive sources of vorticity in the lower troposphere at the altitude of the developing MCV between 0900 and 1200 UTC: tilting (fig. 4.15a) and unresolved effects (fig. 4.16). Because the vortex had already formed by the start of the period of detailed analysis, I could not determine the source of vorticity in the incipient vortex. Even so, figure 4.15a suggests that tilting may have played the largest role on resolved scales, which would be consistent with studies by Zhang (1992) and Davis and Weisman (1994), whose simulated MCVs began primarily from tilting, then in maturity strengthened from convergence.

The MCV of 1 August 1996 grew deeper and stronger between 1200 and 1500 UTC primarily from convergence of positive absolute vorticity in the middle troposphere (fig. 4.15b). Planetary and relative vorticities contributed almost equally (not shown). If not for divergence of planetary vorticity in the upper troposphere, the tendency due to divergence there at 1500 UTC would have been positive as well, because upper-tropospheric relative vorticity was negative (fig. 4.10b). Indeed, because divergence and relative vorticity were approximately anticorrelated about zero, any deep layers of negative tendency due to divergence must have been from divergent wind acting on planetary vorticity, because divergence of negative relative vorticity and convergence of positive relative vorticity cannot produce a negative tendency. Davis and Weisman (1994) alluded to this. At the same time that convergence of absolute vorticity generated relative vorticity in the lower and middle troposphere, the mesoscale updraft advected that vorticity upward (fig. 4.15b). However, positive vertical advection of vorticity was overwhelmed by all the other resolved sinks. In particular, horizontal advection decreased vorticity from the lower through the upper troposphere, which is partly a result of the way vorticity was averaged; as long as the $2° \times 2°$ area of averaging remained

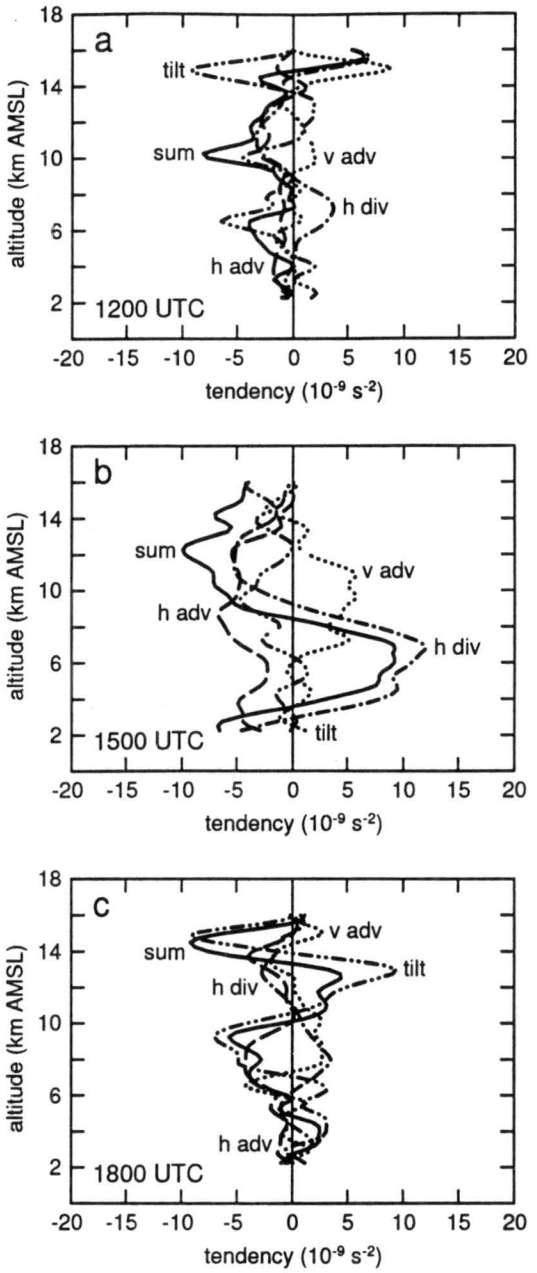

Figure 4.15: Resolved part of the vorticity budget for observed wind. Terms are: horizontal advection (dashed), vertical advection (dotted), divergence (dot-dashed), tilting (dot-dot-dashed), and the sum of terms (solid). Profiles are for a $2° \times 2°$ area centered on the MCV in the middle troposphere, averaged over 3 h ending at the time labeled on 1 August 1996.

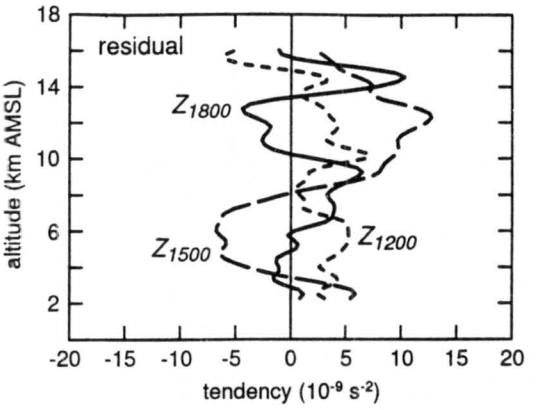

Figure 4.16: Residuals in the vorticity budget for observed wind. Contributions to the vorticity tendency are at 1200 UTC (short dashed), 1500 UTC (long dashed), and 1800 UTC (solid). Profiles are for a 2° × 2° area centered on the MCV in the middle troposphere, averaged over 3 h ending at the time labeled on 1 August 1996.

centered on the maximum vorticity in the MCV, any horizontal advection into or out of that area would necessarily produce a negative tendency. At 1500 UTC, sources represented by the residual acted in concert with vertical advection above the MCV, but at the altitude of the MCV strongly opposed the positive tendency from convergence (fig. 4.16).

Convergence of absolute vorticity between 1200 and 1500 UTC was likely aided by the existent MCV. As explained in section 1.1, when sources of diabatic heating are larger than the Rossby radius of deformation, λ_R, more energy is retained in balanced, vortical flow near an MCS than is transmitted to the far field by gravity waves and buoyancy rolls (Mapes 1993; Schubert et al. 1980). The transition to balanced, vortical flow involves convergence. Background vorticity shrinks λ_R, and the incipient MCV of 1 August 1996 supplied that background vorticity. At 0800 UTC, close to the time when a vortical circulation was first visible in loops of composite reflectivity, λ_R was 276 km, which is close to the 280 km calculated by Chen and Frank (1993) and the 300 km calculated by Cotton et al. (1989) for MCS environments. By 1200 UTC, λ_R had shrunk to 136 km due to the increase in background vorticity. It stayed close to that value through 1500 UTC, the interval of maximum strengthening of the MCV. The radius of maximum wind I estimated for the MCV is

0.75–1.50° latitude (83–167 km). The size of the stratiform region was equally hard to estimate; the major axis was perhaps 350 km long during the asymmetric stage of the MCS, giving a pseudo-radius of 175 km. This is slightly larger than λ_R, so a sizeable fraction of the atmosphere's response to heating was retained near the MCS as convergent, vortical flow in the middle troposphere between 1200 and 1500 UTC.

In the MCS of 1 August 1996, tilting was the primary source of the positive vorticity in the upper troposphere that further deepened the MCV during the final three hours of the period of detailed analysis (fig. 4.15c). Tilting and convergence were the primary sources of vorticity in the lower troposphere. Some of the strength of the MCV in the middle troposphere was maintained by effects represented by the residual and by convergence of absolute vorticity, because convergence, although weakening, continued from 6.5 to 11.0 km AMSL (fig. 4.10c). Three-dimensional advection was generally a sink of vorticity at 6 km AMSL, the altitude of maximum vorticity in the MCV (fig. 4.15c).

A few general properties of the vorticity budget for the total wind deserve mention. In agreement with observations by Chong and Bousquet (1999) and others, tilting and vertical advection of vorticity were roughly anticorrelated about zero (fig. 4.15). Only when this anticorrelation broke down did tilting and vertical advection play large, net roles in the local tendency. The often similar anticorrelation between horizontal advection and divergence of vorticity (e.g., Brandes and Ziegler 1993) was weaker, but still evident at times—in the lower and middle troposphere from 1500 to 1800 UTC, for example (fig. 4.15c). Unresolved effects represented by the residual were just as large as those explicitly resolved in the budget (cf. figs. 4.15 and 4.16), which strongly suggests that regions of persistent convective-scale circulations significantly altered atmospheric vorticity on the mesoscale.

Much of the empirical research into this upscale communication of vorticity in masses of moist convection has focused on large-scale effects of clusters of cumuli in the tropics (e.g., Esbensen et al. 1982; Tollerud and Esbensen 1983; Sui and Yanai 1986). Figure 4.16 generally does not resemble profiles of residuals calculated for such tropical cloud clusters.

Upscale communication of vorticity has also been the subject of numerical studies. For example, in simulations by Montgomery and Enagonio (1998), clusters of cumulonimbi embedded within a vortex were able to strengthen a middle-tropospheric vortex through inward fluxes of angular momentum. The authors used potential vorticity to represent forcing by moist convection. In effect, the existing vortex was cyclonically accelerated because it assimilated positive potential vorticity and expelled negative potential vorticity. Because in their simulations the authors used magnitudes and distributions of potential vorticity that realistically approximated an MCV (radius of maximum wind was 200 km and middle-tropospheric tangential velocity was 5 m s^{-1}) and the moist convection near such a vortex, it is reasonable to assume their results are relevant to MCVs such as that of 1 August 1996.

4.3.2 *Discrimination between synoptic and mesoscale winds*

When terms in the vorticity budget, (2.1), are itemized according to the synoptic background wind and the mesoscale perturbation to that background wind, the budget exemplifies commonly observed—in some cases defining—traits of synoptic and mesoscale motions. First, synoptic and mesoscale horizontal velocities were similarly large, so contributions to vorticity from $\widetilde{\boldsymbol{v}}(\widetilde{u}, \widetilde{v})$ and $\widehat{\boldsymbol{v}}(\widehat{u}, \widehat{v})$ within the budget's terms were similarly large. Second, synoptic vertical velocity, $\widetilde{w}$, was much smaller than mesoscale vertical velocity, $\widehat{w}$, because synoptic divergence, $\nabla \cdot \widetilde{\boldsymbol{v}}$, was much smaller than mesoscale divergence, $\nabla \cdot \widehat{\boldsymbol{v}}$. Accordingly, terms in (2.1) with $\widetilde{w}$ and $\nabla \cdot \widetilde{\boldsymbol{v}}$ contributed very little to the budget. Third, when planetary vorticity, f, is considered part of synoptic vorticity, synoptic and mesoscale vorticities, $\widetilde{\zeta} + f$ and $\widehat{\zeta}$, were of the same magnitude, and in some terms contributed large values to the budget. Gradients in synoptic vorticity were much smaller than gradients in mesoscale vorticity, though. Finally, shear in synoptic and mesoscale winds were similarly large, so tilting of both $\widetilde{\boldsymbol{\eta}}(\widetilde{\xi}, \widetilde{\eta})$ and $\widehat{\boldsymbol{\eta}}(\widehat{\xi}, \widehat{\eta})$ contributed similarly large values to vorticity tendency. The term-by-term analysis of the vorticity budget in the following subsection makes these generalities more meaningful.

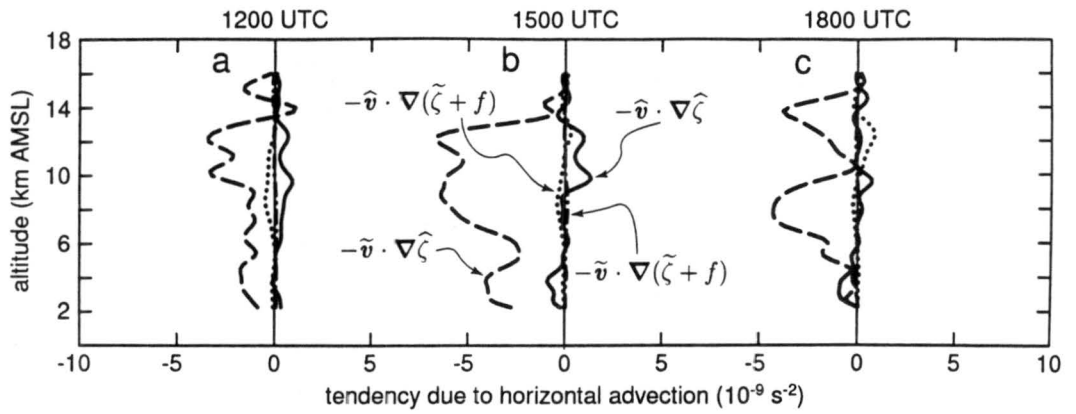

Figure 4.17: Components of horizontal advection in the vorticity budget. Terms are: advection of mesoscale perturbation in vorticity by the mesoscale perturbation in wind (solid) and by the synoptic wind (dashed), and advection of synoptic vorticity by the mesoscale perturbation in wind (dashed-dotted) and by the synoptic wind (dotted). Profiles are for a 2° × 2° area centered on the MCV in the middle troposphere, averaged over 3 h ending at the time labeled on 1 August 1996.

Tendency from horizontal advection

Nearly all the vorticity tendency from horizontal advection was due to advection of mesoscale vorticity by the synoptic wind (fig. 4.17). The reason horizontal advection of mesoscale vorticity by the mesoscale wind was so small is that in the vortical flow of the MCV the gradient of mesoscale vorticity was nearly orthogonal to the mesoscale wind, so the dot product in the horizontal advection term was small even though the two parts of the term were large. Gradients of synoptic vorticity were too small to permit much horizontal advection, even though synoptic vorticity was as large as mesoscale vorticity because I included planetary vorticity in the former.

Because larger vertical shears generally lead to shorter-lived MCVs, differential advection seems to be one mechanism that destroys the vortices (Trier et al. 2000b). Figure 4.17 suggests that such differential advection is mostly by environmental wind, not by wind within the mesoscale circulations of MCSs. Differential advection arose not simply because of the horizontal translation of vertically varying synoptic vorticity, but also because of vertically varying synoptic wind.

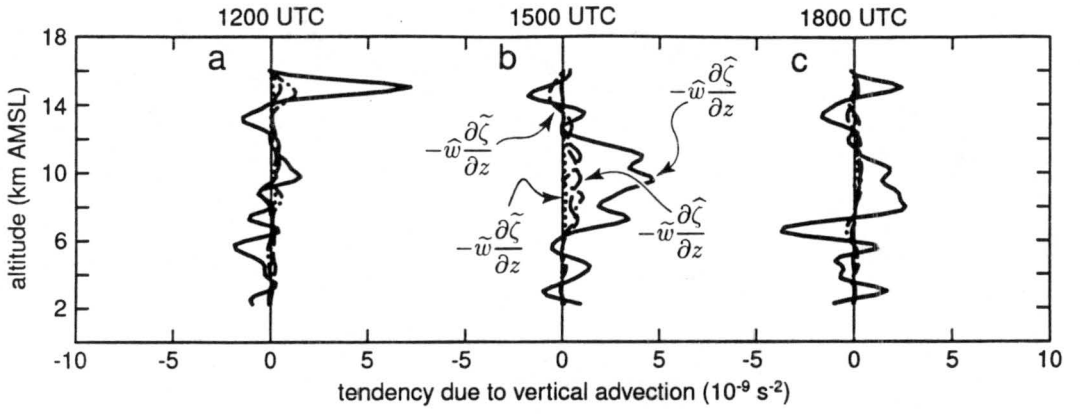

Figure 4.18: Components of vertical advection in the vorticity budget. Terms are: advection of mesoscale perturbation in vorticity by the mesoscale perturbation in wind (solid) and by the synoptic wind (dashed), and advection of synoptic vorticity by the mesoscale perturbation in wind (dashed-dotted) and by the synoptic wind (dotted). Profiles are for a 2° × 2° area centered on the MCV in the middle troposphere, averaged over 3 h ending at the time labeled on 1 August 1996.

Tendency from vertical advection

Nearly all the vorticity tendency from vertical advection was due to advection of mesoscale vorticity by the mesoscale wind (fig. 4.18). Not surprisingly, the only vertical motions strong enough to contribute much to vertical advection were in the mesoscale field. Synoptic vorticity, while large, did not lead to large vertical advection even by the mesoscale wind because vertical gradients of synoptic vorticity were small.

Tendency from divergence

No component in the vorticity tendency from horizontal divergence was negligibly small, although two of the four components were dominant (fig. 4.19). From 1200 to 1500 UTC, when the MCV underwent the greatest deepening and strengthening, vorticity in the MCV was generated mostly, and nearly equally, by convergence of mesoscale vorticity and convergence of synoptic vorticity, both by the mesoscale wind. Tendency due to convergence of synoptic vorticity by the synoptic wind was at least a factor of one-half smaller than the dominant terms, and tendency due

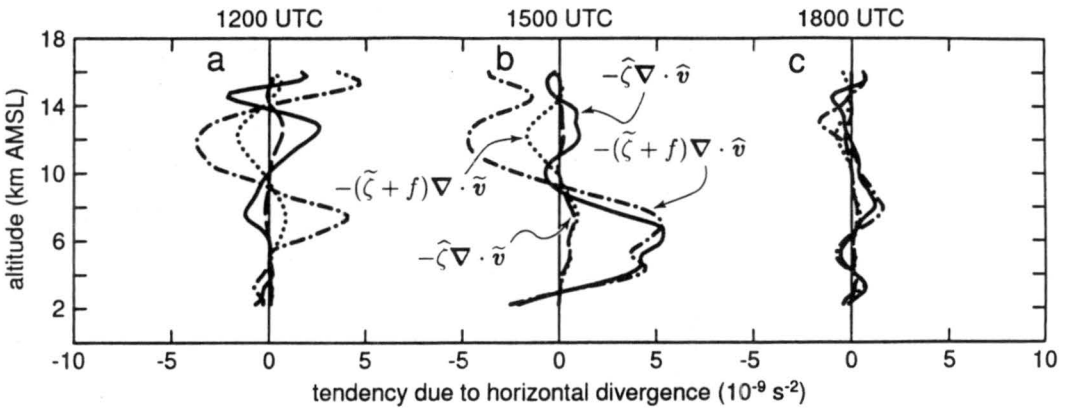

Figure 4.19: Components of horizontal divergence in the vorticity budget. Terms are: divergence of mesoscale perturbation in vorticity by the mesoscale perturbation in wind (solid) and by the synoptic wind (dashed), and divergence of synoptic vorticity by the mesoscale perturbation in wind (dashed-dotted) and by the synoptic wind (dotted). Profiles are for a 2° × 2° area centered on the MCV in the middle troposphere, averaged over 3 h ending at the time labeled on 1 August 1996.

to convergence of mesoscale vorticity by the synoptic wind was slightly smaller yet, especially in the upper troposphere.

It is through convergence that vorticity from short-wave troughs near an MCS would play a role in generating an MCV. The size of a typical short-wave trough would put its vorticity into both the synoptic and mesoscales, as I have approximated them. According to the general conclusions one can draw from figure 4.19, the primary concentrator of vorticity in short-wave troughs must be the mesoscale wind.

Tendency from tilting

Finally, the only two components that contributed appreciably to the vorticity tendency from tilting were tilting of both synoptic and mesoscale vorticity by horizontally varying mesoscale up- and downdrafts (fig. 4.20). Synoptic updrafts were too weak, and their horizontal variations too small, to significantly tilt tubes of horizontal vorticity. Tilted horizontal vorticity consistently contained large synoptic as well as mesoscale components. This differs somewhat from the study by

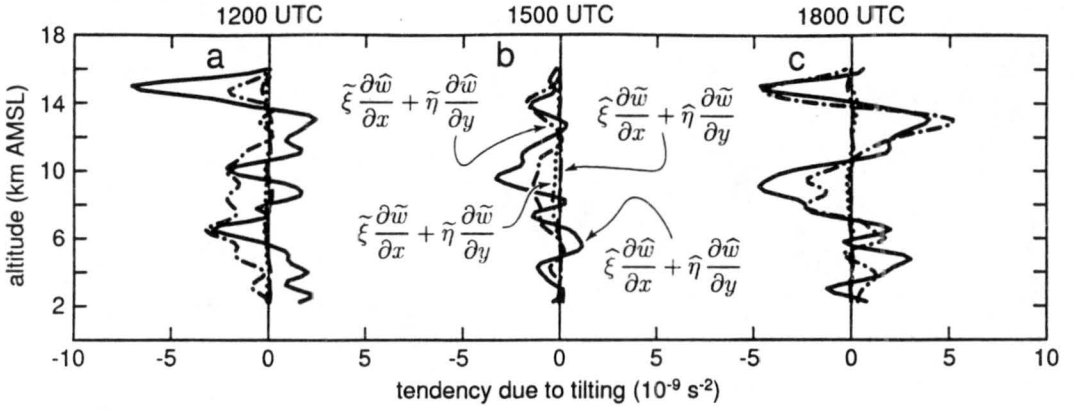

Figure 4.20: Components of tilting in the vorticity budget. Terms are: tilting of vertical shear of the mesoscale perturbation in wind by the horizontal gradient of mesoscale perturbation in vertical motion (solid) and by the horizontal gradient of synoptic vertical motion (dashed), and tilting of vertical shear of the synoptic wind by the horizontal gradient of mesoscale perturbation in vertical motion (dashed-dotted) and by the horizontal gradient of synoptic vertical motion (dotted). Profiles are for a 2° × 2° area centered on the MCV in the middle troposphere, averaged over 3 h ending at the time labeled on 1 August 1996.

Davis and Weisman (1994), in which they found that tilting of environmental shear was dominant early in a simulated MCS, but was later exceeded by tilting of perturbation vorticity.

4.4 Comparison between two forms of vorticity budget

I based the vorticity budget on the conventional form of the vorticity equation, (1.2), for two reasons. First, that form has explicit terms for advection, divergence, and tilting, so one can easily grasp the physical processes represented in each term. Second, the great majority of other budgets of vorticity in observed MCVs have used that form (e.g., Johnson and Bartels 1992; Brandes and Ziegler 1993; Keenan and Rutledge 1993; Scott and Rutledge 1995; Chong and Bousquet 1999; Bousquet and Chong 2000), so it is easy to compare my results with the results of others.

However, as explained in section 2.8, the local tendency from the conventional form is very sensitive to the character of spatial derivatives because it is the sum of four large terms that often nearly cancel one another. To assess this sensitivity in the observations of the MCV of 1 Au-

gust 1996, I calculated a second vorticity budget using the *divergence*, or the *flux* form of the vorticity equation, (2.2–2.4).

The two methods produced grossly similar resolved tendencies, but with noteworthy differences in the details (fig. 4.21). In the lower 65% of the troposphere, below about 8 km AMSL, the two budgets agree well, although the divergence form tended to produce slightly larger tendencies. In the upper troposphere, the divergence form produced significantly larger tendencies. In a few layers, such as between 8 and 11 km AMSL at 1500 UTC (fig. 4.21b), the two budgets even produced opposite signs of the local tendency. Overall, the sign of the vertical derivative of resolved tendency was virtually identical between the budgets, as were the altitudes of local extrema.

There are at least two reasons for the differences between the resolved tendencies from the divergence and conventional forms of the budget. First, the divergence form of the vorticity equation, (2.2–2.4), has fewer terms (and fewer derivatives) than the conventional form, (1.2), so there are fewer calculations. Second, because the divergence form involves a vector with no vertical component, (2.3), an areally-averaged budget may be calculated simply by applying (2.4) at the perimeter of that area. Therefore, the divergence form of the budget is unaffected by small, extreme values of derivatives within the area's perimeter. This is not true of the areally-averaged conventional form of the budget, which involves calculations at each grid point.

Fortunately, the sensitivity of the local vorticity tendency to the form of budget does not call into question the primary conclusions of this chapter. First, the mesoscale and synoptic components of wind contributed significant vorticity to the MCV of 1 August 1996; the former mainly through convergence, vorticity, and three-dimensional wind; the latter mainly through planetary vorticity and horizontal wind. Second, the two largest net, resolved sources of vorticity were convergence and tilting, whose prominence varied during the lifetime of the MCV. Mesoscale convergence of mesoscale and synoptic vorticity produced the single biggest increase in the maturing MCV's strength. Most of the tendency due to tilting was from mesoscale up- and downdrafts acting on horizontal synoptic and mesoscale vorticity.

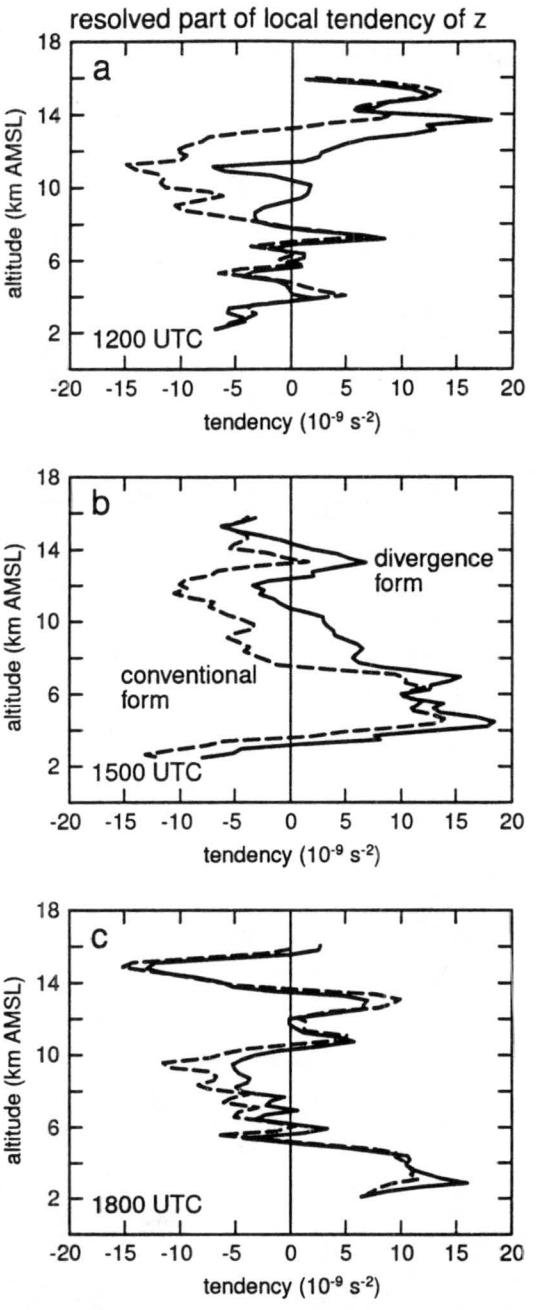

Figure 4.21: Resolved part of the local tendency of relative vorticity calculated according to the conventional (dashed) and divergence (solid) forms of the budget. Profiles are at a) 1200 UTC, b) 1500 UTC, and c) 1800 UTC on 1 August 1996 for a 2° × 2° area centered on the MCV in the middle troposphere; the profiles have not been otherwise averaged or smoothed.

Chapter 5

THERMODYNAMICS

Thermodynamical data for this study are far more coarse than kinematical data, so satisfactorily diagnosing fields of temperature and humidity in four dimensions over the entire period of detailed analysis is impossible. Accordingly, the analysis in this chapter emphasizes what can be gleaned from individual soundings and from a composite MCV intended to circumvent some limitations of the coarse data. Results are consistent with the kinematical analysis in chapter 4.

5.1 Vertical redistribution of mass

Equivalent potential temperature, θ_e, is theoretically conserved in air parcels for many processes, even some that are diabatic. However, in practice, θ_e is not conserved because of ubiquitous processes that are not conservative, such as radiative cooling and heating; because of processes omitted in the usual formulation of θ_e, such as freezing and melting; and because observations simply cannot resolve parcels small enough to be virtually unmixed. Even so, θ_e can be a useful tracer when used with appropriate caution, and it does provide some insight into the MCS and MCV of 1 August 1996.

In order to apply θ_e as a tracer in vertical flows, one must know the horizontal origin of air parcels, because horizontal gradients in θ_e, while not nearly as large as vertical gradients, are sometimes significant. System-relative total wind for this case was generally from the southeast in the lower troposphere, from the northwest in the upper troposphere, and from both the southeast and northwest in the middle troposphere, where convergence and vorticity in the stratiform region were greatest. The closest (spatially and temporally) available soundings west of the MCS, yet not

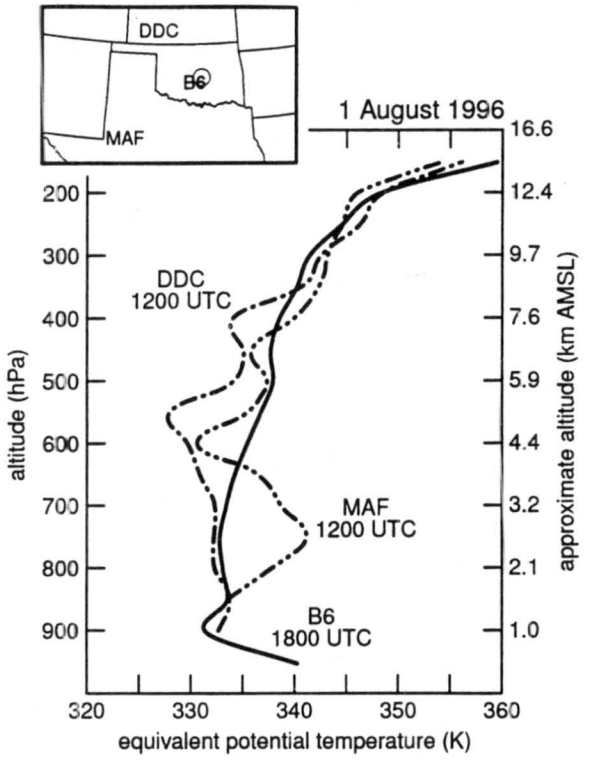

Figure 5.1: Equivalent potential temperature (K) in, and west of, the stratiform region of the MCS on 1 August 1996. Soundings were above Purcell, OK (B6), near the center of the MCV at 1800 UTC (solid), and west of the MCS at Dodge City, KS (DDC; dot-dashed) and Midland, TX (MAF; dot-dot-dashed) at 1200 UTC. The inset map shows the locations of the soundings and the center of the MCV at 1800 UTC (marked by the gray circle). Data are plotted every 50 hPa and smoothed.

recently influenced by it, were above Dodge City, KS (DDC) and Midland, TX (MAF) at 1200 UTC (inset of fig. 5.1). The closest available soundings east of the MCS were above Little Rock and Shreveport at 1200 UTC (inset of fig. 5.2). The intervals of six hours between the sounding above Purcell at 1800 UTC and the operational soundings are unavoidable but not entirely unwelcome because they compensate for some of time it would have taken air to be advected to the MCS from the regions represented by each pair of operational sites.

Profiles of θ_e indicate that the mesoscale downdraft conveyed middle-tropospheric air downward to the lower troposphere. By 1800 UTC, air near 900 hPa in the stratiform region had a θ_e in the low 330s K (fig. 5.1). The only part of the troposphere northwest of the MCS—upstream of

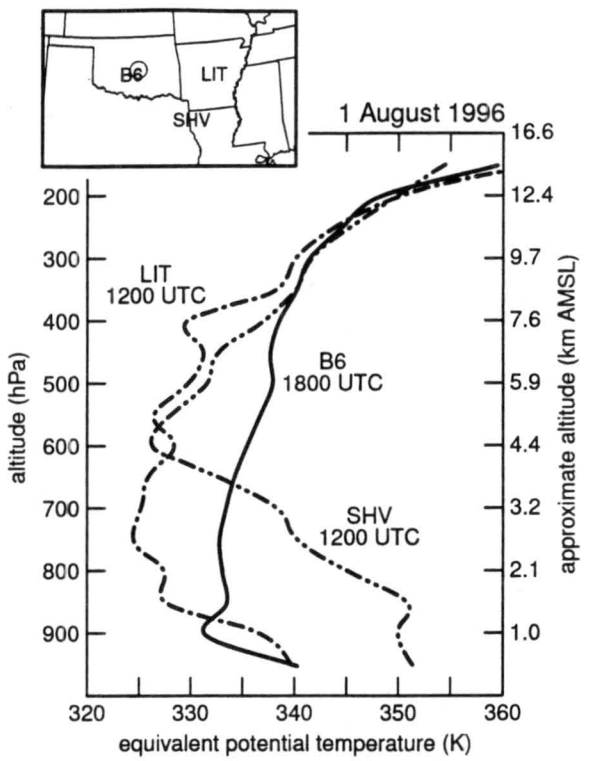

Figure 5.2: Equivalent potential temperature (K) in, and east of, the stratiform region of the MCS on 1 August 1996. Soundings were above Purcell, OK (B6), near the center of the MCV at 1800 UTC (solid), and east of the MCS at Little Rock, AR (LIT; dot-dashed) and Shreveport, LA (SHV; dot-dot-dashed) at 1200 UTC. The inset map shows the locations of the soundings and the center of the MCV at 1800 UTC (marked by the gray circle). Data are plotted every 50 hPa and smoothed.

the mesoscale downdraft—where observed θ_e was consistently that low was between roughly 700 and 500 hPa. Apparently that is where at least some of the air in the lower troposphere, within the terminus of the mesoscale downdraft, originated before descending.

Some lower-tropospheric air within the stratiform region probably also originated in the middle troposphere ahead of the system, judging from the sounding above Little Rock (fig. 5.2). At 700 hPa system-relative flow was from the front of the MCS and θ_e between 800 and 600 hPa was in the middle 320s K. Zipser (1969) explained how middle-tropospheric air ahead of a convective line can flow through gaps between cumulonimbi or can wind up behind a line when new cells form ahead of old cells during the line's propagation. Some of that air then descends and contributes to

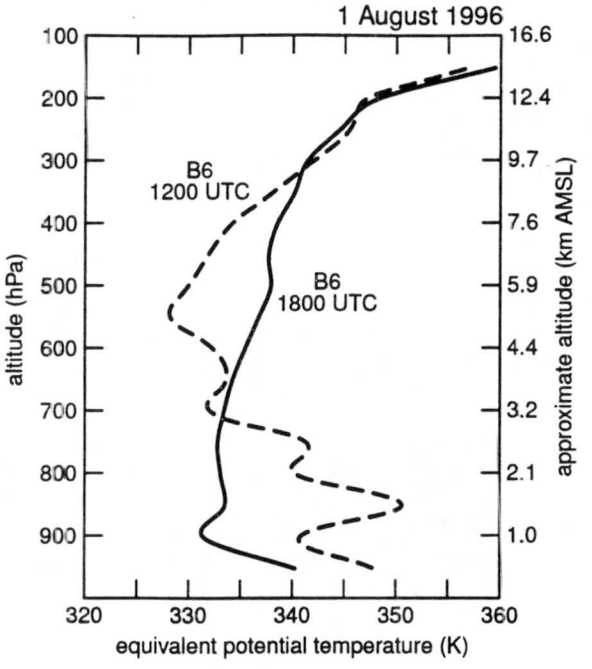

Figure 5.3: Equivalent potential temperature (K) above Purcell, OK (B6) on 1 August 1996. The sounding at 1200 UTC (dashed) was ahead of the MCS. The sounding at 1800 UTC (solid) was very near the center of the MCV. Data are plotted every 50 hPa and smoothed.

a minimum in θ_e in the lower troposphere behind the convective line. Subsequent observations and numerical simulations of MCSs have shown that the lower part of a convective line is, in the mean, a *crossover zone* in which convective flows convey potentially warm, moist, pre-line air upward and convey potentially cool, dry, post-line air downward (e.g., Betts 1976; Zipser 1977; Redelsperger and Lafore 1988). Mixing on small scales in the crossover zone is one example of how the theoretical conservation of θ_e fails in practice when observations are coarse.

Irrespective of mixing, there is no way to use θ_e to unambiguously diagnose the origin of middle-tropospheric air in the stratiform region. At 1800 UTC, in the layer between 600 and 350 hPa above Purcell, θ_e ranged from 335 to 340 K. This range of values was common to multiple layers of the troposphere both ahead of and behind the MCS (figs. 5.1 and 5.2).

Upper-tropospheric air in the stratiform region may have been a combination of air injected

from the lower troposphere and air that remained in the upper troposphere during the passage of the MCS. The sounding above Shreveport at 1200 UTC (fig. 5.2) shows that θ_e below 850 hPa exceeded 350 K. Such values are large enough to be consistent with substantial upward transport across almost the entire troposphere to just below the tropopause.

The overall effect of the convective and mesoscale drafts in the MCS of 1 August 1996 was partially to homogenize the troposphere in the vertical. At Purcell, before the passage of the MCS, temperature and humidity at 1200 UTC were vertically distributed in a way that gave the profile of θ_e the shape of a C, with a minimum in the layer between 600 and 500 hPa, and maxima in the lower and upper troposphere (fig. 5.3), which is common in pre-MCS environments (e.g., Fovell and Ogura 1988; Houze 1993). Six hours later, as the stratiform region of the MCS passed by, the sonde launched from Purcell recorded a much more vertically mixed profile of θ_e. Nearly all the layers of potential instability were removed from above 900 hPa. In particular, little remained of the general potential instability between 850 and 550 hPa at 1200 UTC. We must be mindful that the lapse rate of θ_e does not indicate the presence or absence of buoyant instability (sometimes called gravitational instability) itself. It indicates *near instability*, as Sherwood (2000) called it; that is, the potential that a layer of the troposphere might become buoyantly unstable if the basic state of that layer were changed by some pre-conditioning process, such as widespread mechanical lifting.

5.2 Profiles of temperature and dewpoint in the stratiform region

The memorable term *onion sounding* (Zipser 1977) is commonly applied to profiles of temperature and dewpoint that characterize the soundings within stratiform regions of many MCSs, especially MCSs that contain strong, descending rear inflow. In an onion sounding, a layer of highly subsaturated air in the lower troposphere separates a shallow, cool, nearly saturated layer near the ground from a deep, nearly saturated, statically neutral layer in the middle and upper troposphere (see Zipser's paper for examples). The few soundings through the stratiform region of the MCS of 1 August 1996 display many characteristics of the archetypal onion sounding (figs. 5.4–5.6).

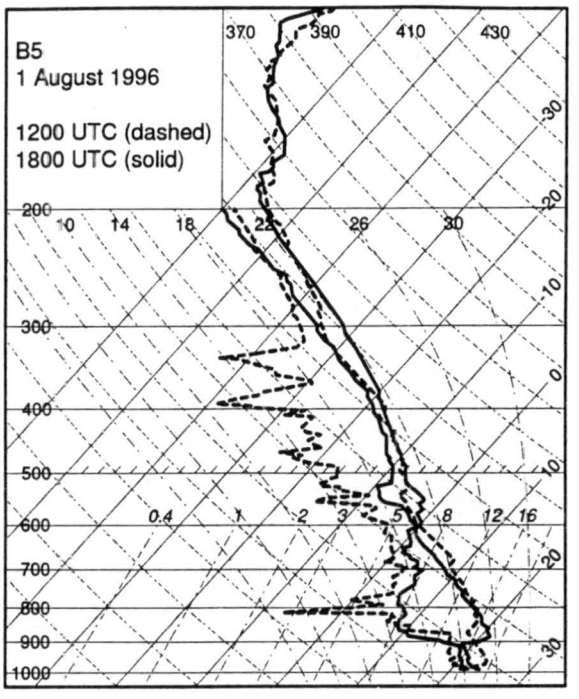

Figure 5.4: Soundings above Morris, OK (B5) plotted on a skew-T/ln-p diagram. Traces are dewpoint (left pair of lines) and temperature (right pair of lines) at 1200 UTC (dashed) and 1800 UTC (solid) on 1 August 1996.

5.2.1 Conditions beneath the anvil

Descending air beneath the base of the trailing anvil of the MCS was highly subsaturated (fig. 5.6). This was true even where the Oklahoma Mesonet indicates rain fell through the dry, descending air and reached the ground beneath the enhanced stratiform region.

The large dewpoint depression (the difference between temperature, T, and dewpoint, T_d) in the lower part of this and other mesoscale downdrafts can be viewed, after some simplifying assumptions, as the result of two competing rate problems, one regulating dewpoint, the other regulating temperature (Leary 1980). Each rate problem comprises the same two opposing processes: advection and evaporation. For temperature, downward advection of potentially warmer air (quantified by potential temperature, θ) increases temperature while evaporative cooling from rain decreases temperature. For dewpoint, downward advection of generally lower absolute humidity (quantified

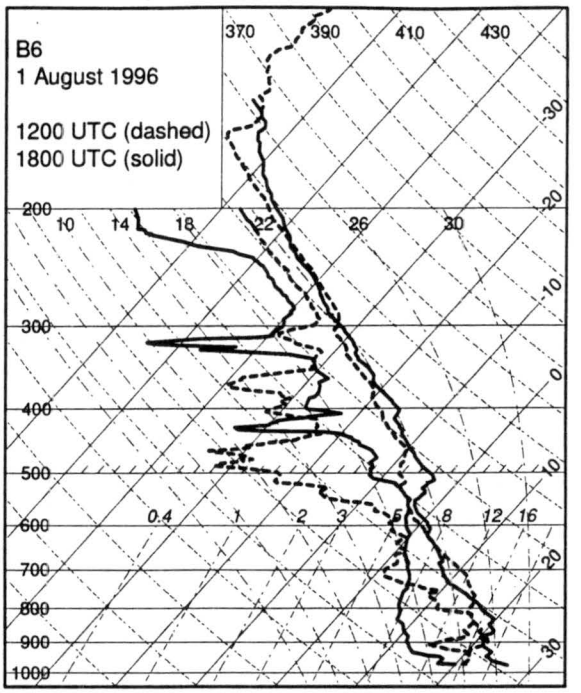

Figure 5.5: Soundings above Purcell, OK plotted on a skew-T/ln-p diagram. Traces are dewpoint (left pair of lines) and temperature (right pair of lines) at 1200 UTC (dashed) and 1800 UTC (solid) on 1 August 1996.

by vapor mixing ratio, q_v) decreases dewpoint while evaporation of rain increases dewpoint.

In this way, the lapse rates of temperature and dewpoint in figure 5.6 are indirect measures of the comparative strengths of advection and evaporation. Downward advection of well mixed air without any evaporation would produce a trace of temperature along a line of constant potential temperature (a dry adiabat) and a trace of dewpoint along a line of constant mixing ratio. Downward advection of well mixed air with unlimited evaporation would produce traces of dewpoint and temperature along a line of constant equivalent potential temperature (a moist adiabat). Therefore, the extent to which traces of temperature and dewpoint approach these two limits is some indication of the comparative strengths of advection and evaporation. Above Vici, OK (B4) at 1200 UTC, the moderate dewpoint depression, conditionally unstable lapse rate in temperature, and moderate lapse rate in dewpoint are evidence that neither downward advection nor evaporation were entirely

dominant. Above Purcell at 1500 UTC there is evidence of a layer of very high evaporation and a layer of very low evaporation within the downdraft. The former was between 750 to 710 hPa, where traces of temperature and dewpoint in figure 5.6b are very nearly along moist adiabats, although the dewpoint depression in that layer was still 2 or 3 K. The latter was between 870 and 750 hPa where the lapse rates of temperature and dewpoint were respectively along $\theta = 308$ K and $q_v = 9$ g kg^{-1}, a sign of overwhelming downward advection in the draft—stronger downward advection than that above Vici at 1200 UTC. The relative downdraft strengths deduced from figure 5.6 are consistent with figure 4.10a and b, to the extent that temporally and spatially averaged data can represent circulations over specific observing sites.

Strong, subsaturated mesoscale downdrafts often sharply decrease pressure at the ground beneath them, generating *wake lows* beneath stratiform regions (e.g., Williams 1963; Johnson and Hamilton 1988; Johnson et al. 1989; Yang and Houze 1995). Inertia can convey descending air past its level of neutral buoyancy, at which point the air is virtually warmer and less dense than its surroundings. Provided air does not correspondingly cool somewhere above the warmed part of a downdraft, pressure at the ground will fall hydrostatically. The sounding shown in figure 5.6b is exactly the sort that often signifies a wake low at the ground immediately beneath the sounded column (e.g., Johnson et al. 1989). However, in this case it did not. At 1500 UTC the only wake low the Oklahoma Mesonet detected was at the northern border of the state, just north of the hammer head in the reflectivity of the stratiform region (fig. 5.7). (It is not clear to what extent the MCV may have contributed to this low in the north, although the low was more than 100 km north of the middle-tropospheric location of the vortex.) The reason the strong downdraft evinced in figure 5.6b did not generate a wake low is because not all of the highly subsaturated air in the draft's terminus was warmed. Above 800 km AMSL it was cooled (compare the dotted and solid lines in the figure). Apparently the increase in density within the cooled layer was enough to counter the decrease in density within the warmed layer. Despite the sounding shown in figure 5.6a, there was no wake low near Vici at 1200 UTC, either.

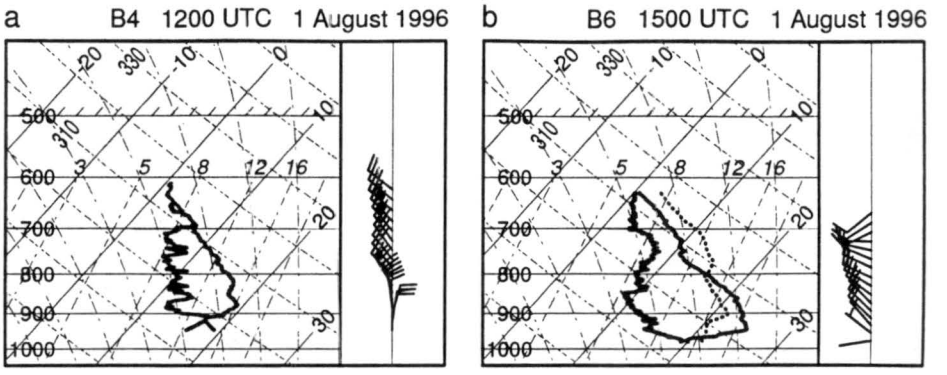

Figure 5.6: Temperature and dewpoint beneath the trailing anvil of the MCS on 1 August 1996. Profiles are plotted on a skew-T/log-p diagram. The soundings were above a) Vici, OK (B4) at 1200 UTC and b) Purcell, OK (B6) at 1200 UTC (dotted) and 1500 UTC (solid). Half and full wind barbs respectively represent 5 and 10 m s^{-1}. Both sondes stopped transmitting data at approximately the altitudes of 0°C.

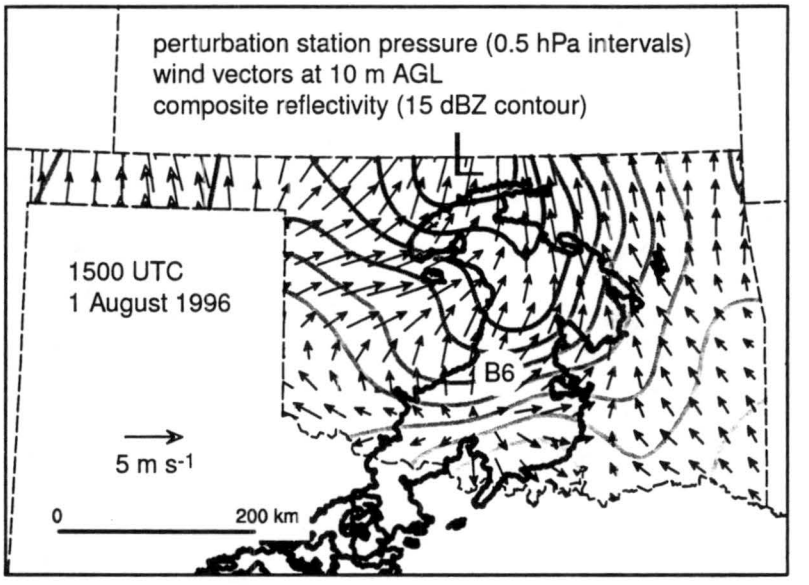

Figure 5.7: Radar reflectivity and surface conditions within the Oklahoma Mesonet at 1500 UTC on 1 August 1996. Surface pressure is contoured every 0.5 hPa in gray; values are deviations from a state-wide mean and darker grays indicate lower pressure. Vectors depict wind at 10 m AGL. The thick black contours outline reflectivity $\geq$ 15 dBZ. The GCIP site at Purcell, OK is marked by "B6."

5.2.2 *Double-onion soundings*

The 1800 UTC sounding above Morris (fig. 5.4), which was near the perimeter of the MCV, displays well the characteristic shape of the typical onion sounding, with one exception: just above the altitude of 0°C was a relatively warm, dry layer (something similar appears in fig. 5.5, as well). This feature between 600 and 520 hPa looks like a small version of the dry layer between 900 and 600 hPa in figure 5.4 and between 970 and 550 hPa in figure 5.5.

These *double-onion soundings*, as some call them, have appeared in other studies (e.g., Brandes 1990; Bartels and Maddox 1991; Stumpf et al. 1991; Johnson et al. 1996; Mapes and Zuidema 1996), but there seems to be no universal explanation for them. Because of limitations of the available data, I can only speculate about which existent or new explanations might apply in this case.

The simplest and most obvious explanation to first test is that what produced the lower-tropospheric dry layers in figures 5.4, 5.5, and 5.6 also produced the middle-tropospheric dry layer in figure 5.4: strongly descending air. Mesoscale data give no indication of this origin, however. Indeed, the mesoscale downdraft tended to be weak, not strong, at the altitude of the upper onion (fig. 4.11b and c and other profiles not shown). Smaller, unresolved downdrafts may have been partly responsible, but this cannot be determined with the available data.

The proximity of the upper onion to the altitude of 0°C suggests that melting may have played a role in producing the relatively warm, dry layer. Melting in a stratiform region cools a layer of air over a large horizontal area (that cooling is apparent immediately below 600 hPa in figure 5.4). The resultant horizontal pressure field accelerates divergent flow below the cooled layer and convergent flow above (Mapes and Houze 1995). Perhaps such convergent flow above the cooled layer was able to advect into the stratiform region comparatively dry air from outside the MCS, which longwave radiation would then have heated (Mapes and Zuidema 1996). GCIP soundings at 1800 UTC do reveal beyond the MCS a dry environment in which the vapor mixing ratio was generally less than 2 g kg^{-1} between 600 and 500 hPa (not shown). In addition, from 1200 to 1500 UTC, when pronounced bright bands in radar reflectivity indicated vigorous melting in the stratiform region, there was a localized maximum of convergence near the altitude of 0°C

(fig. 4.10b), which is consistent with *melting convergence*, as Mapes and Houze (1995) called it. However, that convergence was not above, but roughly at, the altitude of 0°C (although the altitude of 0°C was probably slightly lower in some parts of the MCS than others, particularly in heavy precipitation). Plus, there was no corresponding layer of locally maximized divergence detectable just below that altitude (fig. 4.10b). Even if convergence did introduce, above the melting level, a layer of dry air into the decaying stratiform region, it is not clear why that layer would have been shallow enough to account for the small upper onion when convergence (produced by phenomena other than melting) extended many kilometers above the melting level, and environmental air was quite dry through that entire depth. In addition, judging from the simulations of Mapes and Zuidema (1996), the net long-wave heating within the dry layer would have been far too weak to generate the amount of warmth between 600 and 500 hPa (the upper onion) shown in figure 5.4.

One case in which a double-onion sounding was not only observed but explained was that documented by Stumpf et al. (1991). It turned out that the two dry layers depicted in the traces of temperature and dewpoint within the stratiform region of the MCS they studied were not two different circulations, but the same circulation penetrated in two different locations by the ascending sonde. The upper dry layer was the part of the system-relative inflow that was directed toward the front of the MCS in the middle troposphere. The lower dry layer was the part of the same system-relative inflow after it had overturned and was moving toward the back of the MCS in the lower troposphere. In the case of the MCS of 1 August 1996, the 1800 UTC sounding above Morris was taken in a part of the MCS where system-relative flow was from the southeast at, and between, the altitudes of both dry layers, so the explanation of Stumpf et al. (1991) cannot be applied here.

5.3 Heating in the MCV

To a first approximation, the MCV contained warmed air above the altitude of 0°C in the environment and cooled air below (fig. 5.8). Magnitudes of the changes in virtual potential temperature were as large as 5 K in some middle- and upper-tropospheric layers within the MCV, but average magnitudes were closer to 2 K.

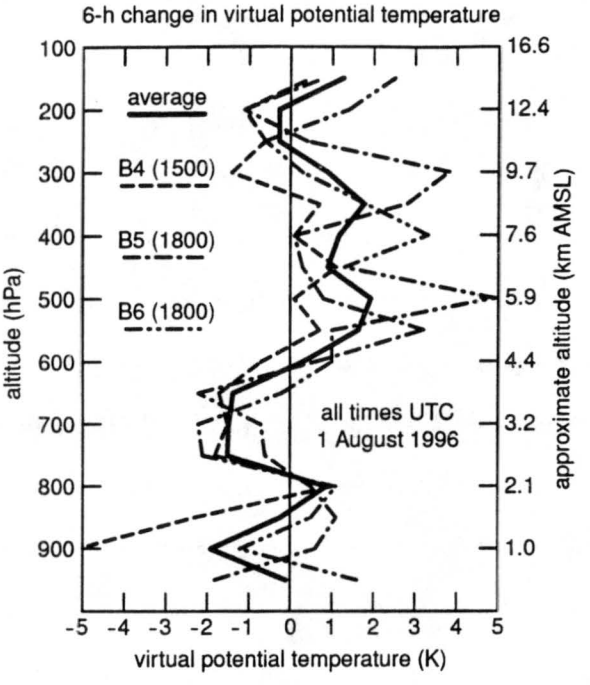

Figure 5.8: Changes in virtual potential temperature (K) within the MCV over 6 h. Profiles are from soundings above Vici, OK (B4; dashed), Morris, OK (B5; dash-dotted), and Purcell, OK (B6; dash-dot-dotted). The thick solid line shows the average profile. The 6-h intervals end at the times shown. The first of each sounding pair used to calculate the difference was taken ahead of the MCS and MCV; the second of each was taken within the MCV. Data are plotted every 50 hPa.

The gross shape of perturbation potential temperature shown in figure 5.8—that of a single, sinusoidal wave—is the same as the gross shape of diabatic heating profiles in the stratiform regions of MCSs (e.g., Houze 1982; Johnson and Young 1983; Houze et al. 1989; Gallus and Johnson 1991). Thus, it is likely that heating in the upper part of the troposphere on 1 August resulted from condensation, freezing, and deposition in the mesoscale updraft of the MCS. Cooling in the lower part of the troposphere likely resulted from melting and evaporation beneath the anvil of the stratiform region. Of course, most heating and cooling does not translate identically to local increases and decreases in temperature. Expansion of rising air and compression of sinking air nearly cancel diabatic heating. The part of diabatic heating that is not canceled produces profiles such as the one shown in figure 5.8. Such rising and sinking occurs in mesoscale and convective

drafts. It also occurs in the vertical circulations within gravity waves. Diabatic heating in MCSs and other modes of moist convection triggers gravity waves that lower and adiabatically cool layers of the troposphere as they pass and disperse; the opposite occurs for cooled columns (Nicholls et al. 1991; Mapes 1993; Haertel and Johnson 1998).

Short- and longwave radiation in and near the deep convective towers and anvils of MCSs also contribute to such profiles. Using a multiple-scattering radiative transfer model, Webster and Stephens (1980) simulated how a cloud with a base at 600 hPa and a top at 200 hPa radiatively warms surrounding air as much as 5–10 K day^{-1} through roughly the lowest three-fourths of its depth. From maturity through the first few hours of its decay, the MCS of 1 August 1996 included behind its convective line a cloud of roughly the vertical extent simulated by Webster and Stephens (1980). Therefore, net short- and longwave heating could account for a substantial part of the increase in virtual potential temperature above 600 hPa, as shown in figure 5.8. The role of radiation in such profiles is easy to overlook.

Superposed on the grossly sinusoidal wave in figure 5.8 are a number of perturbations over shallow layers of the troposphere. Although not deep, the perturbations seem to have been horizontally coherent because each appears in multiple soundings through different parts of the MCV. The perturbations in the lower and middle troposphere call to mind the *melting-layer reverberations* of Mapes and Houze (1995), although the warmed and cooled layers in their figures are thinner and higher than the layers depicted in figure 5.8.

First, embedded within the generally cooled air of the lower troposphere was a thin warmed layer centered at 800 hPa. At this altitude the mesoscale downdraft was decelerating (figs. 4.10b and 4.11b), probably because it was lower than its level of neutral buoyancy. Near the terminus of the downdraft, adiabatic compression heated the air more than evaporation cooled it. Shallow, warmed layers in the lower troposphere like this one are common in MCSs (e.g., Gamache and Houze 1985; Johnson and Bartels 1992).

Second, just below the warmed layer was cool outflow from cumulonimbi (fig. 5.8). This *surface cold pool*, as it is often called, had spread rearward from the convective line where it orig-

inated in convective downdrafts. That origin makes surface cold pools distinct from deeper layers of cool air produced higher in the troposphere by stratiform regions. At Purcell, sunshine through breaks in the clouds of the decaying stratiform region had warmed the ground beneath the cold pool by 1800 UTC, which explains the comparatively high virtual potential temperature just above the ground at that site (fig. 5.8). There is little doubt that, without strong sunshine prior to 1800 UTC, the base of the differential profile for Purcell would have been similar to the bases of the other two profiles.

Third, between 400 and 500 hPa was a local minimum in virtual potential temperature, although it was still positive. The limitations in thermodynamical data for this study make it impossible to prove the origin of the minimum, but there is at least one explanation consistent with the evidence. The minimum in warming was roughly at the same altitude as the base of the mesoscale updraft (cf. figs. 4.10 and 5.8). If subsaturated environmental air was part of the convergent flow into the updraft, some air would have cooled adiabatically during dry ascent—that is, the air's virtual potential temperature would not have changed—until reaching its dewpoint (Rosenthal 1980; Gamache and Houze 1985). Any such dry, adiabatic ascent would have partially diluted the overall warming in that layer of the mesoscale updraft. Not every sounding in the stratiform region supports this speculation, but some do. At 1800 UTC, the 400–500 hPa layer above Morris was nearly saturated, so ascent there would have increased virtual potential temperature (fig. 5.4). However, above Purcell at 1800 UTC, the 400–500 hPa layer was much drier (fig. 5.5). Vici's sounding at 1500 UTC, also through the stratiform region, displays a similar dry layer (not shown).

Finally, in the upper troposphere was a shallow cooled layer. Some of the decrease in virtual potential temperature of the cooled layer can be explained by net radiational cooling in the top part of the stratiform anvil (Webster and Stephens 1980; Houze 1982; Wong et al. 1993). (Figure 4.4 shows a schematic depiction of the anvil at ~1230 UTC.) Although the high sun around local noon increases shortwave radiation into the tops of stratiform clouds, thereby partially, or even fully, canceling long-wave cooling (Wong et al. 1993), by local noon on 1 August little was left of the MCS's trailing anvil.

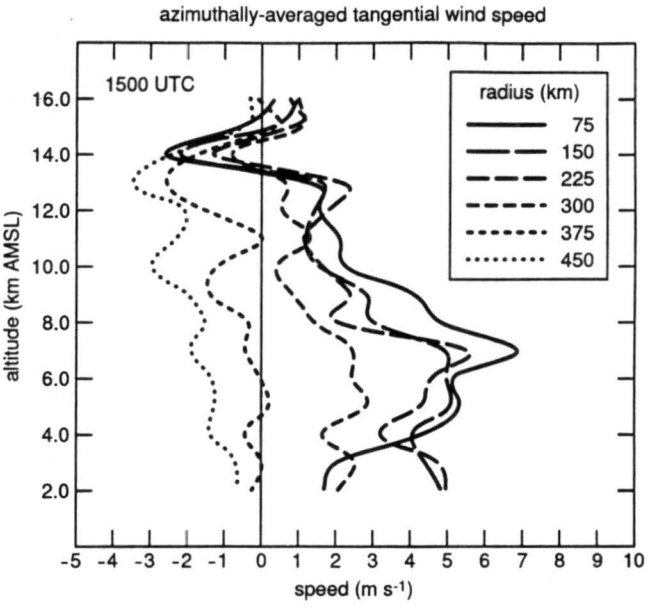

Figure 5.9: Azimuthally-averaged tangential wind speed (m s^{-1}) within the MCV at 1500 UTC on 1 August 1996. Radii are from 75 to 450 km at intervals of 75 km; the key indicates the lines for each radius. Data are plotted every kilometer and smoothed.

5.4 Gradient imbalance in the MCV

The MCV of 1 August 1996 was apparently not in gradient balance. However, this result should be interpreted with slight caution because of assumptions and compromises involved in the assessment of balance. (In this section, *balance* and *imbalance* refer only to *gradient and hydrostatic balances.* The methods and data behind the following results are explained in section 2.13.)

In a balanced vortex, the strongest tangential winds are at the same altitude as the top of the cool layer—or, alternatively, the bottom of the warm layer—in the vortex's core (Bartels and Maddox 1991; Bartels et al. 1997). If the MCV of 1 August 1996 were balanced, based on the tangential wind at 1500 UTC (fig. 5.9) the top of the cool layer would have been at about 7 km AMSL. Instead, it was about 2 km lower (fig. 5.10). Apart from that discrepancy, the observed temperature profile in the MCV at 1800 UTC displays the same gross features as the balanced profile: a negative perturbation surmounted by a positive perturbation.

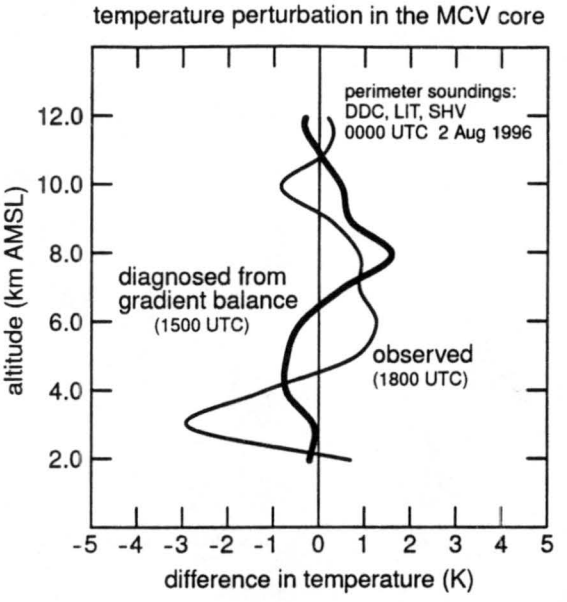

Figure 5.10: Balanced and observed temperature perturbations within the MCV. Both perturbations (K) are with respect to a far-field profile approximated with soundings above Dodge City, KS (DDC), Little Rock, AR (LIT), and Shreveport, LA (SHV) at 0000 UTC on 2 August 1996. The thin line is the observed profile from near the MCV's core above Purcell, OK (B6) at 1800 UTC on 1 August. The thick line is a retrieved profile in gradient balance with the MCV's wind field at 1500 UTC. Data are plotted every kilometer and smoothed.

The most pedestrian explanation for the apparent gradient imbalance in the MCV of 1 August 1996 is that the necessarily imperfect method of creating figure 5.10 (sec. 2.13) misrepresented the actual fields of mass and wind in and near the vortex. In particular, if the MCV were highly tilted, then the single sounding at 1800 UTC may not have accurately observed the true depth and strength of the cool layer. However, too much other evidence corroborates figure 5.10 to make this a likely explanation. Signs of the anomalously shallow, lower-tropospheric cool layer also appear in figure 5.8, whose plots of 6-h temperature changes indicate that as the MCV passed over three different GCIP sites, the local decrease in virtual potential temperature extended to only about 4.4 km AMSL at all three. This altitude agrees almost exactly with the transition altitude shown in figure 5.10, which is evidence that both the core profile and the far-field profile used to construct figure 5.10 are respectively representative of the MCV and its environment, and that any tilt

to the MCV does not invalidate figure 5.10. In addition, the observed transition from cool to warm core was very near the altitude of 0° in the environment (fig. 4.10), which is typical of temperature changes due to non-radiative cooling and heating within stratiform anvils (e.g., Houze 1982; Johnson and Young 1983). Finally, tangential wind at 1500 UTC, from which the balanced temperature profile was retrieved, appears consistent with observations of wind at other individual hours (those depicted in the average derivative fields in figure 4.10b and c, for example).

One reason the MCV of 1 August 1996 may have been imbalanced is that it was being strongly forced during most of the period of detailed analysis. Possibly the MCV simply did not have time to achieve balance before it left the densest part of the NPN, because raining clouds in the MCS's dissipating stratiform region continued strongly to heat the troposphere through 1500 UTC (fig. 3.4). In the few hours following 1500 UTC, the areal extent of the stratiform region markedly decreased (fig. 3.4h), and by 1700 UTC, strong convergence into the MCV had stopped (fig. 4.11b). A natural assumption is that, in the absence of strong forcing after 1700 UTC, the MCV may have been evolving toward balance, but not quickly enough for a balanced core temperature profile to appear by 1800 UTC, when the sounding was taken above Purcell. Without forcing, an MCV should adjust toward balance in roughly f^{-1} (C. Davis, personal communication, 2001), which would have been about 3.3 h for the MCV of 1 August 1996. The hypothesis that the MCV did not have time to achieve balance may be valid, but not all the evidence supports it. While approaching balance, the greatest tangential wind speeds (and vorticity due to curvature) would have descended to the top of the cool layer. Instead, they ascended. From 1200 to 1500 UTC, the average altitude of maximum vorticity was just below 6.0 km AMSL (fig. 4.10b). By 1700 UTC its altitude was between 6.0 and 7.0 km AMSL (fig. 4.11b). Vorticity below 4.5 km AMSL did increase over that time, however, which may have been a response to cooling in the lower troposphere.

It is not easy to judge figure 5.10 in the context of previous research because, heretofore, no published empirical study of which I am aware has included an explicit examination of gradient balance in an MCV, although Bartels and Maddox (1991) did present strong circumstantial evidence of an MCV in approximate gradient balance. They found that the MCV of 14 May 1984 had a

cooled core whose top was nearly at the same altitude as the MCV's largest tangential wind speeds. Some MCVs that others have studied appear more like the MCV of 1 August 1996, with maximum tangential wind speeds (or vorticity) at significantly higher altitudes than the observed tops of the cool layers, or what can be reasonably inferred to be the tops of the cool layers, in the vortices' cores (e.g., Brandes 1990; Chong and Bousquet 1999).

Bartels et al. (1997) *assumed* balance for some of their treatment of the MCV of 9 June 1988. Their assumption seems incompatible with their data. Tops of cool layers in the stratiform regions of MCVs tend to be very near the altitude of 0° (e.g., Houze 1982; Johnson and Young 1983). That altitude was at 590 hPa, or approximately 4.5–4.6 km AMSL, in the environment of the MCS of 9 June 1988, yet Bartels et al. diagnosed from the observed wind field a cool-layer top of 6.3 km AMSL in order to model their MCV's potential vorticity perturbation. It is more likely that their MCV had a cool layer too shallow to be in gradient balance.

5.5 Other applicable forms of balance

In a general sense, a vortex is balanced if its mass and wind fields are diagnostically related. Gradient balance is the simplest form of balance applicable to vortices of the size and altitude of MCVs, so a test for gradient balance is a fitting starting point in the examination of mass and wind in an MCV. However, there are other, more complex forms of balance that are also applicable. An MCV that is not in gradient balance may still be balanced according to one of those forms.

Nonlinear balance, in particular, has proven quite fruitful in both diagnostic and prognostic simulations of MCVs (e.g., Raymond and Jiang 1990; Davis and Weisman 1994; Davis et al. 1996; Olsson and Cotton 1997). It is based on the assumption that the nondivergent component of wind is much larger than the irrotational component. Mass and wind are related by a balance equation that is derived from the divergence equation in a manner whereby terms involving irrotational and vertical velocity are neglected.

Trier and Davis (2002) used the nonlinear balance constraint in order to invert potential vorticity calculated from gridded analyses of the Rapid Update Cycle (RUC). Their goal was to diag-

nose the balanced vertical velocity and parcel displacements in an MCV that fostered serial MCSs. They found that balanced motions contributed to roughly half of the total vertical displacement of unstable air upstream of deep moist convection in the MCSs.

Just how similar the distribution of mass in an observed MCV must be to that in an idealized, perfectly balanced vortex before former may be called *balanced* is highly debatable. The vertical velocity in the MCV studied by Trier and Davis (2002) was qualitatively quite similar to the purely balanced vertical velocity, yet, if half of the vertical displacement of parcels in the vortex was unbalanced, was the MCV balanced? As mentioned above, the distribution of mass in the MCV of 1 August 1996 was grossly similar to that in the balanced vortex I diagnosed, but the differences between the two were significant.

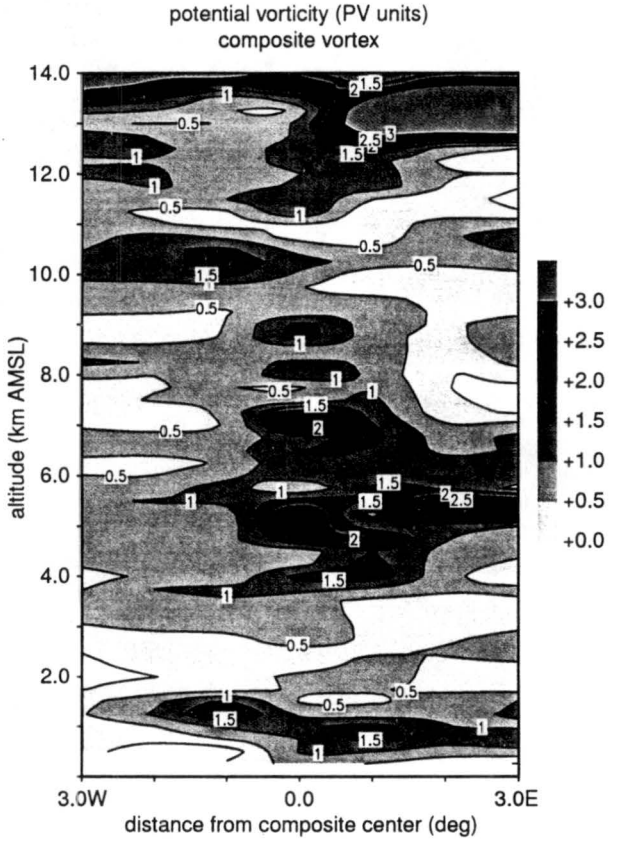

Figure 5.11: Potential vorticity within the composite MCV. Contours and shading are every 0.5×10^{-7} m^2 s^{-1} K kg^{-1}. Horizontal distance is from the center of the composite vortex.

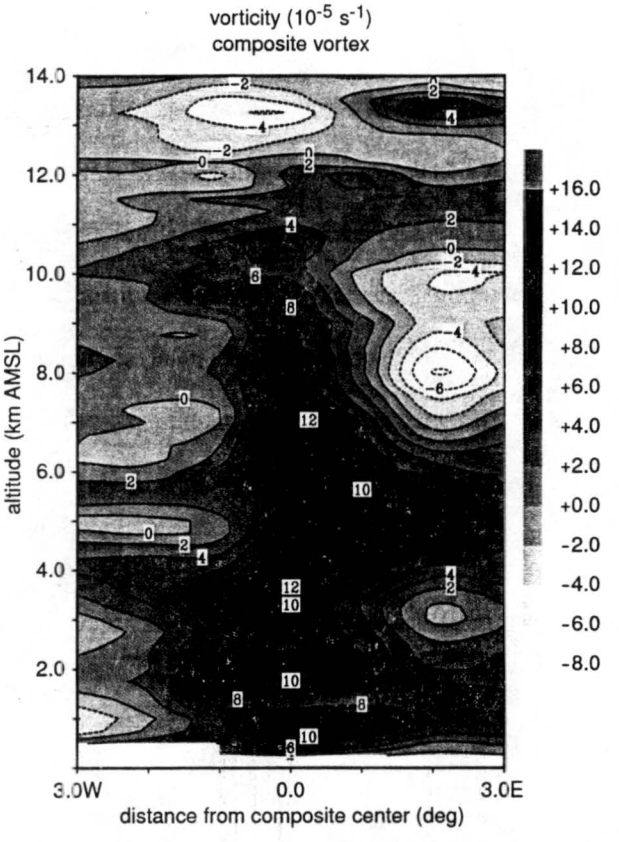

Figure 5.12: Relative vorticity within the composite MCV. Contours and shading are every 2×10^{-5} s^{-1}.

5.6 Potential vorticity in the composite MCV

Potential vorticity, defined by (2.5), was greatest in the middle troposphere within the column of the composite MCV (fig. 5.11). This maximum is broadly consistent with what one would expect in a vortex generated by vertical gradients of diabatic heating within the active stratiform region of an MCS (Raymond and Jiang 1990; Hertenstein and Schubert 1991; Fritsch et al. 1994). However, the upper troposphere is missing the expected minimum in potential vorticity. Apparently, the column of high relative vorticity within the composite MCV (fig. 5.12) was tall enough to mask the weak, but existent, minimum in the lapse rates of potential temperature between 9.0 and 11.25 km AMSL (fig. 5.13). It is this minimum in lapse rate that is partly responsible for the

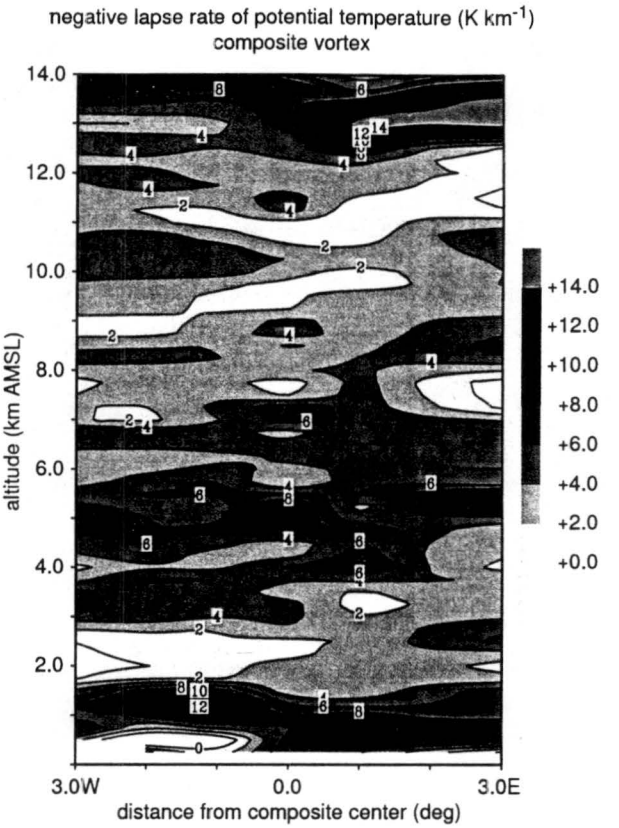

Figure 5.13: Negative lapse rate of potential temperature within the composite MCV. Contours and shading are every 2 K km^{-1}.

minimum in potential vorticity above many simulated MCVs.

Within the core of the composite MCV, the overall maximum in potential vorticity is between 3.75 and 7.5 km AMSL (fig. 5.11). Within this overall maximum are two localized maxima at roughly 5.0 and 7.25 km AMSL. The overall maximum reflects the structure of relative vorticity in the composite (fig. 5.12), which is duly similar to the 3-h averages in relative vorticity centered on the actual (not the composite) MCV (fig. 4.10). The localized maxima are due to increases in the lapse rate of potential temperature at the bases of shallow warm layers (fig. 5.13), which appear in the actual MCV. The lower of the two maxima coincides with the top onion of the double-onion soundings shown in figures 5.4 and 5.5, and discussed in subsection 5.2.2. The upper of the two

maxima comes from a less distinct and less widespread warm layer near 400 hPa, which is apparent only in some soundings, such as the one shown in figure 5.5.

Outside the core of the composite MCV are other extrema in potential vorticity in the middle and upper troposphere, including one exceptionally prominent maximum at 5.5 km AMSL about 2.5° east of the composite's center. An anomalously high lapse rate in potential temperature is responsible (fig. 5.13). The anomaly's origin is unknown, although because it is along the eastern edge of the composite, spurious data from inside or near the MCS's leading convective line are probably responsible.

The shallow, but horizontally expansive band of high potential vorticity below 1.75 km AMSL (fig. 5.11) is due in large part to subsaturated downdrafts within the MCS's stratiform region. The band is the potential-vorticity version of an onion sounding, if you will. At the base of the subsaturated air low in the stratiform region was a very shallow inversion (fig. 5.4), or, in some cases, an isothermal layer (fig. 5.5). Above and below was conditionally unstable air that isolated the high lapse rates (fig. 5.13), thus equating to a band of high potential vorticity.

Most of the gross features in potential vorticity within the composite MCV are due to the distribution of relative vorticity (fig. 5.12). Most of the fine features are due to the distribution of static stability (fig. 5.13). In particular, relative vorticity seems to be the chief constraint on the horizontal extent of high potential vorticity within the core of the composite MCV, whereas variations in stability play a larger role in modulating the potential vorticity's vertical texture. It is difficult to judge how much of the vertical texture would change if many more soundings were added to the composite.

In figures 5.11–5.13 the composite appears vertical, but this was hardly the case for the actual MCV. There are two reasons for the deceptive appearance. First, height is exaggerated by about a factor of 70 in the figures. Second, the drift of the sondes is not represented in the figures. Advection determines the horizontal velocity of balloon-borne sondes, and, to a first approximation, advection determines the orientation of MCVs, especially late in their lifetimes (Johnson and Bartels 1992). Therefore, a sonde's location relative to an MCV is roughly the same throughout ascent, as long as

the two are reasonably close to one another. Because all the data in figures 5.11–5.13 are plotted relative to the MCV's axis, even a tilted MCV would appear vertical in them.

It is easy to overlook how far some MCVs are tilted because height is exaggerated in the vast majority of cross-sectional depictions of the atmosphere. Yet an MCV's tilt can be extreme. Johnson and Bartels (1992) reported a slope of at least 1:50 in the MCV of 23–24 June 1985, which means the top of the vortex was hundreds of kilometers away from the bottom. Unfortunately, I am not confident enough in the resolution of the data to state just how much the MCV of 1 August 1996 may have been tilted. As explained in section 2.11, I located the MCV based on its middle-tropospheric circulation evident in loops of composite reflectivity. Above and below the altitudes of maximum reflectivity, vorticity maxima may have been many tens of kilometers away from the MCV's middle-tropospheric center.

Chapter 6

SYNTHESIS

When the mesoscale convective system (MCS) and the mesoscale convective vortex (MCV) of 1 August 1996 traversed Kansas and Oklahoma, the system and vortex crossed instrument arrays that observed them in more detail than is usually possible except during extensive field projects. The National Oceanic and Atmospheric Administration (NOAA) Wind Profiler Network (NPN) was particularly valuable. By applying to the unusually rich dataset a few variations on simple, proven analysis techniques, I was able to study the MCS and MCV over nine hours on scales between those of semi-daily operational rawinsondes and Doppler radars. The three most important techniques were 1) the use of a spatial bandpass filter to divide observed wind into a component that was predominately the synoptic background wind and a component that was predominately the mesoscale perturbation to that background wind; 2) the retrieval of a temperature profile in gradient balance with the wind of an axisymmetric approximation to the actual MCV; and 3) the construction of a composite MCV from six hours of thermodynamical soundings in and near the vortex.

The MCS of 1 August 1996 comprised a leading convective line and trailing stratiform region. At various stages, the system exhibited many of the features in radar reflectivity common to systems that generate MCVs: early symmetry followed by asymmetry during maturity and decay; enhanced reflectivity in the stratiform region, which twice became notched due to one or more rear inflow jets; and spiral bands of weakly raining clouds as the MCS dissipated.

The environment of the MCS was typical of environments of MCSs in other studies. A synoptic ridge lay to the west of the system, and a trough lay to the east. Vorticity advection was weak. Wind was weakly to moderately sheared and veered from southeasterly near the ground

to west-northwesterly in the middle and upper troposphere. Although a low-level jet was present, gradients were small so advections were weak. Mesoscale and synoptic fronts existed in the areas in which the MCS formed and moved.

The straightforward, but powerful, bandpass filtering made it possible to study the MCS of 1 August 1996 in an environment-relative framework. This framework is familiar to modelers (e.g., Pandya and Durran 1996; Pandya et al. 2000; Nachamkin and Cotton 2000), but empiricists almost never adopt it. The mesoscale (environment-relative) wind was distributed asymmetrically about the MCS, and in the middle troposphere extended farther behind the MCS than ahead of it, which is consistent with analytic studies and numerical simulations of gravity waves generated by heat sources in leading convective lines and trailing stratiform regions (Pandya and Durran 1996; Nachamkin and Cotton 2000). Within the asymmetrically distributed mesoscale wind were the four primary circulations commonly observed in MCSs: a rear-to-front (RTF) mesoscale downdraft and a front-to-rear (FTR) mesoscale updraft that horizontally converged in the middle troposphere, as well as divergent outflows in the lower and upper troposphere.

The mesoscale drafts, together with the convective drafts in the MCS's leading line, vertically mixed the troposphere, thereby partially homogenizing equivalent potential temperature and removing deep layers of potential instability that existed in the environment ahead of the MCS. The mesoscale updraft was approximately saturated with a moist adiabatic lapse rate. The terminus of the mesoscale downdraft was highly subsaturated because advection of drier, potentially warmer air aloft exceeded humidifying and cooling from rain. Profiles of temperature and dewpoint through the downdraft exhibit onion and double-onion patterns. Unlike in some other studies (e.g., Johnson et al. 1989), the downdraft did not foster a pronounced, localized hydrostatic low beneath itself, most likely because observed warming in the lowest part of the subsaturated layer within the downdraft was offset by observed cooling immediately above.

The MCV appeared as a nearly closed circulation within the middle-tropospheric mesoscale wind. At lower and higher altitudes, the resolved circulation was generally not quite closed, but I believe this was at least partly due to the resolution of the data. By the end of the period of detailed

analysis, which was nine hours, the top of the MCV had reached to within a few kilometers of the tropopause, and the bottom had descended to below the lowest data available from the NPN. Data from the Oklahoma Mesonet suggests a vortical circulation may even have reached the ground while the MCS was decaying.

If the composite MCV I constructed accurately represents the actual MCV, within its core was a region of large potential vorticity in the middle troposphere, almost certainly a result of observed diabatic cooling below the melting level and diabatic heating above (Raymond and Jiang 1990; Hertenstein and Schubert 1991; Fritsch et al. 1994). Most of the gross features in potential vorticity within the composite MCV are due to the distribution of relative vorticity. Most of the fine features are due to the distribution of static stability. In particular, relative vorticity seems to be the chief constraint on the horizontal extent of high potential vorticity within the core of the composite MCV, whereas variations in stability modulate the potential vorticity's vertical texture.

The scale-discriminating vorticity budget revealed that both the synoptic background wind and the mesoscale perturbation in wind contributed significant vorticity to the MCV of 1 August 1996. The two largest net, resolved sources of vorticity were convergence and tilting. Although convergence produced the single biggest increase in the MCV's vorticity as it matured, tilting was never negligibly small during the period of detailed analysis. Most of the tendency due to convergence was as mesoscale wind converged both synoptic and mesoscale vorticity. Tilted vorticity was from the horizontal variation of updrafts in the mesoscale wind acting on the horizontal vorticity in both the synoptic wind and the mesoscale wind. Three-dimensional advection was not small, but it did not produce a large net increase in vorticity. Vorticity tendency from horizontal advection was due almost entirely to advection of mesoscale vorticity by the synoptic wind. Tendency from vertical advection was due almost entirely to advection of mesoscale vorticity by the mesoscale wind. Throughout the period of detailed analysis, unresolved sources and sinks of vorticity were just as large as those that were resolved. This comes as little surprise because the bandpass filter excluded more than 90% of the signal of phenomena with wavelengths shorter than 85 km, yet phenomena of this size are prominent sources of positive and negative vorticity (e.g., Weisman and Davis 1998),

often over large regions (e.g., Esbensen et al. 1982; Tollerud and Esbensen 1983).

If tilting is as prominent in most MCVs as it was in the MCV of 1 August 1996, then the character of vertical shear (or, simply, *shear*) in an MCS may be even more important in determining the formation and growth of MCVs than previously thought. Simplified numerical simulations of MCSs often omit environmental shear in the upper half of the troposphere, yet simulated MCVs still form (e.g. Davis and Weisman 1994; Skamarock et al. 1994; Weisman and Davis 1998). This suggests that lower-tropospheric shear's contribution to tilting may be more important to the formation of MCVs than shear at higher altitudes. The MCV of 1 August 1996 was consistent with this suggestion; tilting of horizontal vorticity in sheared wind of the MCS (not the environment) was the lone source of positive vorticity early in the vortex's life. Late in its life, however, as the vortex deepened, shear in both the mesoscale and synoptic wind above 6 km AMSL played a much bigger role through tilting. It may be in the more mature stages of MCVs that simulations without environmental shear in the upper half of the troposphere are missing vital elements of realism.

MCVs that are initially generated by tilting are a growing theme among numerical simulations (e.g., Zhang and Fritsch 1988; Zhang 1992; Weisman and Davis 1998; Cram et al. 2002). In many of these simulations, the tendency from convergence eventually supersedes that from tilting as the MCV matures. In at least one simulation (Zhang and Fritsch 1988), maximum vorticity initially remained at a nearly fixed altitude for a few hours, abruptly ascended as the MCV matured, then remained at a nearly fixed, but higher, altitude after that. This is precisely how the MCV of 1 August 1996 behaved, according to the averaged data. Without far more case studies we cannot know how universal this pattern might be, but that it might be common is intriguing. Perhaps an abrupt change in the maximum vorticity of an MCV signals an abrupt change in its main net source of vorticity—from tilting to convergence, for instance.

If tilting is responsible for generating certain vortices, then some amount of shear, whether mesoscale or synoptic, must favor MCVs. Yet there apparently is such a thing as too much shear, because strong differential horizontal advection seems to shorten the lives of MCVs (e.g., Davis and Weisman 1994; Trier et al. 2000b). Mesoscale and synoptic shear in the lower and middle

troposphere within the MCS of 1 August 1996 were greatest when the MCV first appeared, then decreased after that. The decrease in mesoscale and synoptic shear is evidence that as the MCS matured it altered wind in a way that made the MCV's environment less hostile.

The questions posed at the beginning of the dissertation, and other questions related to them, will not be conclusively and universally answered with operational data sets. As fortuitously rich as the data for this case was, I still had to make compromises and simplifications that veiled the detailed kinematics and thermodynamics involved. An intensive field project designed expressly to study MCVs and the MCSs that generate them is necessary to more thoroughly answer some of the questions raised in this dissertation. Fortunately, it appears that at least one such field project is in the offing. Leading mesoscale scientists are now planning the Bow Echo and MCV Experiment (BAMEX), scheduled for 2003 in the central Plains.

APPENDIX

The following are examples of the formulae used to calculate on a discrete grid the vorticity budget based on (2.1):

$$\xi_{yz} = \frac{w_{y+\Delta y} - w_{y-\Delta y}}{2\Delta y} - \frac{v_{z+\Delta z} - v_{z-\Delta z}}{2\Delta z},$$

$$\eta_{xz} = \frac{u_{z+\Delta z} - u_{z-\Delta z}}{2\Delta z} - \frac{w_{x+\Delta x} - w_{x-\Delta x}}{2\Delta x},$$

$$\zeta_{xy} = \frac{v_{x+\Delta x} - v_{x-\Delta x}}{2\Delta x} - \frac{u_{y+\Delta y} - u_{y-\Delta y}}{2\Delta y},$$

$$\begin{aligned}\Big(\boldsymbol{v}\cdot\boldsymbol{\nabla}\left(\zeta+f\right)\Big)_{x,y} &= u_x\left(\frac{\zeta_{x+\Delta x} - \zeta_{x-\Delta x}}{2\Delta x}\right) \\ &\quad + v_y\left(\frac{\zeta_{y+\Delta y} - \zeta_{y-\Delta y}}{2\Delta y}\right) + v_y\left(\frac{f_{y+\Delta y} - f_{y-\Delta y}}{2\Delta y}\right),\end{aligned}$$

$$\left(w\frac{\partial\zeta}{\partial z}\right)_z = w_z\left(\frac{\zeta_{z+\Delta z} - \zeta_{z-\Delta z}}{2\Delta z}\right),$$

$$\Big((\zeta+f)\boldsymbol{\nabla}\cdot\boldsymbol{v}\Big)_{x,y} = (\zeta+f)_{x,y}\left(\frac{u_{x+\Delta x} - u_{x-\Delta x}}{2\Delta x} + \frac{v_{y+\Delta y} - v_{y-\Delta y}}{2\Delta y}\right),$$

$$\left(\xi\frac{\partial w}{\partial x}\right)_x = \xi_x\left(\frac{w_{x+\Delta x} - w_{x-\Delta x}}{2\Delta x}\right),$$

$$\left(\eta\frac{\partial w}{\partial y}\right)_y = \eta_y\left(\frac{w_{y+\Delta y} - w_{y-\Delta y}}{2\Delta y}\right), \text{ and}$$

$$\begin{aligned}(Z)_t &= \left(\frac{\zeta_t - \zeta_{t-\Delta t}}{\Delta t}\right) + \Big(\boldsymbol{v}\cdot\boldsymbol{\nabla}\left(\zeta+f\right)\Big)_t + \left(w\frac{\partial\zeta}{\partial z}\right)_t \\ &\quad + \Big((\zeta+f)\boldsymbol{\nabla}\cdot\boldsymbol{v}\Big)_t - \left(\xi\frac{\partial w}{\partial x} + \eta\frac{\partial w}{\partial y}\right)_t.\end{aligned}$$

Variables x, y, z, and t respectively are Cartesian coordinates and time. Subscripts are indices of positions and times for which calculations are depicted. An absent subscript is an implied reference index: x, y, z, or t. For example, $u_{x+\Delta x}$ and $u_{x+\Delta x,y,z,t}$ are equivalent. Observations from the NOAA Wind Profiler Network for time t are data averaged over the hour ending at t.

BIBLIOGRAPHY

Barnes, S. L., 1973: Mesoscale objective analysis using weighted time-series observations. NOAA Tech. Memo. ERL NSSL-62, 60 pp. [Available from National Severe Storms Laboratory, Norman, OK 73069.]

Bartels, D. L., J. M. Brown, and E. L. Tollerud, 1997: Structure of a midtropospheric vortex induced by a mesoscale convective system. *Mon. Wea. Rev.*, **125**, 193–211.

Bartels, D. L., and R. A. Maddox, 1991: Midlevel cyclonic vortices generated by mesoscale convective systems. *Mon. Wea. Rev.*, **119**, 104–118.

Barth, M. F., R. B. Chadwick, and D. W. van de Kamp, 1994: Data processing algorithms used by NOAA's wind profiler demonstration network. *Ann. Geophys.*, **12**, 518–528.

Betts, A. K., 1976: The thermodynamic transformation of the tropical subcloud layer by precipitation downdrafts. *J. Atmos. Sci.*, **33**, 1008–1020.

Biggerstaff, M. I., and R. A. Houze, Jr., 1991: Kinematic and precipitation structure of the 10–11 June 1985 squall line. *Mon. Wea. Rev.*, **119**, 3034–3065.

Biggerstaff, M. I., and R. A. Houze, Jr., 1993: Kinematics and microphysics of the transition zone of a midlatitude squall-line system. *J. Atmos. Sci.*, **50**, 3091–3110.

Bosart, L. F., and F. Sanders, 1981: The Johnstown flood of July 1977: a long-lived convective storm. *J. Atmos. Sci.*, **38**, 1616–1642.

Bousquet, O., and M. Chong, 2000: The oceanic mesoscale convective system and associated mesovortex observed 12 December 1992 during TOGA-COARE. *Quart. J. Roy. Meteor. Soc.*, **126**, 189–211.

Brandes, E. A., 1990: Evolution and structure of the 6–7 May 1985 mesoscale convective system and associated vortex. *Mon. Wea. Rev.*, **118**, 109–127. See Corrigendum, **118,** p. 990.

Brandes, E. A., and C. L. Ziegler, 1993: Mesoscale downdraft influences on vertical vorticity in a mature mesoscale convective system. *Mon. Wea. Rev.*, **121**, 1337–1353.

Brock, F. V., K. C. Crawford, R. L. Elliott, G. W. Cuperus, S. J. Stadler, H. L. Johnson, and M. D. Eilts, 1995: The Oklahoma Mesonet: A technical overview. *J. Atmos. Oceanic Technol.*, **12**, 5–19.

Brown, J. M., 1979: Mesoscale unsaturated downdrafts driven by rainfall evaporation: a numerical study. *J. Atmos. Sci.*, **36**, 313–338.

Ceselski, B. F., and L. L. Sapp, 1975: Objective wind field analysis using line integrals. *Mon. Wea. Rev.*, **103**, 89–100.

Chen, S. S., and W. M. Frank, 1993: A numerical study of the genesis of extratropical convective mesovortices. Part I: Evolution and dynamics. *J. Atmos. Sci.*, **50**, 2401–2426.

Chong, M., and O. Bousquet, 1999: A mesovortex within a near-equatorial mesoscale convective system during TOGA COARE. *Mon. Wea. Rev.*, **127**, 1145–1156.

Cotton, W. R., M. S. Lin, R. L. McAnelly, and C. J. Tremback, 1989: A composite model of mesoscale convective complexes. *Mon. Wea. Rev.*, **117**, 765–783.

Cram, T. A., M. T. Montgomery, and R. F. A. Hertenstein, 2002: Early evolution of vertical vorticity in a numerically simulated idealized convective line. *J. Atmos. Sci.*, **59**, 2113–2127.

Cressman, G. P., 1959: An operational objective analysis system. *Mon. Wea. Rev.*, **87**, 367–374.

Davis, C. A., E. D. Grell, and M. A. Shapiro, 1996: The balanced dynamical nature of a rapidly intensifying oceanic cyclone. *Mon. Wea. Rev.*, **124**, 3–26.

Davis, C. A., and M. L. Weisman, 1994: Balanced dynamics of mesoscale vortices produced in simulated convective systems. *J. Atmos. Sci.*, **51**, 2005–2030.

Durran, D. R., and J. B. Klemp, 1982: On the effects of moisture on the Brunt–Väisälä frequency. *J. Atmos. Sci.*, **39**, 2152–2158.

Esbensen, S. K., 1993: Cumulus effects on vorticity. *The Representation of Cumulus Convection in Numerical Models, Meteor. Monogr.*, No. 46, Amer. Meteor. Soc., 93–98.

Esbensen, S. K., E. I. Tollerud, and J.-H. Chu, 1982: Cloud-cluster-scale circulations and the vorticity budget of synoptic-scale waves over the eastern Atlantic intertropical convergence zone. *Mon. Wea. Rev.*, **110**, 1677–1692.

Fortune, M. A., W. R. Cotton, and R. L. McAnelly, 1992: Frontal-wave-like evolution in some mesoscale convective complexes. *Mon. Wea. Rev.*, **120**, 1279–1300.

Fovell, R. G., and Y. Ogura, 1988: Numerical simulation of a midlatitude squall line in two dimensions. *J. Atmos. Sci.*, **45**, 3846–3879.

Frank, W. M., 1983: The cumulus parameterization problem. *Mon. Wea. Rev.*, **111**, 1859–1871.

Fritsch, J. M., J. D. Murphy, and J. S. Kain, 1994: Warm-core vortex amplification over land. *J. Atmos. Sci.*, **51**, 1780–1807.

Gallus, W. A., Jr., and R. H. Johnson, 1991: Heat and moisture budgets of an intense midlatitude squall line. *J. Atmos. Sci.*, **48**, 122–146.

Gallus, W. A., Jr., and R. H. Johnson, 1992: The momentum budget of an intense midlatitude squall line. *J. Atmos. Sci.*, **49**, 422–450.

Gamache, J. F., and R. A. Houze, Jr., 1985: Further analysis of the composite wind and thermodynamic structure of the 12 September GATE squall line. *Mon. Wea. Rev.*, **113**, 1241–1259.

Hack, J. J., and W. H. Schubert, 1986: Nonlinear response of atmospheric vortices to heating by organized cumulus convection. *J. Atmos. Sci.*, **43**, 1559–1573.

Haertel, P. T., and R. H. Johnson, 1998: Two-day disturbances in the equatorial western Pacific. *Quart. J. Roy. Meteor. Soc.*, **124**, 615–636.

Harr, P. A., M. S. Kalafsky, and R. L. Elsberry, 1996: Environmental conditions prior to formation of a midget tropical cyclone during TCM-93. *Mon. Wea. Rev.*, **124**, 1693–1710.

Haynes, P. H., and M. E. McIntyre, 1987: On the evolution of vorticity and potential vorticity in the presence of diabatic heating and frictional or other forces. *J. Atmos. Sci.*, **44**, 828–841.

Hertenstein, R. F. A., and W. H. Schubert, 1991: Potential vorticity anomalies associated with squall lines. *Mon. Wea. Rev.*, **119**, 1663–1672.

Hilgendorf, E. R., and R. H. Johnson, 1998: A study of the evolution of mesoscale convective systems using WSR-88D data. *Wea. Forecasting*, **13**, 437–452.

Hoskins, B. J., M. E. McIntyre, and A. W. Robertson, 1985: On the use and significance of isentropic potential vorticity maps. *Quart. J. Roy. Meteor. Soc.*, **111**, 877–946.

Houze, R. A., Jr., 1982: Cloud cluster and large-scale vertical motions in the tropics. *J. Meteor. Soc. Japan*, **60**, 396–409.

Houze, R. A., Jr., 1989: Observed structure of mesoscale convective systems and implications for large-scale heating. *Quart. J. Roy. Meteor. Soc.*, **115**, 425–461.

Houze, R. A., Jr., 1993: *Cloud Dynamics*. Academic Press, 573 pp.

Houze, R. A., Jr., S. A. Rutledge, M. I. Biggerstaff, and B. F. Smull, 1989: Interpretation of Doppler weather radar displays of midlatitude mesoscale convective systems. *Bull. Amer. Meteor. Soc.*, **70**, 608–619.

Houze, R. A., Jr., B. F. Smull, and P. Dodge, 1990: Mesoscale organization of springtime rainstorms in Oklahoma. *Mon. Wea. Rev.*, **118**, 613–654.

Johnson, R. H., and D. L. Bartels, 1992: Circulations associated with a mature-to-decaying midlatitude mesoscale convective system. Part II: Upper-level features. *Mon. Wea. Rev.*, **120**, 1301–1320.

Johnson, R. H., S. Chen, and J. J. Toth, 1989: Circulations associated with a mature-to-decaying midlatitude mesoscale convective system. Part I: Surface features—heat bursts and mesolow development. *Mon. Wea. Rev.*, **117**, 942–959.

Johnson, R. H., P. C. Ciesielski, and K. A. Hart, 1996: Tropical inversions near the 0°C level. *J. Atmos. Sci.*, **53**, 1838–1855.

Johnson, R. H., and W. A. Gallus, Jr., 1988: The wake structure of an intense midlatitude squall line in OK PRE-STORM. Preprints, *Eighth Conf. on Numerical Weather Prediction and 15th Conf. on Severe Local Storms*, Baltimore, MD, Amer. Meteor. Soc., 229–232.

Johnson, R. H., W. A. Gallus, Jr., and M. D. Vescio, 1990: Near-tropopause vertical motion within the trailing stratiform region of a midlatitude squall line. *J. Atmos. Sci.*, **47**, 2200–2210.

Johnson, R. H., and P. J. Hamilton, 1988: The relationship of surface pressure features to the precipitation and airflow structure of an intense midlatitude squall line. *Mon. Wea. Rev.*, **116**, 1444–1472.

Johnson, R. H., and G. S. Young, 1983: Heat and moisture budgets of tropical mesoscale anvil clouds. *J. Atmos. Sci.*, **40**, 2138–2147.

Jones, S. C., 1995: The evolution of vortices in vertical shear. I: Initially barotropic vortices. *Quart. J. Roy. Meteor. Soc.*, **121**, 821–851.

Keenan, T. D., and S. A. Rutledge, 1993: Mesoscale characteristics of monsoonal convection and associated stratiform precipitation. *Mon. Wea. Rev.*, **121**, 352–374.

Koch, S. E., M. DesJardins, and P. J. Kocin, 1983: An interactive Barnes objective map analysis scheme for use with satellite and conventional data. *J. Climate Appl. Meteor.*, **22**, 1487–1503.

Leary, C. A., 1980: Temperature and humidity profiles in mesoscale unsaturated downdrafts. *J. Atmos. Sci.*, **37**, 1005–1012.

LeMone, M. A., 1983: Momentum transport by a line of cumulonimbus. *J. Atmos. Sci.*, **40**, 1815–1834.

Loehrer, S. M., and R. H. Johnson, 1995: Surface pressure and precipitation life cycle characteristics of PRE-STORM mesoscale convective systems. *Mon. Wea. Rev.*, **123**, 600–621.

Maddox, R. A., 1980: An objective technique for separating macroscale and mesoscale features in meteorological data. *Mon. Wea. Rev.*, **108**, 1108–1121.

Maddox, R. A., D. J. Perkey, and J. M. Fritsch, 1981: Evolution of upper tropospheric features during the development of a mesoscale convective complex. *J. Atmos. Sci.*, **38**, 1664–1674.

Mapes, B. E., 1993: Gregarious tropical convection. *J. Atmos. Sci.*, **50**, 2026–2037.

Mapes, B. E., and R. A. Houze, Jr., 1995: Diabatic divergence profiles in western Pacific mesoscale convective systems. *J. Atmos. Sci.*, **52**, 1807–1828.

Mapes, B. E., and P. Zuidema, 1996: Radiative-dynamical consequences of dry tongues in the tropical troposphere. *J. Atmos. Sci.*, **53**, 620–638.

Menard, R. D., and J. M. Fritsch, 1989: A mesoscale convective complex-generated inertially stable warm core vortex. *Mon. Wea. Rev.*, **117**, 1237–1261.

Miller, D., and J. M. Fritsch, 1991: Mesoscale convective complexes in the western Pacific region. *Mon. Wea. Rev.*, **119**, 2978–2992.

Montgomery, M. T., and J. Enagonio, 1998: Tropical cyclogenesis via convectively forced vortex Rossby waves in a three-dimensional quasigeostrophic model. *J. Atmos. Sci.*, **55**, 3176–3207.

Nachamkin, J. E., and W. R. Cotton, 2000: Interactions between a developing mesoscale convective system and its environment. Part II: Numerical simulation. *Mon. Wea. Rev.*, **128**, 1225–1244.

Nicholls, M. E., R. A. Pielke, and W. R. Cotton, 1991: Thermally forced gravity waves in an atmosphere at rest. *J. Atmos. Sci.*, **48**, 1869–1884.

O'Brien, J. J., 1970: Alternative solutions to the classical vertical velocity problem. *J. Appl. Meteor.*, **9**, 197–203.

Olsson, P. Q., and W. R. Cotton, 1997: Balanced and unbalanced circulations in a primitive equation simulation of a midlatitude MCC. Part II: Analysis of balance. *J. Atmos. Sci.*, **54**, 479–497.

Orlanski, I., 1975: A rational subdivision of scales for atmospheric processes. *Bull. Amer. Meteor. Soc.*, **56**, 527–530.

Pandya, R. E., and D. R. Durran, 1996: The influence of convectively generated thermal forcing on the mesoscale circulation around squall lines. *J. Atmos. Sci.*, **53**, 2924–2951.

Pandya, R. E., D. R. Durran, and M. L. Weisman, 2000: The influence of convective thermal forcing on the three-dimensional circulation around squall lines. *J. Atmos. Sci.*, **57**, 29–45.

Parker, M. D., and R. H. Johnson, 2000: Organizational modes of midlatitude mesoscale convective systems. *Mon. Wea. Rev.*, **128**, 3413–3436.

Raymond, D. J., and H. Jiang, 1990: A theory for long-lived mesoscale convective systems. *J. Atmos. Sci.*, **47**, 3067–3077.

Redelsperger, J.-L., and J.-P. Lafore, 1988: A three-dimensional simulation of a tropical squall line: Convective organization and thermodynamic vertical transport. *J. Atmos. Sci.*, **45**, 1334–1356.

Reed, R. J., and R. H. Johnson, 1974: A vorticity budget of synoptic wave disturbances in the tropical western Pacific. *J. Atmos. Sci.*, **31**, 1784–1790.

Rogers, R. F., and J. M. Fritsch, 2001: Surface cyclogenesis from convectively driven amplification of midlevel mesoscale convective vortices. *Mon. Wea. Rev.*, **129**, 605–637.

Rosenthal, S. L., 1980: Numerical simulation of tropical cyclone development with latent heat release by the resolvable scales, II. Propagating small-scale features observed in the prehurricane phase. NOAA Tech. Rep. ERL 413-AOML 29, 43 pp. [NTIS PE81-176588.]

Rutledge, S. A., R. A. Houze, Jr., M. I. Biggerstaff, and T. Matejka, 1988: The Oklahoma-Kansas mesoscale convective system of 10–11 June 1985: Precipitation structure and single-Doppler radar analysis. *Mon. Wea. Rev.*, **116**, 1409–1430.

Schaefer, J. T., and C. A. Doswell III, 1979: On the interpolation of a vector field. *Mon. Wea. Rev.*, **107**, 458–476.

Schubert, W. H., and J. J. Hack, 1982: Inertial stability and tropical cyclone development. *J. Atmos. Sci.*, **39**, 1687–1697.

Schubert, W. H., J. J. Hack, P. L. Silva Dias, and S. R. Fulton, 1980: Geostrophic adjustment in an axisymmetric vortex. *J. Atmos. Sci.*, **37**, 1464–1484.

Scott, J. D., and S. A. Rutledge, 1995: Doppler radar observations of an asymmetric MCS and associated vortex couplet. *Mon. Wea. Rev.*, **123**, 3437–3457.

Shafer, M. A., C. A. Fiebrich, D. S. Arndt, S. E. Fredrickson, and T. W. Hughes, 2000: Quality assurance procedures in the Oklahoma Mesonetwork. *J. Atmos. Oceanic Technol.*, **17**, 474–494.

Shapiro, L. J., and H. E. Willoughby, 1982: The response of balanced hurricanes to local sources of heat and momentum. *J. Atmos. Sci.*, **39**, 378–394.

Sherwood, S. C., 2000: On moist instability. *Mon. Wea. Rev.*, **128**, 4139–4142.

Skamarock, W. C., M. L. Weisman, and J. B. Klemp, 1994: Three-dimensional evolution of simulated long-lived squall lines. *J. Atmos. Sci.*, **51**, 2563–2584.

Smull, B. F., and R. A. Houze, Jr., 1985: A midlatitude squall line with a trailing region of stratiform rain: Radar and satellite observations. *Mon. Wea. Rev.*, **113**, 117–133.

Smull, B. F., and R. A. Houze, Jr., 1987: Rear inflow in squall lines with trailing stratiform precipitation. *Mon. Wea. Rev.*, **115**, 2869–2889.

Stumpf, G. J., R. H. Johnson, and B. F. Smull, 1991: The wake low in a midlatitude mesoscale convective system having complex convective organization. *Mon. Wea. Rev.*, **119**, 134–158.

Sui, C.-H., and M. Yanai, 1986: Cumulus ensemble effects on the large-scale vorticity and momentum fields of GATE. Part I: Observational evidence. *J. Atmos. Sci.*, **43**, 1618–1642. See Corrigendum, **46,** p. 1630.

Tollerud, E. I., and S. K. Esbensen, 1983: An observational study of the upper-tropospheric vorticity fields in GATE cloud clusters. *Mon. Wea. Rev.*, **111**, 2161–2175.

Trier, S. B., and C. A. Davis, 2002: Influence of balanced motions on heavy precipitation within a long-lived convectively generated vortex. *Mon. Wea. Rev.*, **130**, 877–899.

Trier, S. B., C. A. Davis, and W. C. Skamarock, 2000a: Long-lived mesoconvective vortices and their environment. Part II: Induced thermodynamic destabilization in idealized simulations. *Mon. Wea. Rev.*, **128**, 3396–3412.

Trier, S. B., C. A. Davis, and J. D. Tuttle, 2000b: Long-lived mesoconvective vortices and their environment. Part I: Observations from the central United States during the 1998 warm season. *Mon. Wea. Rev.*, **128**, 3376–3395.

Weber, B. L., D. B. Wuertz, D. C. Welsh, and R. McPeek, 1993: Quality controls for profiler measurements of winds and RASS temperatures. *J. Atmos. Oceanic Technol.*, **10**, 452–464.

Webster, P. J., and G. L. Stephens, 1980: Tropical upper-tropospheric extended clouds: Inferences from winter MONEX. *J. Atmos. Sci.*, **37**, 1521–1541.

Weisman, M. L., and C. A. Davis, 1998: Mechanisms for the generation of mesoscale vortices within quasi-linear convective systems. *J. Atmos. Sci.*, **55**, 2603–2622.

Whiteman, C. D., X. Bian, and S. Zhong, 1997: Low-level jet climatology from enhanced rawinsonde observations at a site in the southern Great Plains. *J. Appl. Meteor.*, **36**, 1363–1376.

Williams, D. T., 1963: The thunderstorm wake of May 4, 1961. National Severe Storms Project Rep. 18, U.S. Dept. of Commerce, Washington, D.C., 23 pp. [NTIS PB-168223.]

Wong, T., G. L. Stephens, and P. W. Stackhouse, Jr., 1993: The radiative budgets of a tropical mesoscale convective system during the EMEX-STEP-AMEX experiment, 2. Model results. *J. Geophys. Res.*, **98**, 8695–8711.

Yang, M.-J., and R. A. Houze, Jr., 1995: Sensitivity of squall line rear inflow to ice microphysics and environmental humidity. *Mon. Wea. Rev.*, **123**, 3175–3192.

Zhang, D.-L., 1992: The formation of a cooling-induced mesovortex in the trailing stratiform region of a midlatitude squall line. *Mon. Wea. Rev.*, **120**, 2763–2785.

Zhang, D.-L., and J. M. Fritsch, 1988: A numerical investigation of a convectively generated, inertially stable, extratropical warm-core mesovortex over land. Part I: Structure and evolution. *Mon. Wea. Rev.*, **116**, 2660–2687.

Zipser, E. J., 1969: The role of organized unsaturated convective downdrafts in the structure and rapid decay of an equatorial disturbance. *J. Appl. Meteor.*, **8**, 799–814.

Zipser, E. J., 1977: Mesoscale and convective-scale downdrafts as distinct components of squall-line structure. *Mon. Wea. Rev.*, **105**, 1568–1589.